Diss. ETH No. 25995

Computation with Artificial Spin Ice: Nanomagnetic Logic and Monopole Circuits

A thesis submitted to attain the degree of
DOCTOR OF SCIENCES of ETH ZURICH
(Dr. sc. ETH Zurich)

presented by
Hanu Arava

M.Sc., Texas State University

born 02.09.1987
citizen of India

Accepted on the recommendation of

Prof. Dr. Laura J. Heyderman
Prof. Dr. Pietro Gambardella
Prof. Dr. Christopher H. Marrows

2019

ABSTRACT

In this PhD thesis, a new perspective to computation using nanomagnets is provided. The thesis makes use of dipolar coupled single domain nanomagnets, which are arranged on a lattice such as a square (or kagome lattice), producing an artificial square ice. For such an arrangement of nanomagnets, there are a large number of magnetic moment configurations that are associated with different dipolar energies and could eventually be exploited to mimic synaptic connectivity in the human brain. In this thesis, it is systematically shown that artificial spin ice inspired structures could be implemented in the transport of data, and to perform deterministic and probabilistic computational logic. In addition, a new scheme to control the location of nucleation of monopoles and the direction of the generated monopole currents is presented. Such a deterministic control of monopole currents could be implemented in monopole based computation.

In the first instance, chains of square rings are used to transport data from one location to another. Transportation of data was demonstrated by setting the initial state of the nanomagnets with an applied magnetic field and then allowing the relaxation of the magnetic moments to a ground state by increasing the temperature. It was shown that the ground state ordering in a linear chain of square rings could be controlled with an input nanomagnet, which was sufficiently long to ensure that it did not change its moment orientation when the temperature was raised. The data could be transported between the input and output magnet over a distance that was an order of magnitude larger than the distance previously achieved with a linear chain of nanomagnets.

Subsequently, a NAND logic gate was designed with an arrangement of up to 12 nanomagnets to reliably perform Boolean logic operations. A logic operation involved the relaxation of the nanomagnets from a particular initial state to a final ground state involving a sequence of moment reorientations. The energy path from the initial state to the final state, or the relaxation pathway, was engineered to reliably give one specific final output moment. It was demonstrated that this is reliable for all the four logic operations required to produce a NAND logic gate. The experimentally observed operational reliability of over 90% of the logic gates surpassed the ~50% operational reliability found in traditional nanomagnetic logic.

With the goal of creating a device that would mimic the human brain, a probabilistic logic gate was experimentally demonstrated, in which higher energy metastable states were incorporated into a relaxation pathway to produce a probabilistic output. A set of rules were derived to help identify arrangements of nanomagnets that would give moment reorientations to a higher energy state within a given relaxation pathway. Importantly, it was shown that the probability of an output could be tuned to any value by changing the strength of dipolar coupling between different magnets. Such a tuneable probability is essential for the development of artificial neural networks, in which the probability of

obtaining a certain output needs to be modified based on feedback. As a last step, a scheme to connect several logic gates was developed to demonstrate their use in extended circuits.

The final challenge addressed in this thesis was the control of the location of nucleation (or injection) of emergent magnetic monopoles and the generation of directional monopole currents in an artificial square ice. In order to understand the probability of injecting monopoles at the edges of an artificial square ice, it was important to consider the influence of the single vertex arrangements. The number of magnets at a single vertex can be reduced from four nanomagnets at the vertex to three or two nanomagnets. Assuming a globally applied initial field set state, the dipolar energies associated with these different vertex configurations will be different. In particular, the switching probabilities, from the initial state to a next state, continue to decrease as the number of magnets decreases. It was experimentally shown that deterministic injection of monopole currents is therefore possible when one of the artificial square ice edges was modified to include two nanomagnets at a vertex and the other incorporated four nanomagnets. Smaller structures were also built, in which deterministic injection and termination of monopole currents was demonstrated and a preliminary idea towards building a monopole current based transistor was introduced. Finally, the idea of using different vertex configurations incorporated in artificial spin ice structures is proposed, to give probabilistic generation and termination of monopole currents. Such probabilistic currents could be used for building monopole based probabilistic computing devices.

The ideas developed in this thesis could serve as foundational building blocks towards using artificial spin ice for computational applications. More importantly a new perspective is provided where relaxation pathways are considered for use in computation.

Zusammenfassung

In dieser Dissertation wird eine neue Perspektive auf den Transfer und die Verarbeitung von binären Daten mithilfe von Nanomagneten gegeben. Hierzu werden dipolar gekoppelte eindomänige Nanomagnete verwendet, die auf einem zweidimensionalen Gitter, etwa einem Quadrat-Gitter oder einem Kagome-Gitter, angeordnet sind. Solche sogenannte „künstlichen Spin-Eise“ ergeben eine große Anzahl magnetischer Konfigurationen mit verschiedenen dipolaren Energien, die letztendlich dazu genutzt werden könnten, um die synaptische Verbindung im menschlichen Gehirn nachzuahmen. In dieser Arbeit wird systematisch gezeigt, dass in von künstlichen Spinsystemen inspirierte nanomagnetische Konfigurationen Daten transportieren werden können sowie deterministische und probabilistische Berechnungslogiken ausgeführt werden können. Weiterhin wird ein neues Schema vorgestellt, mit dem sich der Ort der Entstehung und die Propagationsrichtung von sogenannten magnetischen Monopolen in nanomagnetischen Kagome-Gittern steuern lässt. Eine derartige deterministische Kontrolle von Monopolströmen könnte ebenfalls für die Verarbeitung von binären Daten verwendet werden.

In einem ersten Experiment werden Ketten von quadratischen Ringen verwendet, um Daten von einem Ort zu einem anderen zu transportieren. Der Datentransfer wurde experimentell demonstriert, wobei zuerst der Anfangszustand der Nanomagnete mit einem angelegten Magnetfeld initialisiert wurde, und dann die thermische Relaxation der magnetischen Momente in einen Grundzustand durch Erhöhen der Temperatur ermöglicht wurde. Es wurde gezeigt, dass der Grundzustand in einer linearen Kette von quadratischen Ringen durch den Zustand eines Eingabe-Moments kontrolliert werden kann. Dieser Eingabe-Nanomagnet ist ausreichend lang, um sicherzustellen, dass sich seine magnetische Konfiguration während der Transfer-Phase mit erhöhter Temperatur nicht ändert. Die Daten konnten zwischen dem Eingabe- und dem Ausgabemagneten über eine Distanz transportiert werden, die eine Größenordnung größer war als die Distanz, die zuvor mit einer linearen Kette von Nanomagneten erreicht wurde.

Anschließend wurde ein NAND-Logikgatter mit einer Anordnung von bis zu zwölf Nanomagneten entworfen, um zuverlässig Boolesche Logikoperationen auszuführen zu können. Eine logische Operation beinhaltete die Relaxation der Nanomagnete von einem bestimmten Anfangszustand in einen finalen Grundzustand, durch eine Sequenz von Umorientierung einzeler Nanomagnete. Unter Betrachtung der Energielandschaft der wechselwirkenden Nanomagnete wurde solch ein Relaxationspfad so ausgelegt, dass ein bestimmtes Ausgabemoment zuverlässig erreicht wird. Es wurde gezeigt, dass dies für alle vier Logikoperationen, die zur Herstellung eines NAND-Logikgatters erforderlich sind, eintritt. Die experimentell beobachtete Zuverlässigkeit von über 90% der Logikgatter übertraf weit die von 50% in bisher getesteten nanomagnetischen Logikgattern.

Mit dem Ziel, ein Gerät zu schaffen, das die Datenverarbeitung in einem menschliche Gehirn nachahmt, wurde experimentell ein probabilistisches Logikgatter demonstriert, bei dem die Relaxationspfade metastabile Zustände enthalten, welche zu es ermöglichen verschiedene Endzustände mit bestimmter Wahrscheinlichkeit zu erreichen. Eine Reihe von Regeln wurde abgeleitet, um Anordnungen von Nanomagneten zu identifizieren, welche Relaxationspfade, die Zustände höherer Energie enthalten, bedingen, und somit zu verschiedenen Endzuständen führen können. Es wurde insbesondere gezeigt, dass die Wahrscheinlichkeit einer Ausgabe beliebig eingestellt werden kann, indem die Stärke der dipolaren Kopplung zwischen verschiedenen Magneten verändert wird. Eine solche Kontrolle ist für die Entwicklung künstlicher neuronaler Netze wesentlich, in denen die Wahrscheinlichkeit, eine bestimmte Ausgabe zu erhalten, basierend auf einem Rückkopplungs-Kreis modifiziert werden muss. Als letzter Schritt wurde ein Schema zum Verbinden mehrerer Logikgatter entwickelt, um ihre Verwendung in erweiterten Schaltungen zu demonstrieren.

Die letzte Herausforderung, die in dieser Arbeit angesprochen wurde, war die Kontrolle der Lage der Nukleirung (oder Injektion) von emergenten magnetischen Monopolen und die Erzeugung von gerichteten Monopolströmen in einem künstlichen Spin-Eis. Um die Wahrscheinlichkeit einer Injektion von Monopolen an den Rändern eines künstlichen Spin-Eises zu verstehen, war es wichtig, den Einfluss von einzelnen Vertices, d.h. Treffpunkt verschiedener Nanomagnete, zu berücksichtigen. Die Anzahl der Magneten an einem einzelnen Vertex kann von vier Nanomagneten am Vertex auf drei oder zwei Nanomagnete reduziert werden, was die dipolaren Energien dieser Konfigurationen modifiziert. Insbesondere nimmt mit reduzierter Anzahl Nanomagnete am Vertex die Wahrscheinlichkeit ab, dass sich einzelne Momente umorientieren. Es wurde experimentell gezeigt, dass eine deterministische Injektion von Monopolströmen möglich ist, wenn eine der Kanten des künstlichen Spin-Eises so modifiziert wurde, dass sie zwei Nanomagnete an einem Vertex und die andere Kante vier Nanomagnete pro Vertex enthält. In ähnlichen Strukturen wurde die deterministische Injektion und Termination von Monopolströmen demonstriert und eine erste Idee zum Bau eines Monopolstrom-Transistors eingeführt. Schließlich wird die Idee der Verwendung unterschiedlicher Vertexkonfigurationen in künstlichen Spin-Eis-Strukturen vorgeschlagen, um eine probabilistische Erzeugung und Termination von Monopolströmen zu ermöglichen. Solche probabilistischen Ströme könnten zum Aufbau von auf Monopolen basierenden probabilistischen Gatter verwendet werden.

Die in dieser Arbeit entwickelten Ideen zu Relaxationspfaden in künstlichen Spin-Systemen und die Beziehung der zugrundeliegenden geometrischen Anordnung der Nanomagnete zum erwarteten Relaxationsverhalten können als grundlegende Bausteine für die Verwendung von künstlichen Spin-Eis für den Transport und der Verarbeitung von Daten, insbesondere für neuartige Anwendungen von probabilistische Berechnungsmethoden, dienen.

Table of Contents

List of Abbreviations

SLS	Swiss Light Source
PSI	Paul Scherrer institute
SEM	Scanning Electron Microscope
MFM	Magnetic Force Microscope
AFM	Atomic Force Microscope
X-PEEM	X-ray Photoemission Electron Microscope
XMCD	X-ray Magnetic Circular Dichroism
MC	Monte Carlo
KMC	Kinetic Monte Carlo

Outline

A typical computer is essentially an adding machine, in which two unique states, representing 1 and 0, are used to perform Boolean algebra. For example: the transistor in a computer is such an object consisting of two unique states, where each state is characterized by the transistor's turning on or off [1]. As more transistors are used to perform the same task, computers get faster. Computers get "smarter" when better mathematics is implemented to run Boolean algebra[2, 3].

An avenue of interest in providing an alternative to traditional computing has been the introduction of nanomagnets in computation[4, 5]. The advantage to using nanomagnets is the lower power required to operate them. Nanomagnet based circuits that mimic the same functionality as that of traditional CMOS circuits have been successfully demonstrated[6]. However, their implementation into devices for computation has been hindered by their lack of operational reliability[5, 7] and not the least; they are much larger in size than transistors. Therefore, there has been a general realization in the community that nanomagnets would not replace traditional computers, but may be implemented as an add-on to assist in computation.

As part of the artificial spin ice community, I realized that, I may be able to bring a new perspective to computation using nanomagnets. An artificial spin ice consists of arrays of dipolar interacting nanomagnets arranged on a periodic lattice[8]. Such an N-body type interaction between different nanomagnets gives rise to a large number of magnetic states with unique energies. There is a case here to be made that, just as trillions of neurons in the human brain gives rise to decision making[9], it may be possible to implement this N-body interaction in artificial spin ice as a vehicle to mimic portions of decision making. Therefore, I set out to show that artificial spin ice may provide an alternative route to computation, in both Boolean and probabilistic schemes.

This thesis is my effort in implementing the ideas of artificial spin ice, in Boolean and probabilistic schemes for use as a traditional adding machine and that of a neuromorphic device. Collaborations with staff at the Swiss Light Source (PSI), Condensed Matter Theory Group (PSI), and the University of Hamburg were critical to the success of the projects described in the thesis. Individual contributions from colleagues are provided at the end of each chapter. Finally, I am grateful to the support provided by the staff of the Laboratory for Mesoscopic Systems and the Laboratory for Micro- and Nanotechnology at PSI.

The thesis is divided into eight chapters, in which I address concepts, challenges, and new ideas to the implementation of artificial spin in computation. More specifically:

Chapter 1 (Introduction): Here a brief overview of artificial spin ice is given. Along with this, an overview of computation (Boolean and Probabilistic) using nanomagnets is given and finally, I discuss the phenomenon of monopole currents in artificial spin ice and the possibility of using these

monopole currents to achieve computation. Finally, I pose three critical questions that drive my thesis. These critical questions are addressed in three different chapters.

Chapter 2 (Physics of Nanomagnets): An overview of the physics governing the formation of domains in nanomagnets is provided. In addition, the role of heating, which has been the primary method to thermally relax the arrays of nanomagnets discussed in the thesis, in influencing the dynamics of moment reorientations in nanomagnets is addressed.

Chapter 3 (Methods): This chapter details the methods implemented to fabricate the arrays of nanomagnets and the different techniques that were used to probe the structures. In addition, a background is provided on the different types of analytical calculations found throughout the thesis.

Chapter 4 (Optimization in Linear Chains): One of the initial goals, as part of my effort into computation using artificial spin ice, was to optimize the quality of my structures by performing experiments that have long been a staple of the nanomagnetic logic community. This chapter details the results obtained from thermalization and field relaxation in linear chains of nanomagnets. I also provide a motivation for why a traditional approach to computation using nanomagnets may not be ideal.

Chapter 5 (Boolean Computation with Artificial Spin Ice): Here I discuss the construction of logic gates, inspired from artificial spin ice, to perform Boolean algebra. A functionally complete NAND logic gate is presented.

Chapter 6 (Probabilistic Computation with Artificial Spin Ice): Weighted outputs for use in applications such as artificial neural networks are discussed and the physics behind relaxation pathways is introduced. By considering the relaxation pathways, an explanation for the high reliability in Boolean computation using the artificial spin ice inspired logic gates is provided,. Additionally, new logic gate designs are demonstrated for probabilistic computational schemes. Finally, a set of rules/conditions are defined for the design and construction logic gates for use in Boolean and probabilistic schemes.

Chapter 7 (Deterministic Injection of Monopole Currents in Artificial Spin Ice): We develop a scheme to control the location of the nucleation of monopole defects in artificial spin ice. Such a scheme is further implemented in the generation of directional monopole currents. The influence of nanomagnet thickness on the nucleation probability in arrays of artificial spin ice is quantified using a switching probabilities plot. Such an improved control in the nucleation and generation of monopole currents forms the basis for monopole based circuits for use in computation.

Chapter 8 (Conclusion and Outlook): A summary of the most critical results as part of this thesis is provided and their role in advancing the implementation of computation in artificial spin ice systems is discussed.

CHAPTER 1: INTRODUCTION

My goal in this chapter is to provide a motivation behind the work carried out in this thesis. Broadly, the thesis aims to develop computational solutions using nanomagnets (magnets with sub-micron dimensions), drawing inspiration from ideas in the field of artificial spin ice. I will start by briefly introducing the field of artificial spin ice. I will then lay out the motivation behind the thesis by splitting it into three separate questions as part of three sub-chapters, these being (1) Boolean computation using nanomagnets, (2) non-Boolean computation using nanomagnets, and (3) Monopole currents. Each of these three sub-chapters contains a brief overview of the field and broadly describes the open challenges facing scientists today. The sub-chapter concludes by drawing up a specific open question in the field. These three questions form the basis for the thesis.

1.1 Geometrical Frustration in Magnetism

Geometrical frustration in magnetism refers to the arrangement (or geometry) of spins on a lattice where the interactions between different spins are not simultaneously minimized. The origins of frustration were initially described by Linus Pauling in water ice[10], where the bonding distances of hydrogen atoms surrounding each oxygen atom cannot be energetically minimized at the same time (see Figure 1.1). Later, it was shown that naturally occurring rare earth Pyrochlores[11] observed a similar behavior to that of water ice. Unlike water ice, where frustration arose as a consequence of proton placement, Pyrochlores instead comprised of spins arranged on corners of a tetrahedra leading to magnetic frustration.

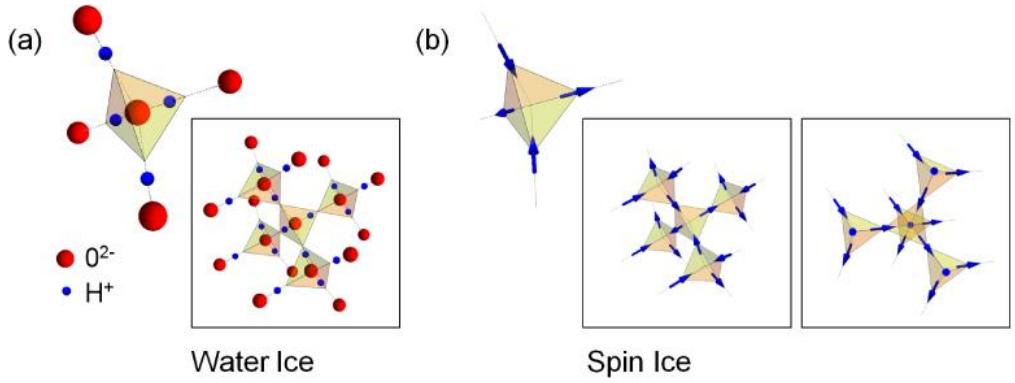

Figure 1.1: (a) Protons (hydrogen) positioned on the corners of a tetrahedra in a water ice molecule. Minimization of energy could occur in two configurations, where two of the protons need to be closer to the oxygen ion and the other two protons need to be farther away. The frustration leads to positional degeneracy in water ice. (b) An example of a rare earth Pyrochlore, where, unlike water ice, protons are replaced by magnetic ions. Such an arrangement of spins leads to spin mediated frustration, and this system is referred to as a spin ice. Figure adapted from Heyderman and Stamps [12]

The advent of an "artificial" spin ice was with the demonstration of frustration in lithographically patterned arrays of Permalloy nanomagnets arranged on a square lattice[8]. Around the same time, it was observed that spin excitations in naturally occurring Pyrochlores behaved like magnetic monopoles with Dirac strings connecting them[13]. Immediately afterwards, an artificial analogue to magnetic monopole in artificial square ice was described[14]. This was followed by the first experimental observation of emergent magnetic monopoles in artificial spin ice involving kagome lattice configurations[15, 16].

The field of artificial spin ice continues to pose fundamental questions and unearth novel phenomena involving a variety of ice models and the dynamics in their evolution. In addition, artificial spin ice provides a fertile play ground to probe the mechanism behind complex physics such as many body physics and phase transitions in materials[12, 17]. On the applications front, we find artificial spin ice put to use in the creation of tunable metamaterials and sensors[18, 19, 20]. More recently, efforts have been made to implement artificial spin ice in the field of computation[21, 22]. This includes the work in this thesis, where the first experimental demonstration of a functionally complete logic gate, using artificial square ice was demonstrated[22].

1.2 Boolean Computation using Nanomagnets

Moore's law predicts that the transistor density will double every two years. Our technology has until now either met with or exceeded the expectations of Moore's Law. However, the decrease in size has not been complemented with a decrease in operating and standby power of transistors[23]. To counter issues with power dissipation, various architectures and novel approaches have been proposed. These include changes to composition of gate oxides and implementing negative capacitance to lower the operating power [24, 25]. However, while most solutions provide reduced power consumption for standby operation, they do not necessarily eliminate it altogether.

Using a non-volatile building block that does not require any standby power and has low operating power would therefore be ideal for computing. Nanomagnets have been proposed as this alternative[5] since they are non-volatile and switch at energy scales that are six orders of magnitude lower than traditional CMOS. Indeed, the latter was experimentally confirmed recently where nanomagnetic switching was measured to be around 5 zJ when compared with femto-joule operation of CMOS[26]. With the possibility to have two stable magnetization directions that can act as binary bits (corresponding to on and off operation of a traditional transistor), nanomagnets hold the potential to play a significant role in next generation computing. Elongated nanomagnets manufactured from Permalloy are ideally suited since the magnetic configuration is determined predominantly by the shape anisotropy with magnetization pointing in one of two directions parallel to the magnet long axis. Earlier designs with linear chains of nanomagnets were implemented in order to propagate "information" along the chains, which is encoded in the magnetization orientation [4, 5, 27].

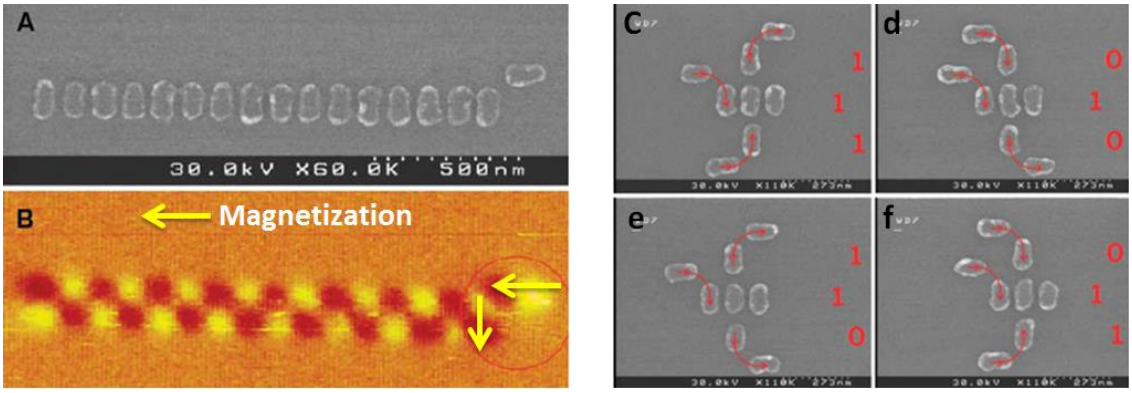

Figure 1.2: (A) SEM image of a linear chain of nanomagnets with a driver (circled in red in B is the driver and the first nanomagnet in the chain) and (B) associated MFM image. To the right are four SEM images (c, d, e & f) of a majority logic gate. Figure adapted from Imre et.al.[5]

Additionally, nanomagnets were implemented in logic gate designs for application in traditional computing. However, two key hurdles in the form of reliability and operational speed have plagued the field since its inception. Shown in Figure 1.2 is one of the first experiments demonstrating the use of nanomagnets for the transfer of information and logic. With an operating efficiency of 25% - 50% [5, 7, 28] - corresponding to the percentage of correct outputs – such logic gates using nanomagnets cannot compete with existing technology. Reliability in propagating information along nanomagnet chains also remains a major hurdle with most studies indicating a 5-10 nanomagnet linear chain length, corresponding to a distance of 1-2 μm, as the upper limit before errors are incurred. More recently, in a comprehensive study, it was found that defects in the magnetic configurations arose in chains as small as 5 nanomagnets[7]. To counter issues with reliability, altering the shape of nanomagnets away from the standard ellipsoids has been proposed. The idea here was to introduce an additional hard axis in the nanomagnets that would serve as an energy barrier, thereby preventing easy reversal of nanomagnets. Most popular has been the biaxial anisotropy nanomagnets created by the addition of notches in each corner of a rectangular nanomagnet[29]. However, these have not made a significant impact in improving nanomagnetic reliability. High speed performance of nanomagnetic chains has recently been demonstrated at the pico-second timescale and this indicated that nanomagnets have the possibility to compete with traditional CMOS in terms of operational speed[30].

The key question here is, is there a viable design alternative to perform nanomagnet based Boolean computation using ideas from artificial spin ice? And following from this, is it possible to demonstrate Boolean logic gates, such as NAND, using this design alternative?

1.3 Non-Boolean Computation using Nanomagnets

The implementation of Boolean schemes in current computing technologies, such as CMOS, has been tremendously successful and is clearly on display in the billions of devices in use across the

globe, ranging from personal computers to that of supercomputers[31]. However, the Boolean approach to solving problems may not be the most efficient methodology in computation. A great example is the human brain, which utilizes a multitude of schemes to retain memory, process sensory information and compute complex questions on a daily basis[9]. In a traditional CMOS, transistors are arranged in blocks known as logic gates. Computation is performed with the implementation of algorithms that communicate the parameters needed for a certain operation to each logic gate in order to achieve a desired outcome. A computer therefore does not "naturally" seek a solution but instead relies on an algorithm, usually generated by a programmer, to perform computation. The operation of nanomagnets is instead dictated by their magnetic Hamiltonian. Under specific conditions, where nanomagnets are allowed to energetically relax, nanomagnets will find their minimum energy state. Therefore, one possibility of utilizing nanomagnets in computation would be to pose computational problems as magnetic Hamiltonians, where relaxing an array of nanomagnets would correspond to obtaining a solution[32].

A second motivation in seeking out a non-Boolean approach to computation is the possibility of finding solutions to NP-complete problems. Nondeterministic Polynomial time or NP type problems are a class of problems dealing with decision making where it may be easier to verify a solution to the problem than to obtain a solution[33, 34]. An example of an NP-complete problem is the traveling salesman problem (TSP)[35, 36]. In a TSP, the goal is to find the path between several "locations" that costs the least amount of "energy". In a typical TSP, a salesman is tasked to optimize the route to different homes in a given city such that he does not visit the same home more than once and the total length of travel is minimized. TSPs are often found in industries such as package delivery (e.g. UPS, FedEx and DHL), content delivery systems (e.g. Akamai) and urban planning (e.g. road constructions). These problems are usually computationally intensive and non-linearly scale with respect to the total number of "cities, nodes or homes". If we assume there are n numbers of "cities" in a TSP, then there will be a total of (n-1)! ways these cities could be connected. In a problem involving n=1000, the total possible ways to connect 1000 data points is 999!, which is $\sim 4 \times 10^{2564}$. Therefore a TSP type problem is computationally intensive, since a computer would need to check all the possible variations before finding the minimum path. However, a magnetic Hamiltonian may solve such a problem at a fraction of the time that it would take a traditional computer[37]. Indeed, this has shown to be the case where an NP-complete problem, Max-Cut, was solved using an Ising spin Hamiltonian[38]. Similarly, TSPs were also solved using nanomagnets[39, 40].

Finally, the use of nanomagnets to simulate natural phenomenon, such as the human brain is an exciting prospect to pursue. Currently, spintronic based neuromorphic computation[41, 42] is an emerging field and holds great promise for building magnetic artificial neural networks[43]. In addition, an alternative approach to constructing artificial neural networks using Ising Hamiltonians has recently been demonstrated[44, 45]. This latter approach to neural networks is of great interest and may hold potential for developing an artificial spin ice analogue to artificial neural networks.

The goal for this part of the PhD work is to identify different mechanisms incorporating ideas from artificial spin ice and construct building blocks to pave way to a non-Boolean scheme of computation.

The question is therefore: can we create computational building blocks using ideas from artificial spin ice to generate a weighted/probabilistic output, which could then be used in applications such as artificial neural networks?

1.4 Monopole Currents

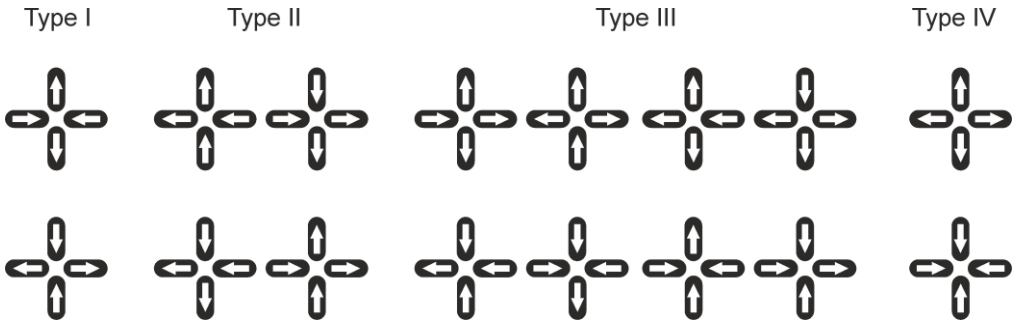

Figure 1.3: Four-vertex energy types. The energy increases with type number. Type I is the ground state and Type IV is the highest energy configuration, which is usually not observed in experiment. Type III vertices correspond to monopole excitations (non-zero magnetic charge at the vertex).

Nanomagnets arranged on a lattice, such as a square or hexagonal lattice, lead to the creation of local effective magnetic charges referred to as emergent magnetic monopoles[14, 17]. In the artificial square ice, there are several vertex configurations, which are shown in Figure 1.3, and the emergent magnetic monopoles occur at Type III vertices where there is a charge imbalance (Type IV vertices never occur). These monopole excitations occur in oppositely charged monopole-antimonopole pairs and are connected by a chain of reversed magnets referred to as a Dirac string[46].

Simulations indicate that monopole generation has a correlation with array parameters such as lattice spacing[14]. Subsequent work shows that monopoles can be deterministically injected by the incorporation of nanomagnets with modified anisotropy in arrays[46]. More recently, other modifications such as changing the position of one of the nanomagnets in an array and altering the thickness were also shown, using simulations, to have an influence on monopole generation[47]. In another experiment, attempts were made to nucleate monopoles along specific edges in an artificial square ice[48]. However, in the experiment, nucleation of monopoles occurred everywhere in the square ice, independent of the location. This was attested to the presence of disorder in the square ice associated with variation in the switching field and the position of nanomagnets. Experimentally it has also been demonstrated that, on increasing the applied magnetic field, the number of monopoles increases (Figure 1.4a and 1.4b).

In addition, the incorporation of nanomagnets with modified shape anisotropy influences the monopole generation and propagation as shown in Figure 1.4(c-e)[15, 49].

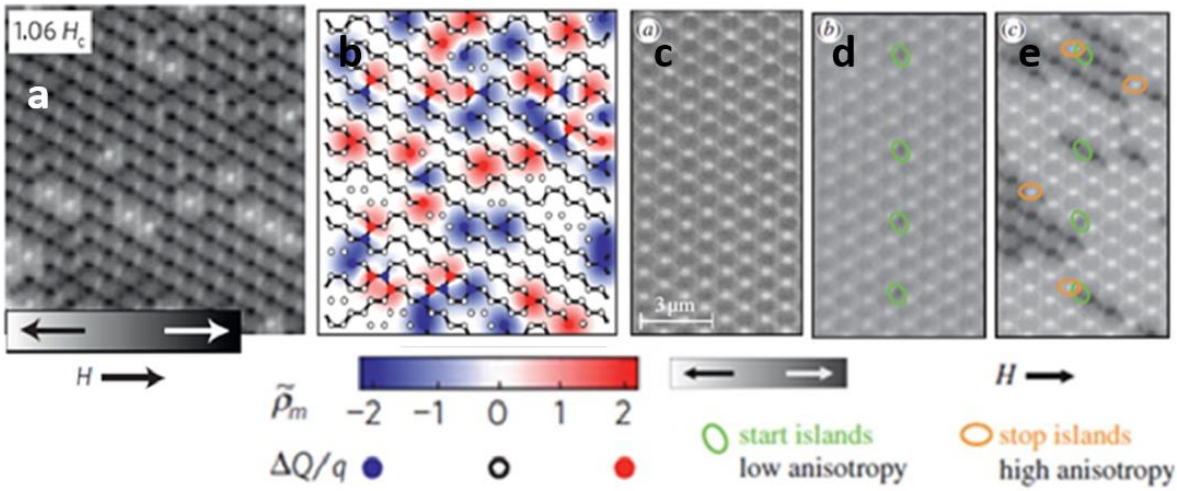

Figure 1.4: (a) X-PEEM image for an artificial kagome spin ice under the influence of external magnetic field and (b) the associated magnetic charge map. (c-e) X-PEEM images of the generation of monopole currents in an artificial kagome spin ice with low and high anisotropy islands, which defining locations of the nucleation (circled in green) and blocking (circled in orange) of monopoles, respectively. Figures adapted from Mengotti et.al. and Hugli et.al. [15, 49]

Another key experiment involved quantification of the vertex population in thermally relaxing artificial square ice as a function of time as shown in Figure 1.5[50]. The array transforms from a saturated state, prepared with a magnetic field and containing Type II vertices only, to the ground state with Type I vertices. This occurs via the creation of charge defect pairs that separate, so increasing the string length until the monopoles reach the array edge or another monopole. This dynamic process of monopoles separating can be considered as a monopole current. Recent theoretical work indicates that such monopole currents can be generated in finite-sized arrays and controlled by the incorporation of nanomagnets with modified anisotropy[46].

The key question here would be, is it possible to control the generation and evolution of monopole currents in artificial spin ice? If yes, can we implement them as part of a device?

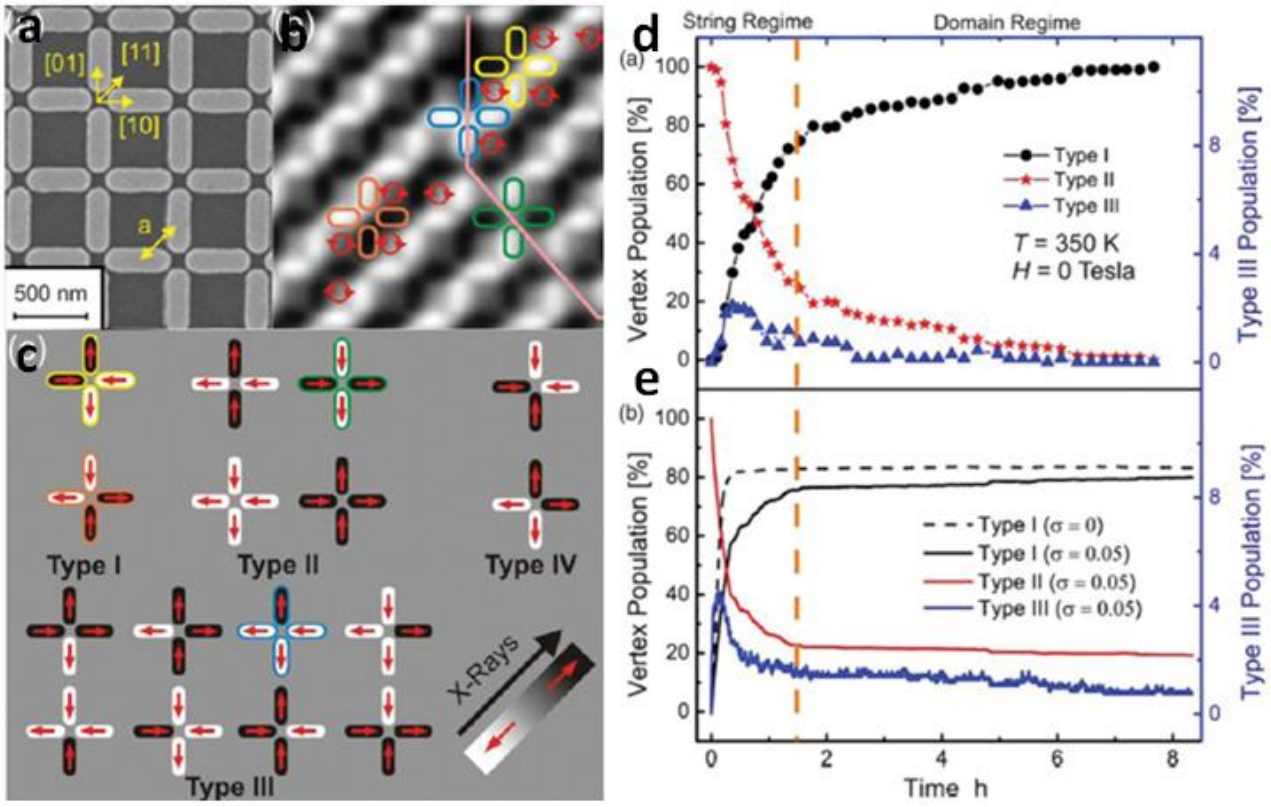

Figure 1.5: Artificial square ice along with their vertex types (a, b & c). (e) Temporal plot of vertex type starting with an array of Type II vertices, which transform into an array of Type I vertices: (d) experimental data and (e) numerical simulation. Figure adapted from Farhan et.al.[50]

CHAPTER 2: PHYSICS OF NANOMAGNETS

The thesis makes use of single-domain Permalloy nanomagnets and primarily utilizes heating to bring about moment re-orientation dynamics in arrays of artificial spin ice. In this chapter, I will provide a brief description of the energy terms governing these nanomagnets that give rise to specific properties, highlighting the conditions for the creation of single domain nanomagnets and their associated switching dynamics upon heating.

2.1 Physics of nanomagnets

The behavior of single domain nanomagnets is primarily governed by a magnetic Hamiltonian composed of the following energy terms: Exchange energy, Zeeman energy, Magnetostatic energy, and Anisotropy energy. The total energy in a nanomagnet can then be written as follows:

$$E = E_{exchange} + E_{Zeeman} + E_{magnetostatic} + E_{anisotropy} \quad (2.1)$$

Exchange Energy

The exchange interaction arises from Pauli's exclusion principle, which says that no two fermions (for example, electrons) may have the same set of quantum numbers. Since the Coulombic interaction energy is inversely related to the distance between two electrons, spins that have the same orientation will lower the energy of the system when compared to those that do not. The energy governing the interaction between two or more spins is given by the Heisenberg Model:

$$E_{heisenberg} = -2\sum_{i,j} J_{ij} S_i . S_j \quad (2.2)$$

Here, J_{ij} is the exchange integral describing the interaction between spins S_i and S_j. Minimization of electrostatic repulsion means that J_{ij} is positive for ferromagnets and negative for antiferromagnets.

Within the context of micromagnetics, the exchange energy is described as an integral over an arbitrary surface (Ω) as:

$$E_{exchange} = \int_{\Omega} \sum_{i,j} A_j \left(\frac{\delta m_i}{\delta x_j}\right)^2 dr \quad (2.3)$$

Here, $A(j)$ is the exchange constant, $\frac{\delta m_i}{\delta x_j}$ is moment contribution along an arbitrary direction, and r is the unit vector between two exchange coupled moments.

Zeeman energy

Magnetic moments in a ferromagnet material can be aligned along a particular direction with the application of an external magnetic field. This interaction of magnetic moments with an external field gives rise to the Zeeman energy term, which is:

$$E_{zeeman} = -\mu_0 \int M.HdV \quad (2.4)$$

Here, the E_{zeeman} is the volume integral of magnetization (M) and the applied field (H), with μ_0 being the permeability of vacuum.

The evolution of the orientation of moments under an applied field in a ferromagnet is described by the M-H (or B-H) hysteresis curve, where B is the magnetic flux density and is related to M by the expression $B = \mu_0(H + M)$. An example of such a curve is shown in Figure 2.1. A hysteresis loop begins at M, H=0 and, as H is increased, the moments start to orient towards the direction of the applied field leading eventually to a saturation state with all moments pointing in the field direction, at which point any further increase of H does not lead to an increase in M. As the field is reversed, the moments will undergo changes to align themselves parallel to the reversed field. This reversal of moments can occur as a coherent rotation or through the formation of magnetic domains. The primary components in a hysteresis loop are the remnant magnetization (the value of M at H=0, assuming the magnetic material started with a saturation state), coercivity (the value of H at M=0) and saturation magnetization (the largest M). Remanence corresponds to a stable magnetic state after the removal of an external field and is critical to applications such as magnetic memory. Coercivity relates to the field at which a magnet switches and therefore can be used to determine if a magnet is hard (high coercivity) or soft (low coercivity).

Magnetostatic Energy

Magnetostatic energy arises from the magnetization of the magnet itself, sometimes also referred to as the demagnetization energy (internal to the magnet) or stray field energy (external to the magnet). The minimization of the Magnetostatic energy ($E_{magnetostatic}$) in a magnet leads to the formation of domains, where $E_{magnetostatic}$ is given by:

$$E_{magnetostatic} = -\frac{\mu_0}{2} \int M.H_d dV \quad (2.5)$$

Here, the $E_{magnetostatic}$ is the volume integral of the demagnetization field (H_d) and M of the material.

Assuming the absence of electric currents, the demagnetization field can be derived from Maxwell equations as the following:

$$H_d = -\nabla\Phi \quad (2.6)$$

Here, Φ is the magnetic scalar potential and takes the following form:

$$\Phi(r) = -\int_V \frac{\nabla.\mathrm{M(r')}}{|r-r'|}d^3r' + \oint_S \frac{n.M(r')}{|r-r'|}dS' \quad (2.7)$$

Where, r and r' are the source and observational location of the stray fields, and n is the unit vector normal to the surface. The scalar potential equation is therefore a sum of contributions from volume (first part of the equation) and the surface charge densities (second part of the equation).

In case of a uniformly magnetized body, the first part of the magnetic scalar potential vanishes (*i.e.* $\nabla.\mathrm{M(r')} = 0$) and the demagnetization field is solely dependent on the potential from the surface charges. The demagnetization field is therefore reduced to:

$$H_d = -N_{ij}M_j \quad (2.8)$$

Here, N_{ij} is the demagnetization tensor and is represented by a 3×3 matrix. The values for N_{ij} are dependent on the shape of an object.

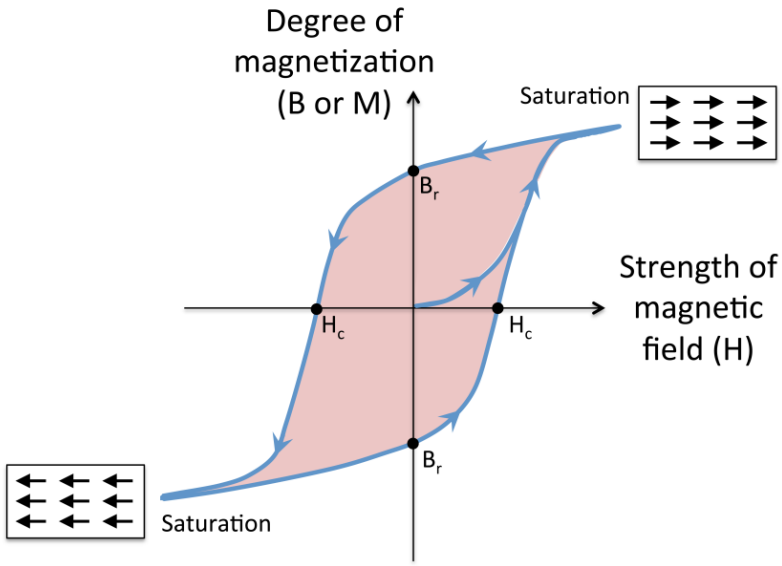

Figure 2.1: A schematic of a ferromagnetic hysteresis loop, detailing the different stages of magnetic moment response of a ferromagnet in an applied field. [Drawing by tem5psu, distributed under CC-BY 2.0 license]

Magnetic domains can form because the stray field is minimized as the number of domains is increased, as shown in Figure 2.2(a-c). The internal energy is lowered further when all the surface charges in a magnet are minimized by the creation of flux closure domains. Two possible flux closure configurations are shown in Figure 2.2(d-e).

Generally, spherical magnets with a diameter ranging from 10 – 100 nm are expected to support single domains, which is favored by the exchange energy at these length scales with the caveat that these numbers may change depending on the type of magnetic material[51]. In magnets where the shape deviates away from a sphere, for example nanorods and nanowires, the minimization of the magnetostatic energy leads to an alignment of the magnetization parallel to the long edge. This is referred to as shape anisotropy as described below.

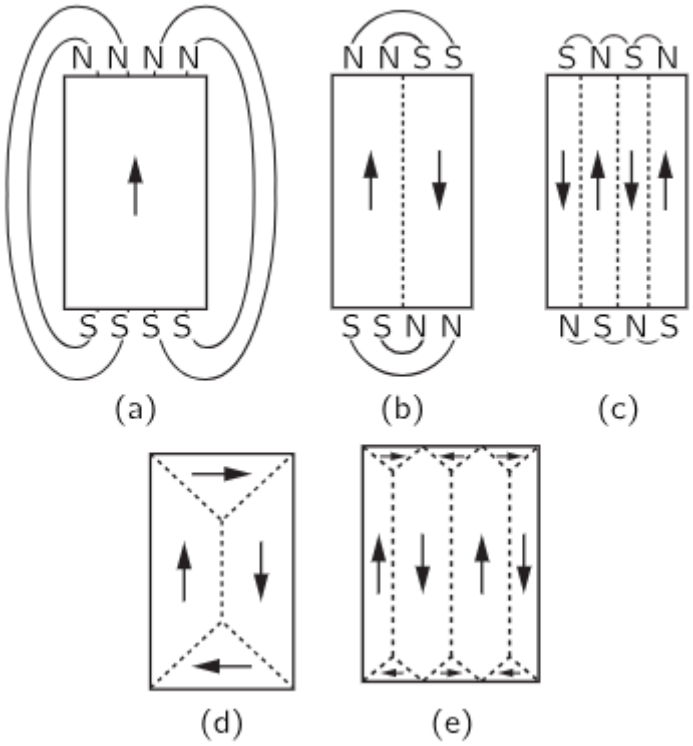

Figure 2.2: Different domain configurations in a ferromagnetic material. (a-c) An increase in the total number of domains leads to minimization of stray fields. (d-e) Flux closure states lacking stray fields and thus the least energetic configurations. Figure adapted from Feynman[52]

Shape Anisotropy Energy

There are a number of effects that lead to anisotropy in magnetic materials. For example, the Magnetocrystalline anisotropy is related to the ease with which a magnetic material can be magnetized along a particular crystal axis due to the preferential direction of the magnetic moment that results from the spin-orbit coupling. This is not relevant to the Permalloy nanomagnets implemented in this thesis, since the Permalloy is polycrystalline. Nevertheless, the magnets have an elongated shape, so the shape anisotropy is important. In particular, if the nanomagnets are not perfectly spherical, for example if they have an ellipsoid shape (Figure 2.3 inset), the poles of the magnet tend to align along

the direction of the physical long axis. Such an alignment is energetically favored since the poles are farthest apart and their magnetostatic energy is minimized. This thesis makes extensive use of nanomagnets close to an ellipsoid shape, with an appropriate magnetic volume i.e. where the exchange interaction ensures a single domain behavior, which thus could be modeled as individual moments.

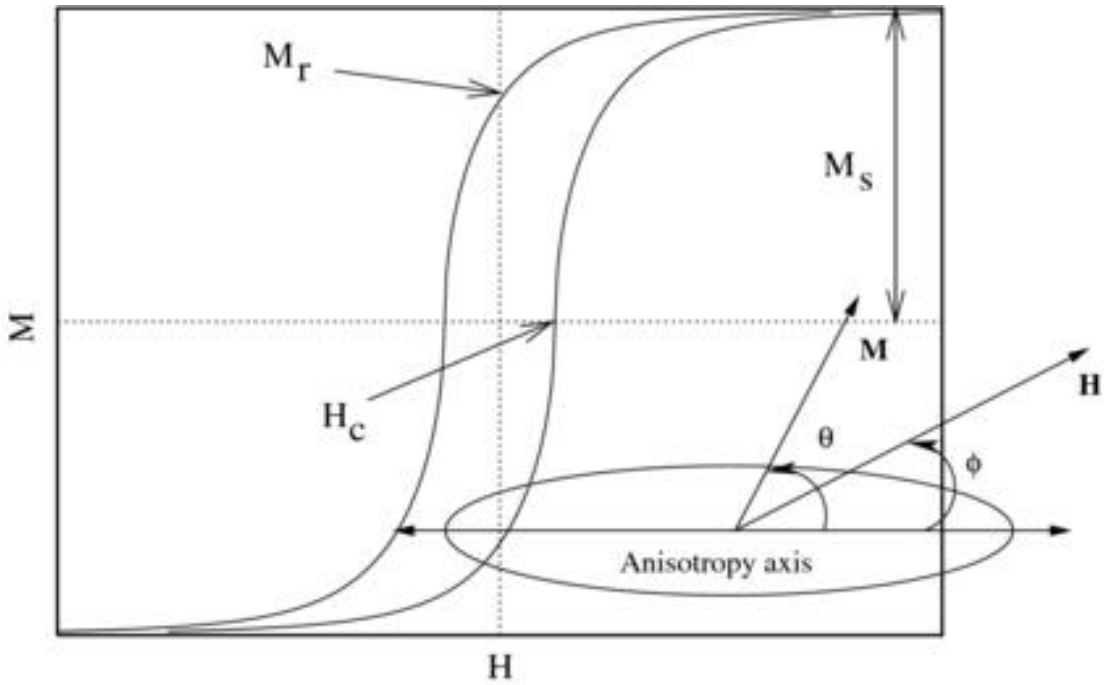

Figure 2.3: A schematic of a ferromagnetic hysteresis loop with an inset of an ellipsoidal shaped ferromagnet. Figure adapted from Tannous et al.[53]

In general, the anisotropy energy is given by:

$$E_{anisotropy} = KVsin^2\theta + higher\ order\ terms \quad (2.9)$$

Here, K is the anisotropy constant and V corresponds to the volume of the magnet. θ is the angle between magnetization and the easy axis (see Figure 2.3). However, the higher order terms are usually small and are neglected.

Ellipsoids under the influence of an external field are best described using the Stoner-Wohlfarth model. Within this model, the energy associated with an ellipsoid is:

$$E = KVsin^2\theta - MVHcos(\theta - \phi) \quad (2.10)$$

Here, φ is the angle between the applied field (H) and the easy axis (Figure 8).

The derivative of the energy with respect to θ would thus give the preferred orientation of the magnetization in the ellipsoid.

$$\frac{dE}{d\theta} = 2KVsin\theta cos\theta + MVHsin(\theta - \phi) = 0 \quad (2.11)$$

The equation has 4 solutions corresponding to two easy axes (minima) at θ = 0 and π, and two hard axes (maxima) at θ = π/2 and 3π/2.

2.2 Thermally active nanomagnets

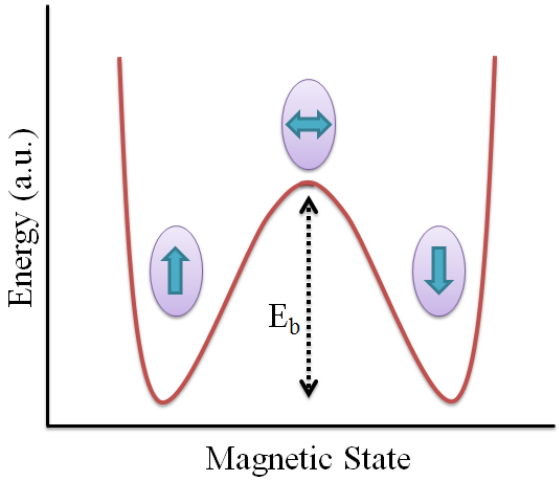

Figure 2.4: A schematic of an energy diagram for a ferromagnetic ellipsoid.

We make use of thermally active nanomagnets in this thesis to perform the experiments. This generally involves increasing the temperature of the sample to allow the moments from an initial state (set by an externally applied field) to relax to a final state (usually one of the degenerate ground states). Assuming coherent rotation of the magnetization (see Figure 2.4), the probability of the nanomagnets to change their moment orientation is approximated by[54]:

$$P \sim e^{-\frac{E_T}{kT}} \quad (2.12)$$

Here, k is the Boltzmann constant and T is the temperature. E_T is the energy associated with the switching of a nanomagnet and depends on factors such as the shape, thickness, and the type of magnetic material. In cases involving arrays of dipolar coupled nanomagnets, E_T would incorporate an additional energy term taking into account the interactions. Generally, we write

$$E_T = E_B + \frac{1}{2}\Delta E \quad (2.13)$$

Where E_B is the intrinsic barrier energy of an isolated nanomagnet, and ΔE is the change in dipolar energy associated with the nanomagnet changing its orientation. The ½ in the equation is an approximation and is generally held to be true.

Since the probability of a nanomagnet to change its moment orientation is a function of magnetic volume (from the anisotropy energy equation) and the applied temperature, care must be taken to engineer nanomagnets with the right magnetic volume, to observe magnetization dynamics at a time resolution (usually ca. 10 seconds) accessible to the X-ray Photoemission Electron Microscope (X-PEEM) used in this thesis to measure the magnetization dynamics.

CHAPTER 3: METHODS

Here, I will describe the fabrication methods employed to construct arrays of nanomagnets used throughout the thesis. With the primary goal of the thesis to perform computation using dipolar coupled nanomagnets, special attention was paid to the quality of the fabricated nanostructures. For this, a new fabrication protocol was developed to minimize the lift-off edges. In addition, a new motorized stage set-up was implemented in the thermal evaporator, in order to ensure repeatability in the thickness gradient associated with the deposited magnetic films. The introduction of a new motorized set-up meant that we needed to carefully calibrate the rate of motor and the rate of thin film deposition, in order to produce thickness gradients that were suitable for our experiments.

In the second part of the chapter, I will describe the two different magnetic microscopy methods that were implemented to determine the magnetic configurations in the structures, in particular, synchrotron X-ray Photoemission Electron Microscopy (X-PEEM) and Magnetic Force Microscopy (MFM).

Finally, I describe the analytical calculations that were performed to describe the experimentally observed results, in particular implementing simple dipolar Hamiltonian in a MATLAB, Monte Carlo and the Kinetic Monte Carlo (KMC) simulations.

3.1 Sample Fabrication

I used electron beam lithography (EBL) to fabricate the nanomagnet arrays. The process (Figure 3.1) begins with a clean silicon substrate, which is then spin-coated with polymethylmathacrylate (PMMA) polymer resist. The resist is then patterned, exposing it to a focused electron beam in a Vistec (EBPG 5000Plus) electron beam writer.

The exposed regions of the polymer are de-cross-linked and removed by spraying the substrate with a solution of IPA (Isopropyl Alcohol) + MIBK (Methyl Isobutyl Ketone) in a 3:1 ratio. This creates a negative of the pattern. A Permalloy thin film is then deposited on the patterned resist using a thermal evaporation system provided by Balzers. The evaporator has two voltage inputs, which can be used to resistively heat a tungsten boat that is filled with a desired material. In my case, we make use of one of the boats to heat Permalloy pellets for deposition. The second tungsten boat is used to deposit 2 nm of Aluminum as a capping layer to prevent oxidation of the Permalloy. During the course of the deposition, a quartz microbalance is used to monitor the thickness of the as grown films. A base pressure of 10^{-6} mbar is used for the deposition.

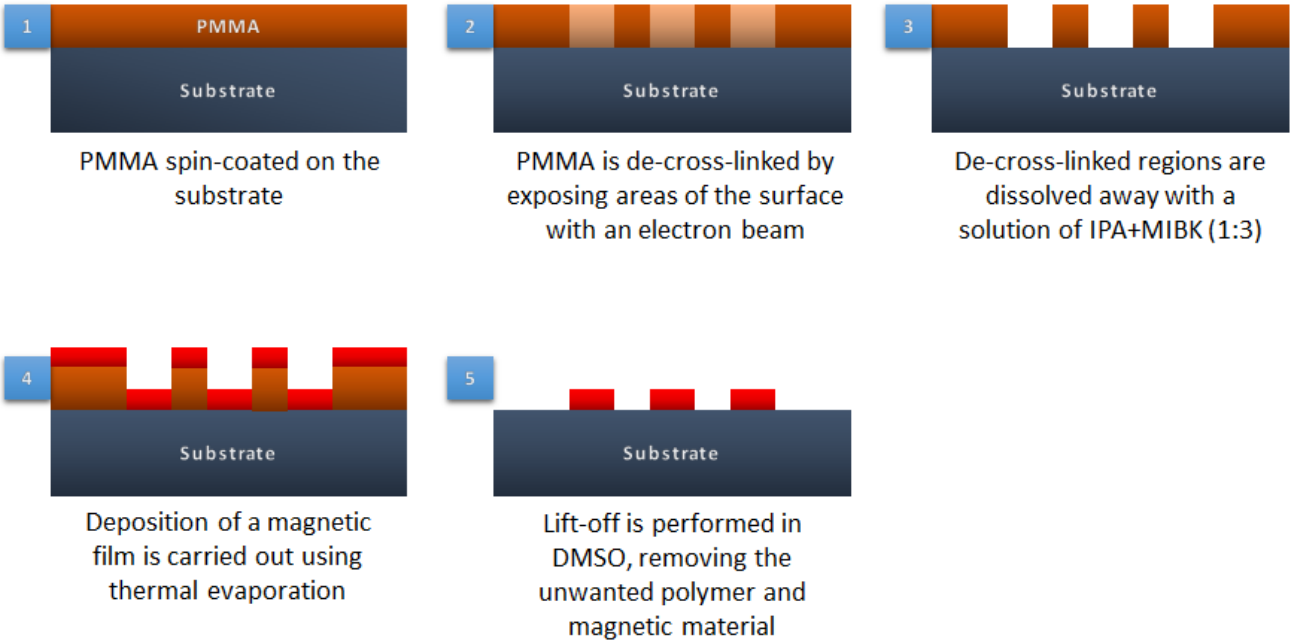

Figure 3.1: Step-by-step schematic detailing the process for fabricating nanomagnetic arrays.

Once the deposition is completed, I use a multi-step lift-off process to obtain pristine nanostructures. Initially, the sample is placed in a beaker of fresh acetone for a period of 20 minutes. This ensures that most of the polymer, visible to the naked eye, is removed. Once visually confirmed, the sample is transferred into a fresh batch of acetone and ultrasonicated for 5 minutes at a temperature of 40^{o}C. The time used for the ultrasound is flexible and is related to visual confirmation of how clean the surface looks. The sample is then transferred into a beaker containing DMSO (Dimethyl Sulfoxide). DMSO is a strong organic solvent and care must be taken to avoid direct contact and inhalation. The sample is then ultrasonicated for 15 minutes in DMSO at 50^{o}C after which it is transferred into another fresh batch of DMSO. The same process of 15 minute ultrasonication at 50^{o}C is repeated. After the completion of this, the sample is cleaned with De-ionized (DI) water and ultrasonicated for 3 minutes in a batch of Isopropyl alcohol (IPA). Transfer steps are performed rapidly and by spraying IPA constantly to avoid drying of the sample. The results from these steps are shown in Figure 3.2 for nanostructures with a thickness of 20 nm and with the smallest of spacing between them of 25 nm.

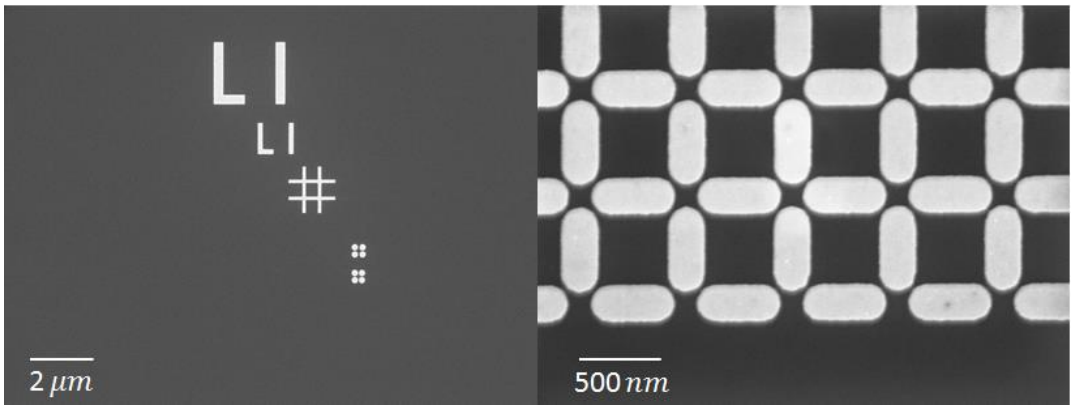

Figure 3.2: Scanning Electron Microscopy (SEM) images of nanostructures after employing the modified lift-off process. Both images indicate clean surfaces with minimal or absence of any lift-off edges.

3.2 Optimization of Sample Fabrication

Samples were manufactured using a specialized scheme to achieve a thickness gradient in the films. A thickness gradient gives us access to arrays of magnets with different energy barriers to switching. Therefore, at a given temperature, some structures have frozen moments and others exhibit dynamic moments where the switching frequency increases with decreasing thickness, so that we have access to different regimes.

Our current set-up for growth involves a motorized stage that brings the sample into the path of the thermally evaporated Permalloy to generate a thickness gradient (see Figure 3.3). The speed of the motorized stage movement has a direct consequence on the thickness gradient achieved, while the growth rate is kept constant. Films of varying thickness gradients were prepared by altering the applied voltage to the motor. AFM scans of the prepared films were used to determine the thickness gradient.

A plot of thickness vs distance (on the sample) is shown in Figure 13 for different samples in which Permalloy was deposited at different rates. Over 300 AFM scans were performed on more than 10 samples (not all shown in the Figure 3.4) to determine the optimum speed of the motorized stage, which was modified by changing the applied voltage to the motor with a constant evaporation rate of Permalloy. The aim was to achieve a thickness plateau in the 3±1 nm thickness range. An example of such a thickness plateau is seen in Sample 8 (grey data curve) in Figure 3.4, labeled as AFM Motor Test – Active, where thickness values are stable across a distance of 3 to ~4 mm. The presence of such a plateau is essential to obtain large number of statistics in nanomagnet arrays at a particular thickness. Such a thickness range is also suitable to observe moment reorientation dynamics in the X-PEEM at values slightly elevated from the room temperature.

A second aspect of sample optimization was the lift-off process used in the sample fabrication. In particular, with our requirement for precise control and reliability, it is imperative that we manufacture high quality samples. Previously, the typical lift-off procedure, as detailed by earlier group members, involved a multi-step process where ultrasound in acetone was carried out for at least 2 hours at a temperature of 40^{o}C. During the course of this lift-off, the sample was moved into a batch of fresh acetone every 15 minutes. However, upon closer inspection using SEM and AFM, it was found that the samples contained debris on their surface and the lift-off edges were quite high. The surface is highly rough and lift-off edges were in excess of 3 nm in height.

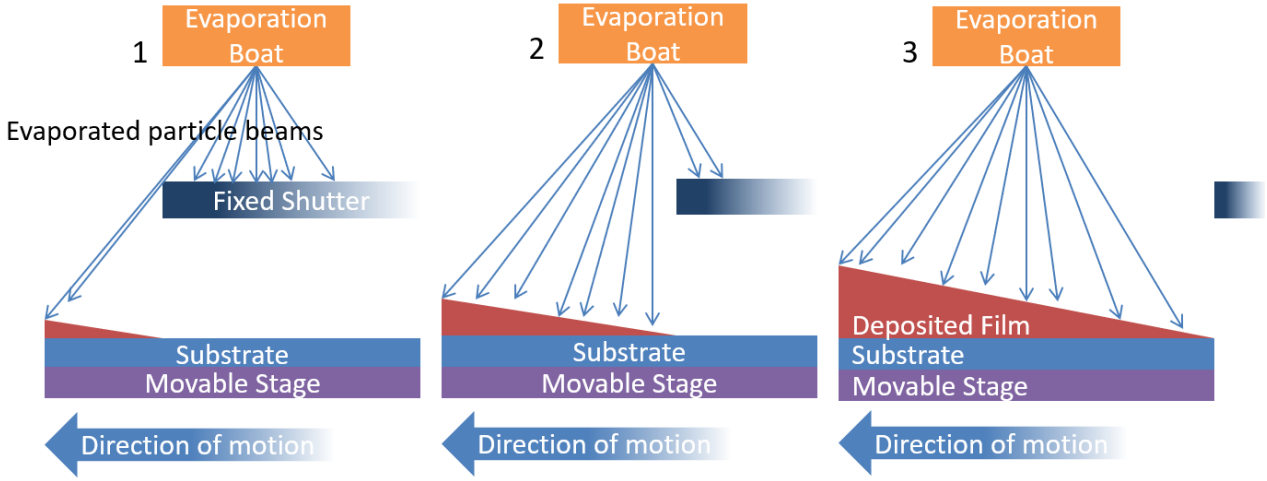

Figure 3.3: Schematic of film deposition. As the stage holding the substrate is moved into the path of the evaporated metal (1 & 2), a film with a thickness gradient is created (3).

To mitigate the debris and also lower the amount of time the sample spent exposed to air, we switched to the better solvent DMSO. The lift-off process is now completed in around 40 minutes, as detailed in the methods section, and the samples show a superior quality with minimal or no lift-off edges. We are unclear as to how the lift-off edges were reduced. This may be attributed to changes in the electron-beam writer dose parameters or in the low viscosity of DMSO. This improved sample quality was observed in our X-PEEM measurements where a smeared intensity at the edges was no longer seen in the optimized samples.

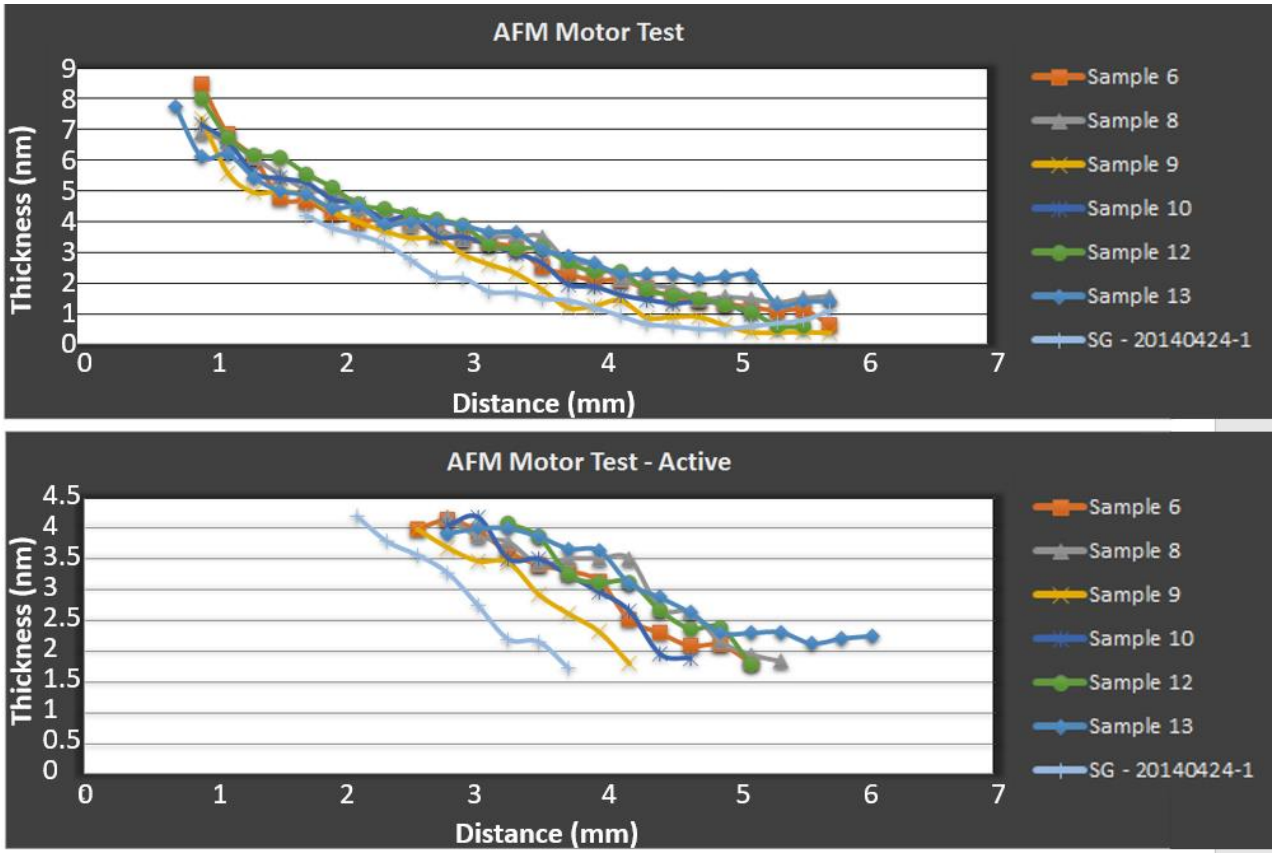

Figure 3.4: Optimization of thickness gradient using a motorized set-up. In the top panel (labeled AFM Motor Test), the thickness as a function of distance on the sample for several different samples is shown. In the bottom panel (labeled AFM Motor Test - Active), a zoomed version of the top plot with the thicknesses relevant to X-PEEM measurements is shown.

3.3 X-ray Photoemission Electron Microscopy (X-PEEM)

Our primary mode of experimentation involves using synchrotron x-ray radiation to image the slow dynamics of nanomagnetic structures.

The core principle behind imaging using X-PEEM involves the phenomenon of x-ray Magnetic Circular Dichroism (XMCD). XMCD is the change in absorption of circularly polarized x-rays when incident on a sample with particular magnetization orientation. Circularly polarized x-rays are obtained when relativistic electrons pass through an undulator with rows of permanent magnets (Figure 3.5a). The electrons follow an oscillatory path due to the Lorentz force generated by the magnetic fields to give different types of polarized light. Circularly polarized light with positive or negative photon angular momentum is obtained by changing the relative position of the rows with respect to each other by a quarter of the periodic length in either directions (Figure 3.5a). In an XMCD process involving a

3*d* ferromagnetic material such as Permalloy, a core shell ($2p_{1/2} - L_2$ edge or $2p_{3/2} - L_3$ edge) electron is excited into an empty *3d*-shell on absorption of a photon (Figure 3.5b)[55]. The excitation is dependent on the helicity of the incident photon where electron dipole transition rules forbid electron spin flips. The transition probability of Right circular photons (RCP) and Left circular photons (LCP) results in a transfer of opposite momentum to the photo-excited electrons. Here, the transition probability is governed by the Fermi's golden rule and therefore is proportional to the density of states in the empty d-shell. For example, at the L_3 edge, 62.5% spin up electrons are excited by RCP light and 37.5% spin down electrons by LCP light. In particular, it is the combination of the spin-polarized excited electrons and the empty, shifted spin-up and spin-down states that gives rise to the XMCD effect. Then, the XMCD effect depends on cosθ, where θ is the angle between incident x-rays and the orientation of the magnetic moments, meaning that maximum intensity is obtained when the incident photons are either parallel or antiparallel to the magnetization orientation.

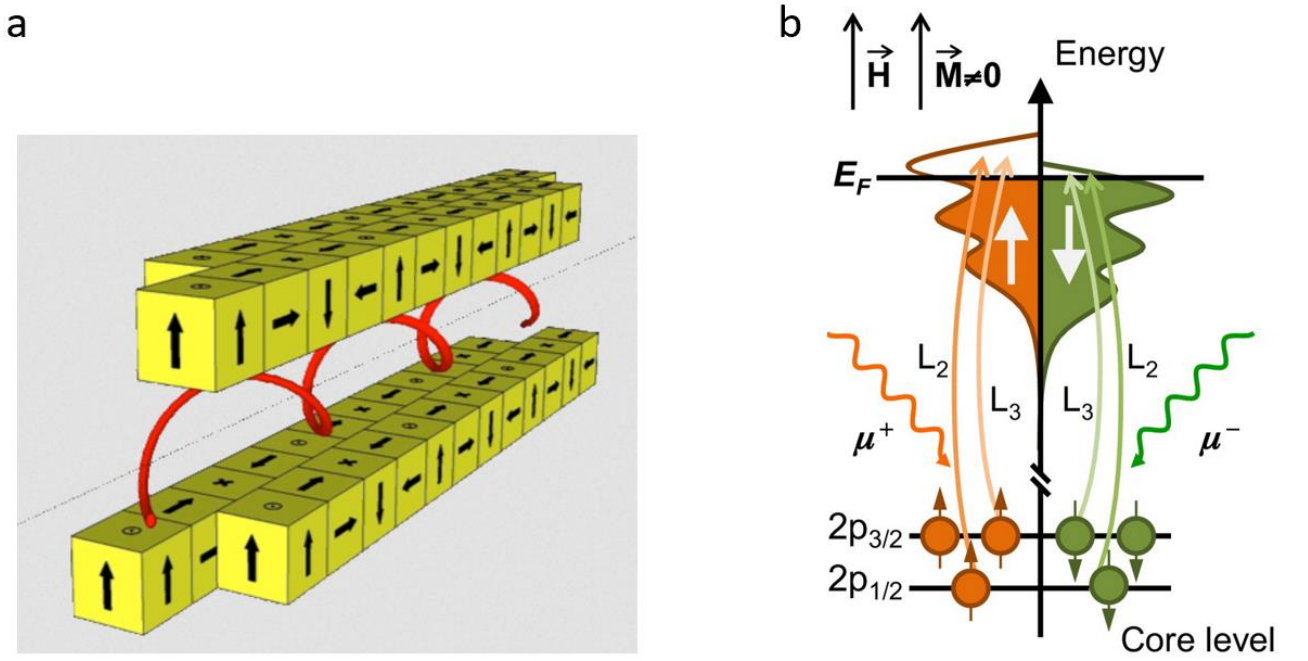

Figure 3.5: (a) Schematic of an APPLE II undulator in which a displacement between rows of permanent magnets leads to the production of circularly polarized light. (b) Two-step model describing the excitation of electrons from 2p core level to the empty d states. Figures adapted from Trieste[56] and van der Laan et.al[57].

X-PEEM takes the principle of XMCD further by adding the functionality of imaging via an electron microscope with the photo-excited electrons detected using a micro-channel plate detector (MCP) and a phosphor screen. For imaging, both LCP and RCP intensity images are obtained and, on dividing RCP and LCP intensity images, we obtain a magnetic contrast map that contains only magnetic information as shown in Figure 3.6.

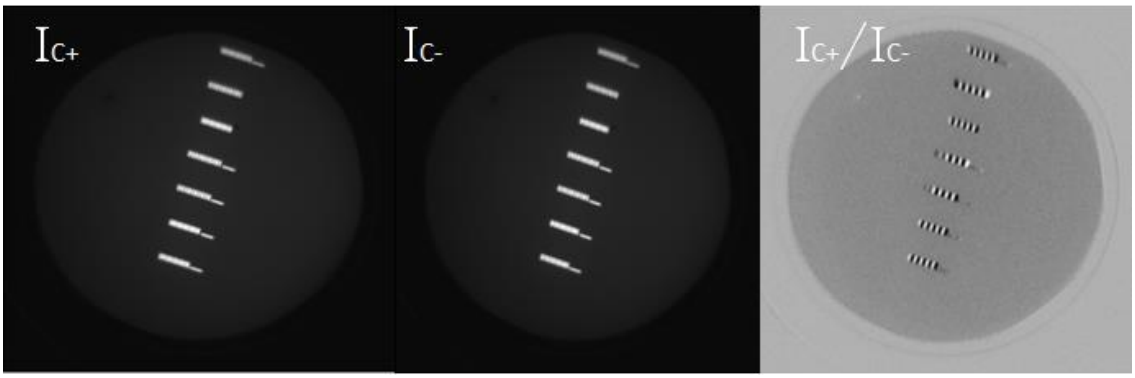

Figure 3.6: Intensity images (containing both magnetic and topographic information) from RCP (Intensity I_{C+}) and LCP (Intensity I_{C-}) incident x-rays and the division image (I_{C+}/I_{C-}) with the magnetic contrast only.

X-PEEM typically has a resolution of 50-100 nm[58], primarily related to chromatic and spherical aberrations, and the difficulty in implementing aberration corrected lenses. X-PEEM is therefore well-suited for imaging our structures with lateral dimensions down to 200 nm and edge-to-edge separations down to 30 nm. The X-PEEM set-up at the Swiss Light Source (Figure 3.7) enables us to perform experiments over a wide range of temperatures. Cooling is performed using liquid helium and the sample can be reliably cooled down to a temperature of 90 K. The sample could in addition be loaded onto a special holder with a resistive heating element that provides temperatures up to 1000 K.

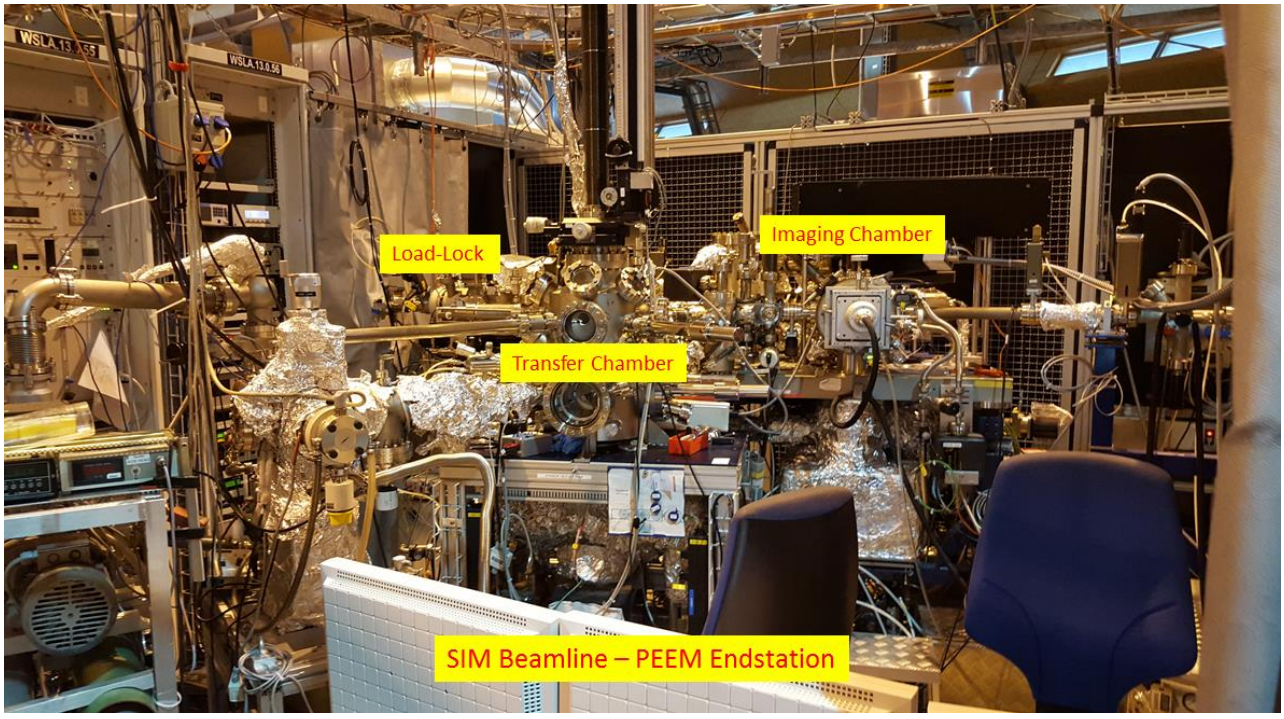

Figure 3.7: X-PEEM set-up at the Swiss Light Source.

It should be noted that the temperature dependent measurements had to be performed by carefully considering the amount of time it took to obtain LCP and RCP images for the nanomagnet arrays, which was often ~5 seconds. This is because, the application of heat increases the probability of changing moment orientations in the nanomagnets and therefore the change in temperature must be small enough so that any change in moment orientations can be successfully imaged.

3.4 Magnetic Force Microscopy (MFM)

Magnetic Force Microscopy (MFM)[59] falls under techniques broadly classified as Scanning Probe Microscopy (SPM). In a general scheme of SPM, a physical object, such as a sharp tip mounted onto a cantilever, is brought close to the surface of the material to be probed and, as the tip is run across the surface, the surface forces acting on the tip are recorded. The most commonly used SPM technique to probe the surface morphology in materials is the atomic force microscopy or AFM[60, 61].

An AFM works by running a sharp tip, made out of a material such as silicon nitride, across the surface of a sample of interest. While it is being scanned across the surface, a laser is shined on the cantilever and its reflection is detected on a photodetector. The small vibrations/changes in the cantilever leads to deflections of the laser beam on the photodetector that are registered as voltage signals, where the measured voltage is directly correlated to changes (in unit length; often nanometers) on the surface of the sample. A topographic profile of the surface of the sample is then obtained. Traditionally, an AFM tip would stay in contact with the sample surface or in a contact mode, while the scanning is performed. The disadvantage of a contact mode is that it requires the tip to be dragged across a surface, which may physically alter the sample. A non-contact mode is possible where the response of the tip to atomistic forces, such as the Van der Waals force, is leveraged for obtaining the topographic profile. However, such a non-contact mode may not always provide the best resolution, since the topography may not always be reflected by the Van der Waals interaction. Therefore, more recently, the use of tapping mode is the preferred mode of operation. In a tapping mode the cantilever is allowed to oscillate at a fixed frequency during the course of a raster scan. Such an oscillation would avoid the tip being dragged across the surface of the sample, while actively recording the surface morphology. Thus, a tapping mode is a superior alternative to traditional AFM.

An MFM is essentially the same as an AFM, but with the difference that the tip being used is made out of a magnetic material. The moment orientation in the magnetic tip is pre-set by either the manufacturer or locally using a large external magnet. The magnetic tip therefore behaves like a single-domain nanomagnet with its net magnetization pointed along the long axis of the tip. Therefore, as the tip is raster scanned across the surface of a sample, it feels forces that are either attractive or repulsive depending on the orientation of stray fields emanating from the surface. These attractive and repulsive forces are tracked using the photodetector and a contrast map is created. A schematic of an MFM set-up is shown in Figure 3.8.

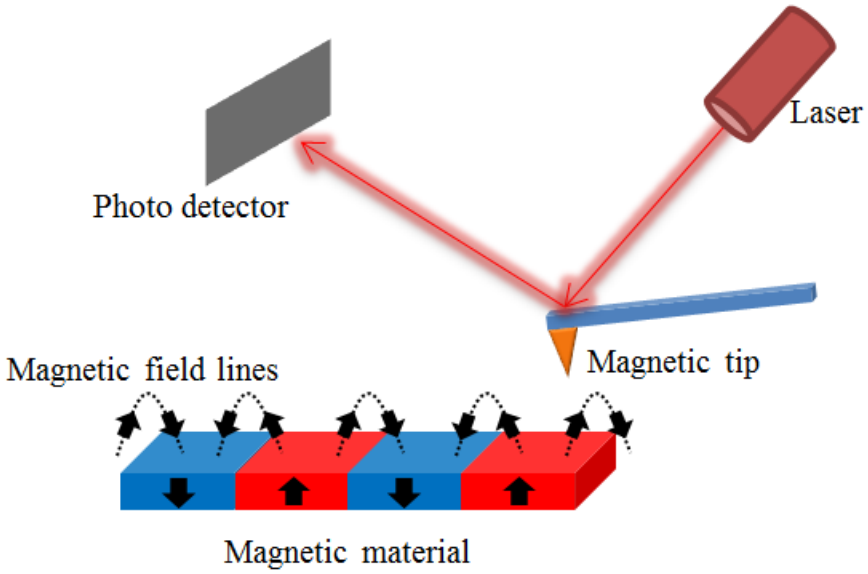

Figure 3.8: A schematic of the principle behind Magnetic Force Microscopy. The magnetic tip is brought close to the surface of a magnetic sample; the stray fields from the magnetic sample influence the motion of the magnetic tip. This motion is tracked using a photodetector and converted into a magnetic contrast profile using software.

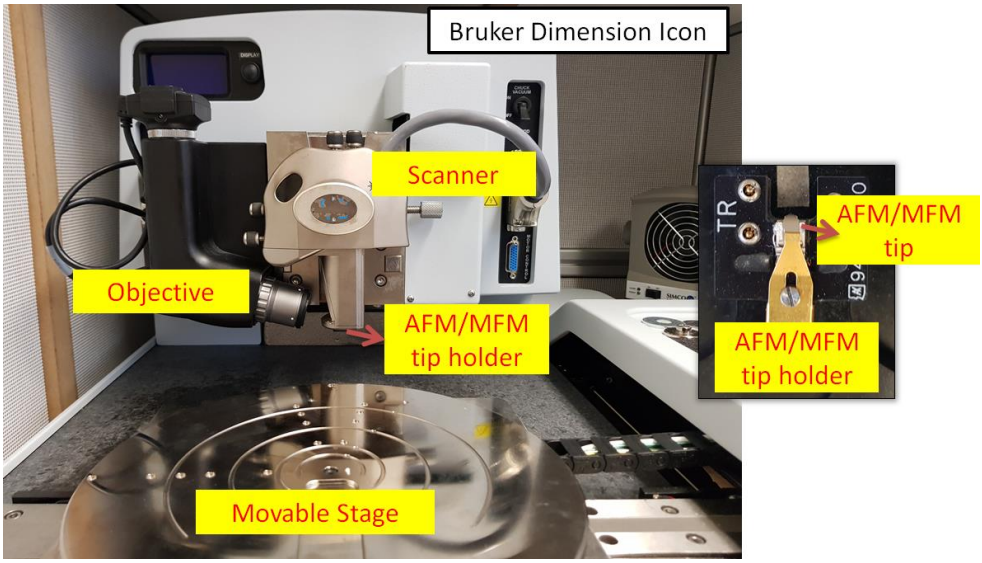

Figure 3.8: A photograph of Bruker Dimension Icon AFM/MFM instrument. Highlighted are key components on the instrument. In the inset is a close-up of the AFM/MFM tip holder assembly.

We use the Bruker Dimension Icon at PSI, housed in the Laboratory for Micro and Nanotechnology (LMN), to perform AFM and MFM measurements on our samples. A photograph of the microscope, in which key components of the device are highlighted, is shown in Figure 3.8. In the inset is a close-up view of the magnetic tip holder and tip assembly.

3.5 MATLAB, Monte Carlo, and Kinetic Monte Carlo Simulations

MATLAB energy calculations

Energy calculations of the gates were performed in MATLAB using a simplified dipolar Hamiltonian. Each nanomagnet was assumed to have its magnetic moment pointing along the long axis of the nanomagnet. Interaction between all moments was considered. The interaction between the nanomagnets was approximated using:

$$V(\hat{r}_{ij}, \hat{m}_i, \hat{m}_j) = -\left(\frac{\mu_0}{4\pi r_{ij}^3}\right)\left[3(\hat{m}_i.\hat{r}_{ij})(\hat{m}_j.\hat{r}_{ij}) - \hat{m}_i.\hat{m}_j\right] \quad (3.1)$$

where $\hat{r}_{ij}$is the distance vector separating the i^{th} and j^{th} point moments, $\hat{m}_i$ and $\hat{m}_j$. The total energy of the system is given by:

$$E_{total} = \frac{1}{2}\sum_{i,j=1}^{N} V(\hat{r}_{ij}, \hat{m}_i, \hat{m}_j) \quad (3.2)$$

Thermal average calculations

In this thesis, magnetic configurations in the arrangements of nanomagnets are associated with particular logic gate operations. Any deviation away from the expected magnetic configuration contributes to a less reliable logic gate operation. Therefore, in order to theoretically understand the reliability of a logic gate operation, the average occupancy of the corresponding magnetic configuration was calculated. The average occupancy for a particular site *i* is calculated to be:

$$< output > = \frac{1}{Z} \times \sum_i n_i e^{-\frac{E_i}{k_B T}} \quad (3.3)$$

Here, E_i is the energy of the state i, n_i is the n^{th} spin of the i^{th} configuration and takes a value of 0 or 1, k_B is the Boltzmann constant, and T is the temperature. The thermally averaged output, where 1 and 0 correspond to the two possible moment orientations, is calculated according to the partition function, Z, which takes the following form:

$$Z = \sum_i^M e^{-\frac{E_i}{k_B T}} \quad (3.4)$$

where M is the total number of configurations.

It should be noted that, for each logic gate operation, a particular number of magnetic moments were fixed in their magnetization direction. Therefore, M corresponds to the total number of magnetic

configurations assuming certain nanomagnets with fixed magnetization orientation. The thermally averaged outputs, *i.e* average occupancies for a particular site, were calculated for the input configurations of (11), (10), (01), and (00). Additional details pertaining to the parameters used in the thermal average calculations are described in section 5.2 of Chapter 5.

Limitations of simplified dipolar Hamiltonian

Since each nanomagnet has a spatial extent, the interaction between such nanomagnets will have a multi-pole structure, the leading order of which is the dipolar interaction (Equation 3.1). The use of the point dipole interaction is therefore an approximation that is expected to work for well-separated nanomagnets (the far field limit). For nearest neighbour nanomagnets (the near field limit), higher order multipole interactions would need to be included for accurate quantitative results. In the present case, use of the point dipole approximation is sufficient for a qualitative description of the energetics.

Kinetic Monte Carlo simulations

Monte Carlo (MC) simulations are a broad category of computational techniques that make use of random numbers to study large systems with high degrees of freedom[5]. Arrays of nanomagnets, where frustration plays a major role, are computationally suitable to be modeled as MC problems.

Monte Carlo simulations were performed by considering a particular initial state in an array of nanomagnets. At each Monte Carlo step, the magnetization of a randomly chosen dipole or multipole is randomly switched and the change in energy is calculated by using the relevant magnetic Hamiltonian, such as in equation 3.2. Additional details pertaining to the exact Hamiltonian used in the thesis is provided in section 7.3 of Chapter 7. The probability of the new configuration, *p*, was obtained using the Boltzmann factor $e^{-\frac{E_T}{kT}}$. Here E_T corresponds to the change in energy after the magnetization reversal (see equation 2.13). A random number, *r*, was then chosen between 0 to 1 and the step was accepted or rejected if $p>r$. The MC steps are repeated until the system reaches a low energy ground state. Several runs are needed, using different random number seeds, to check for statistical validity.

The use of MC simulations has the disadvantage of not including a time scale. Since many of the experiments carried out in this thesis are dynamic in nature, it is sometimes important to make use of a simulation scheme where dynamics are considered. Such a simulation scheme is the Kinetic Monte Carlo (KMC) method[6], which is a variation of MC (via Metropolis algorithm) simulations and was initially developed to study dynamics of vacancies in metallurgy[7].

The basic idea in a KMC simulation is that of a rate constant. Within the KMC framework, we assume that the system to be studied has enough time to equilibrate locally before the next transition,

thus satisfying the Markov property. The rate constant (Γ_{ij}) is the probability per unit time for a transition to occur, from current state (*i*) to that of the next state (*j*) and is given by:

$$\Gamma_{ij} = \nu e^{-\frac{E_{ij}}{kT}} \quad (3.5)$$

Here, ν is the attempt frequency and is typically at 10^9/s, E_{ij} is the transition energy from state *i* to *j* and includes the single particle switching barrier and the magnetostatic energy, *k* is the Boltzmann constant 8.6×10^{-5} eV/T, and T is the temperature. In problems involving large degrees of freedom, there is more than one possible j state. Therefore, we define a total rate constant that incorporates all the *j* states, as the following:

$$\Gamma_{total} = \sum_j \Gamma_{ij} \quad (3.6)$$

The probability of transition, after a time *t*, can then be written as:

$$P(t) = \Gamma_{total} e^{-\Gamma_{total} * t} \quad (3.7)$$

Once the rate Γ_{total} is known, a random number *r* is generated, where $r \in [0,1]$. An event *i* is then selected if the following condition is met:

$$\Gamma_{i-1} < r\Gamma_{total} \leq \Gamma_i \quad (3.8)$$

The event *i* is then executed based on equation 3.5, with a probability defined as:

$$P_{ij}(t) = \Gamma_{ij} e^{-\Gamma_{ij} * t} \quad (3.9)$$

After the event is executed, the KMC advances by a time $t+t_{next}$ by generating a random number r_{next} such that:

$$t_{next} = -\frac{1}{\Gamma_{total}} \ln(r_{next}) \quad (3.10)$$

All the rate constants are then recalculated, since the total number of available states may have changed after the advancement. The steps are then repeated until the maximum time has reached. The maximum time is usually set by the user and typically corresponds to the time associated with a particular experiment. In this thesis, the time considered for KMC simulation is usually less than 10 hours. The experimental parameters used in the KMC simulations are described in Section 6.5 of Chapter 6.

Therefore, with the complete knowledge of rate constants, we can accurately simulate the kinetics in a system using KMC

Finally, the metropolis algorithm in KMC simulations, as used in this thesis[8, 9], is implemented based on the Hamiltonian for the energy associated with transition from a state *m* to a state *l*:

$$E_{m\to l} = E_b + \frac{1}{2}(\Delta E_{m\to l}) \quad (3.11)$$

Here E_b is the energy of single particle switching, and $\Delta E_{m\to l}$ is the change in energy for the transition from state *m* to state *l*.

Thus, the KMC simulation only proceeds if the following condition is met:

$$E_b > \frac{1}{2}(E_m - E_l) \quad (3.12)$$

CHAPTER 4: OPTIMIZATION OF LINEAR CHAINS

In this chapter, I will detail the thermal and field relaxation experiments conducted on linear chains of nanomagnets. These experiments served a two-fold purpose: one was in assisting in calibration of the sample quality and the second to quantify, for the first time and in detail, the magnetic relaxation using a thermal protocol. The latter was useful in determining if thermal relaxation was the better route to transporting information in linear chains of nanomagnets, as opposed to a field protocol. Thus, even though this chapter is short, the work described here played the important role of determining the fabrication route followed in the construction of arrays throughout the thesis. More critically, I provide here a motivation for why traditional nanomagnetic logic is inherently error prone, which raises the need to find new routes to computation using nanomagnets.

4.1 Thermal and Field Protocol in Linear Chains

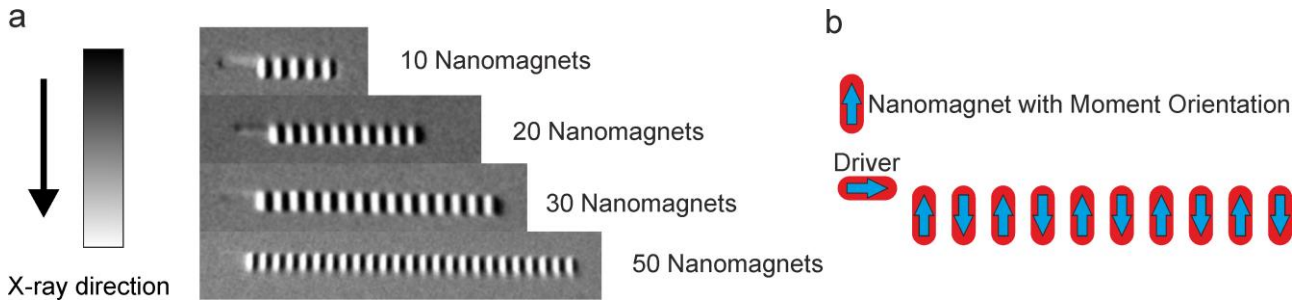

Figure 4.1: (a) X-PEEM images for a linear chain of nanomagnets consisting of 10, 20, 30 and 50 nanomagnets after application of a thermal protocol. (b) A schematic of a chain of 10 nanomagnets with their moments (in blue). Also shown is the driver, which is used as a control for the transfer information in the form of magnetic states.

For the study, nanomagnets of dimensions 470 nm × 200 nm with a thickness in the range of 1 to 15 nm were fabricated from a Permalloy thin film deposited on a silicon substrate. All nanomagnets were capped with a 1-2 nm-thick aluminum film to mitigate oxidation of the Permalloy. Preliminary experiments were performed on linear chains of nanomagnets controlled by an external nanomagnet labeled as a driver (Figure 4.1b). The driver has dimensions of 1 μm × 200 nm, with a higher energy barrier than the other magnets in the array, to ensure that it maintains its magnetization direction throughout the thermal protocol.

The thermal protocol is based on previous experiments on artificial spin ice with ultra-thin (≈3 nm) nanomagnets, where a temperature of 40-50 ^{o}C resulted in moment reorientations on a second timescale and relaxation of the magnetic configuration into the ground state over a period of 8 hours,

so occurring at a timescale suitable for dynamic imaging[62]. In a linear chain of nanomagnets, the degeneracy is greatly reduced from an artificial spin ice and therefore the time to achieve a ground state in a nanomagnetic chain will also be reduced.

The protocol involved using a resistive heating element to heat the sample in vacuum at 60 ^{o}C for 30 minutes without imaging in a preparation chamber connected to the X-PEEM chamber. The sample was then cooled down to room temperature. We imaged chains of nanomagnets with chain lengths of 10, 20, 30 and 50 nanomagnets and an inter-nanomagnet spacing of 30 nm and 50 nm. Additionally, the driver to chain spacing was varied with values of 30, 50, 100 and 150 nm. We performed two heating cycles and the nanomagnet chains were imaged between each heating cycle. We found that most defects, a pair of neighboring nanomagnets with moments pointed along the same orientation, were annihilated after the second cycle for chains of up to 50 nanomagnets (Figure 4.1).

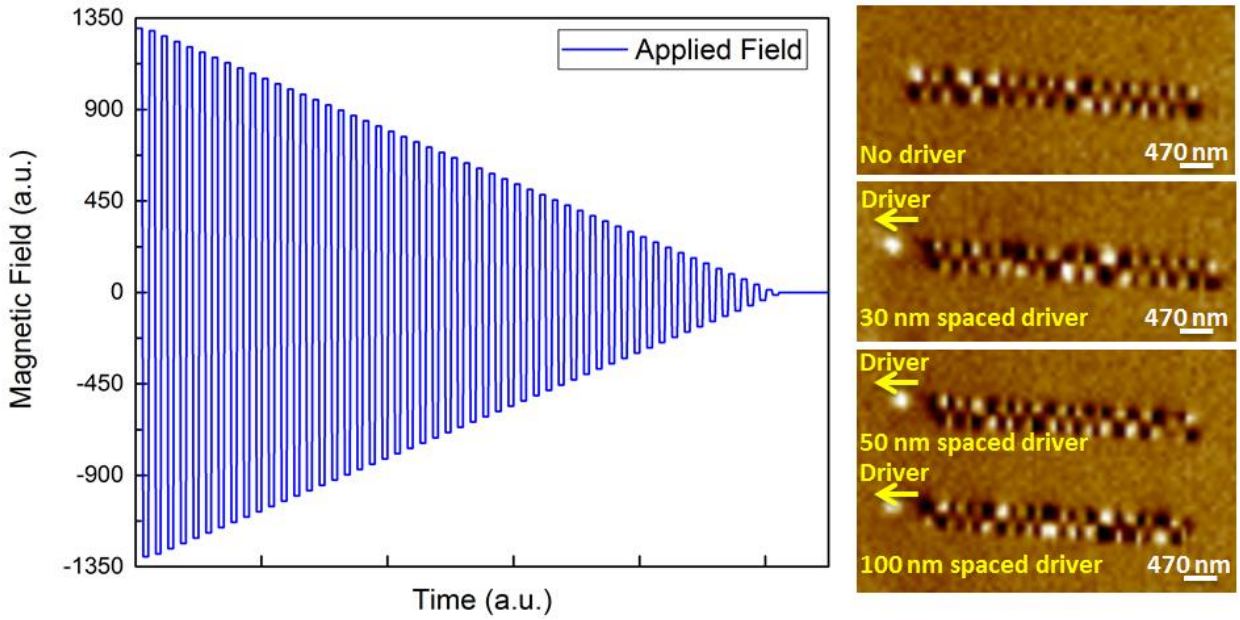

Figure 4.2: The demagnetization field protocol is shown on the left. To the right are MFM images of linear chains.

No clear correlation between driver spacing and error probability (defects/chain length) was observed. It should be noted that we have also measured the number of defects in chains of nanomagnets that we demagnetized at room temperature (Figure 4.2). Here an optimum driver spacing to minimize the error probability may have been found (Figure 4.3). The lack of correlation between the driver spacing and the error probability in the nanomagnet chains that underwent a thermal anneal is a result of the small error probability with the application of a thermal protocol. The highest error probability for room temperature demagnetization is 0.19 (for 30 nm spaced nanomagnets), whereas

for the thermal protocol this has a significantly lower value of 0.06 with only two defects or less per chain.

There was also no correlation between the spacing of the nanomagnets in the chain (30 or 50 nm) and the error probability using the thermal protocol. These results indicate that there is no need to have inter-nanomagnet spacing lower than 30 nm. In particular, a spatial resolution of less than 30 nm is often difficult to achieve when fabricating closely placed nanomagnets and thus such a lower limit of 30 nm on inter-nanomagnet spacing is useful from an experimental stand point. For demagnetized samples, there were many more defects/chain length confirming earlier work[63] where the nanomagnets were placed as closely as possible to improve reliability.

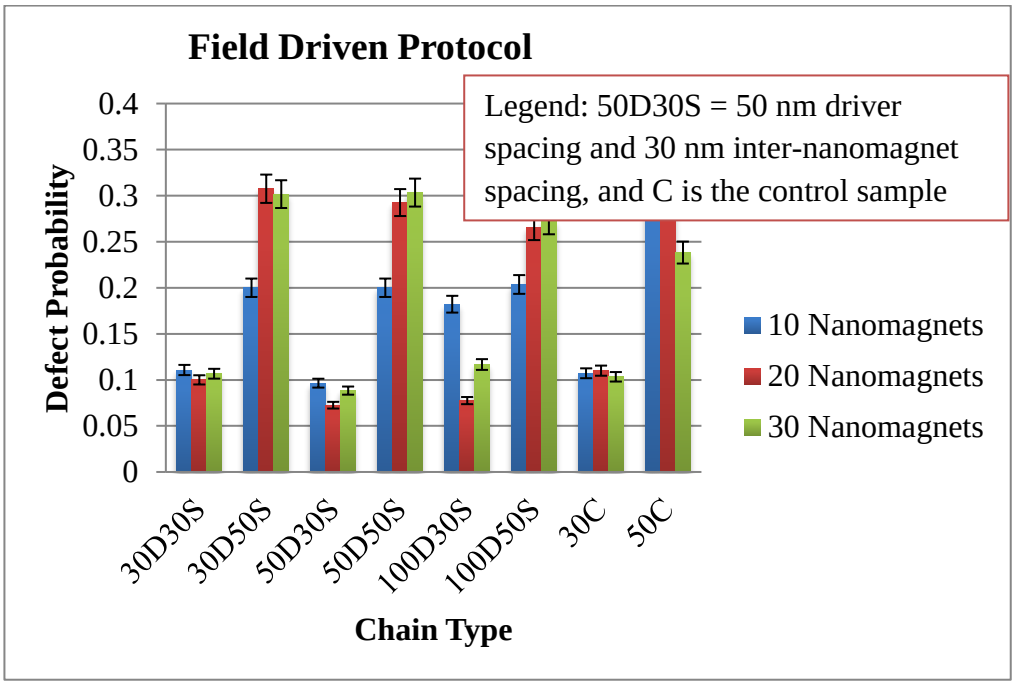

Figure 4.3 Error probability (defect/chain length) is plotted against increasing driver spacing from the chains. Each color represents different chain length, as shown in the legend. A total of 15 data points for each chain type were used to construct the plot.

It is therefore shown that the thermal protocol improves the reliability and the length of nanomagnet chains over which information can be transferred when compared to other published experiments. However, the use of linear chains of nanomagnets is fundamentally limited in its ability to perform reliable computation because there is a high probability for defects to linger. In Figure 4.4, the magnetic dipolar energies, normalized to kT at room temperature (295 K), and calculated for four nanomagnets in a linear and square configuration are plotted for all 16 magnetic states. In the linear chain, metastable defect states are present, which require a single spin flip transition to a higher energy state before relaxing to a ground state. For example, the blue square in Figure 4.4 in the linear chain

plot is that of a metastable state that would require a spin flip transition to the yellow energy state before relaxing to a ground state. In contrast, the square configuration does not possess any metastable defect states that require transition to a higher energy state before relaxing to a ground state. Therefore, the square configuration has design that is superior to that of the traditional linear chains for use in computation where operational reliability is critical.

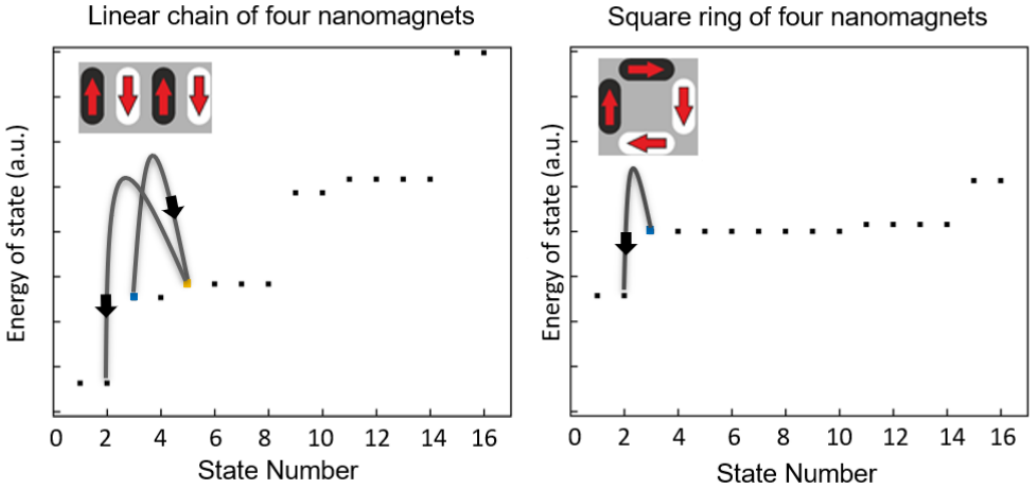

Figure 4.4: Calculated dipolar energies for a linear chain of four nanomagnets and a single square of four nanomagnets. The y-axis is the normalized energy and the x-axis is the state number for different moment configurations. Shown using a blue solid square in the linear chain plot is a metastable state from which the relaxation to a ground state would only occur at a higher energy state shown in yellow, assuming single spin flips. In the square ring, a transition to a higher energy state is not required for relaxation to a ground state.

Similarly, a calculation of dipolar energies was performed for the traditional nanomagnetic logic gate. Such a plot is shown in Figure 4.5 where the y-axis is the normalized energy with respect to kT at a room temperature of 295 K, while the x-axis corresponds to all the possible states. A, B, C, D, E, F, G, and H in Figure 4.5 are magnetic force microscopy images of different logic operations. Upon examining the energies of each logic operation in the energy vs state number diagram, it can be seen that there are many metastable states in which a relaxation (or operation) of the logic gate may yield incorrect operations. For example, the two low energy states of B and F occur close to other metastable states and therefore an operation involving either B or F may not always yield the correct output. This is likely the culprit for the 50% reported operational reliability in these gates[5].

I will note here that the above discussion assumes a nanomagnet array in which the single particle switching barrier (E_b) is expected to remain constant. However, the presence of metastable states and subsequently the relaxation of magnetic moment reorientations from an initial field set state

to that of a final low energy ground state, could be significantly altered by modifying properties in individual nanomagnets.

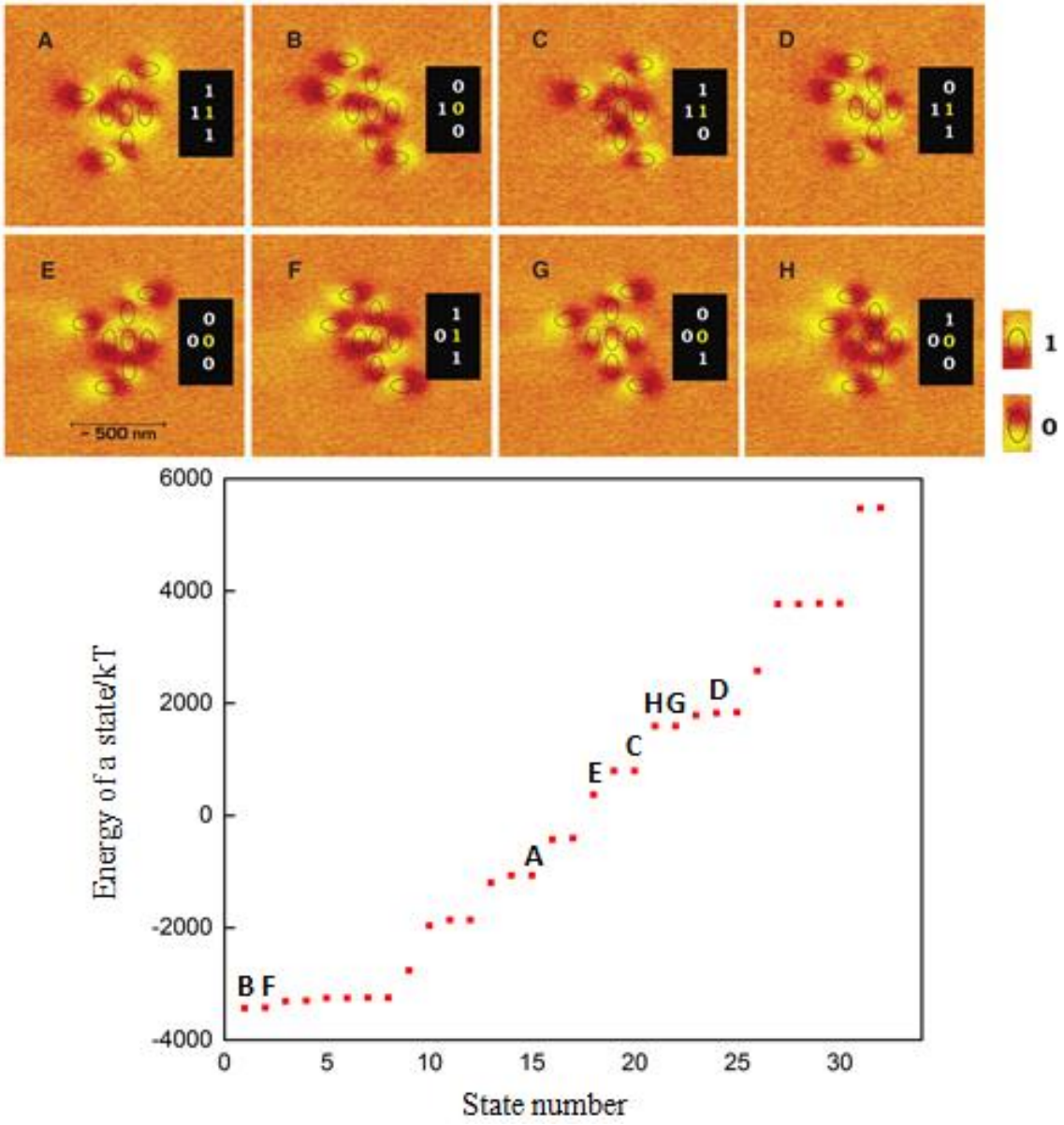

Figure 4.5: (A-H) are Magnetic Force Microscopy (MFM) images of different logic operations. The MFM images were adapted from Imre et al.[5] The lower plot shows all possible magnetic configurations for the logic gate in (A-H) as a function of energy. Indicated in the plot are energies of the gate operations corresponding to the MFM images.

Such a targeted approach, in which the E_b of a nanomagnet is altered by either choosing a magnetic material with a different M_s or, that of shaping the nanomagnet to have a lower E_b by making

it thinner, would be a viable alternative to the design approach taken in this thesis. Therefore, in a nanomagnet array with a constant E_b, *i.e.* all nanomagnets are expected to overcome an initial E_b during a transition, the transition probabilities from one magnetic configuration to another is assumed to be primarily driven by the difference in dipolar energies.

Based on the experimental results and theoretical work detailed up to now, a renewed look at implementation of nanomagnets for computing is therefore needed. As shown in Figure 4.4, the square ring design with a lack of low energy metastable states makes it an ideal candidate for use in computation. Similar closed geometries such as hexagons and pentagons would also be viable candidates.

Acknowledgements: I performed the sample fabrication, SEM, AFM, demagnetization, and MFM measurements. X-PEEM measurements were performed by me with assistance from Armin Kleibert and Jaianth Vijayakumar of the Swiss Light Source.

CHAPTER 5: BOOLEAN COMPUTATION WITH ARTIFICIAL SPIN ICE

Earlier, in the introduction part of this thesis, I have defined a series of questions for each of the three sub-topics that my thesis would deal with. The following are the questions posed for the topic of Boolean computation using artificial spin ice:

"The key question here is, is there a viable design alternative to perform nanomagnet based Boolean computation using ideas from artificial spin ice? Can we demonstrate Boolean logic gates, such as NAND, using this design alternative?"

In order to incorporate the ideas of artificial spin ice into nanomagnet based computation, we had to look into different artificial spin ice lattices for inspiration. One of most studied and "simplest" lattice configuration is that of the artificial square ice. An artificial square ice involves the placement of nanomagnets on a square lattice, with distances between each nanomagnet being small enough (usually ~50 nm) to generate strong dipolar-dipolar coupling [8]. Upon closer examination, we could reduce the square lattice into 2D, 1D and 0D objects. Here, 0D would be a single square ring, 1D would be a chain of square rings and 2D would be the square lattice. Computation requires two base components to operate: (1) a mechanism to support the transport of information across a distance and (2) a computational unit or a logic gate that performs a specific set of Boolean operations. In this chapter, I will describe the use of a 1D square lattice, a chain of square rings, to transport information across a distance. I will then show how logic gates were constructed to perform computation. Finally, I will conclude with a proof-of-concept approach to creating complex circuits using more than one logic gate. All the experiments were carried out at the SIM beamline in the SLS, making use of X-PEEM to image the nanomagnets. Further, thermal average calculations were used to support the described experimental data.

5.1 Transport of Information

In a typical nanomagnetic logic scheme, transport of information is governed by a linear chain of nanomagnets (Figure 5.1a) where the desired output is gathered from the magnetic state of the nanomagnet at the end of each chain. The moment orientation of the input nanomagnet, which was set by an applied field, is usually the input state that we desire to transport across a distance. Upon relaxation of the magnetic moments in the chain, achieved by the application of an oscillating magnetic field or heating the sample, the magnetic moments orient themselves along their easy axis to minimize their energy by accessing one of the two degenerate ground states with all neighboring moments aligned head-to-tail. If the input nanomagnet is constructed to have a higher magnetic moment, which can be achieved by changing the nanomagnet's magnetic volume or the use of a different magnetic

material with higher coercivity, then the degenerate state accessed by the chain of nanomagnets will be biased by the orientation of the input nanomagnet. Thus, we can reliably access the input state across a distance by probing the magnetization orientation of the output nanomagnet.

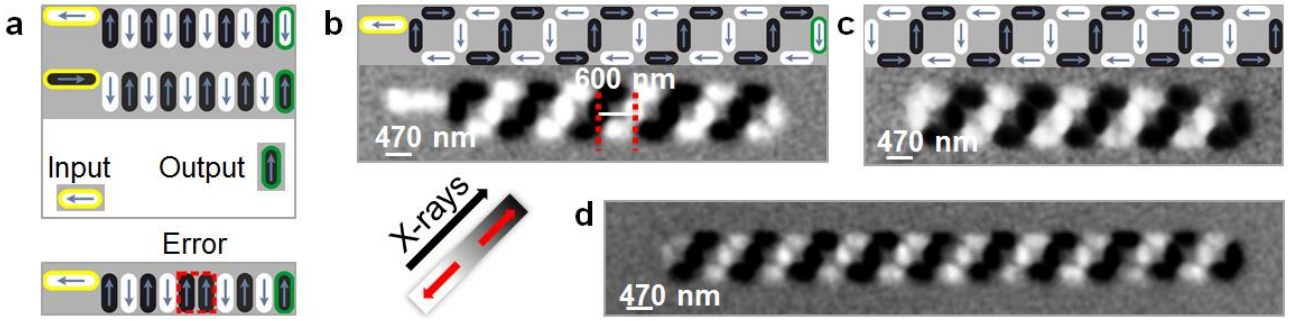

Figure 5.1: (a) Schematic of a linear chain of nanomagnets consisting of an input (in yellow) and an (output), along with an illustration of a possible error arising in a linear chain. (b-c) A chain of square rings whose chirality is influenced by the moment orientation of an input nanomagnet as compared to a chain of square rings without the influence of an input. (d) The longest chain length imaged, which displayed a ground state.

Using a similar geometry to the linear chains, we fabricated chains of nanomagnets, made of Permalloy, using square rings (Figure 5.1 b-d and Figure 5.1a) as described in the methods section. Each nanomagnet has a length L = 470 nm, width W = 200 nm and the thickness ranged from 1-15 nm. The center-to-center distance between two opposing nanomagnets in a single square ring is 600 nm. The input nanomagnet had a length L = 1000 nm and a width W = 200 nm. The initial state in a chain of square rings was set by an external field (~100 – 200 mT) applied along the direction of the X-rays (shown in Figure 5.1. The chains were then allowed to thermally relax by heating the sample with a filament placed beneath the sample. For a thickness of ~3 nm, we require a temperature of ~70 ^{o}C to facilitate the moment reorientations of the nanomagnets so that the square chain accesses one of its two degenerate states. The higher magnetic volume in the input nanomagnet means that during the course of the experiment, the direction of the magnetic moment in the input nanomagnet remains stable. Therefore, the accessed degenerate state in the chain of square rings is biased to the orientation of the input nanomagnet.

We tested a total of 40 chains of square rings, across two different samples, with varying chain lengths consisting of 4, 9, 14 and 19 square rings. We observed that the total number of chains with no defects (i.e. where the relaxed state is the ground state) to be 100%, 70%, 60% and 50% for chain lengths of 4, 9, 14 and 19 square rings, respectively. We attribute this trend of decreasing yield as the chain length is increased to the longer time required to relax chains with larger number of square rings. Thus, an optimized relaxation protocol with an increased time for thermally relaxing the nanomagnets would lead to an increased yield in larger chain lengths. With this experiment, it was demonstrated that the chain of square rings could support the transport of information across varying distances. More

importantly, it was experimentally demonstrated that it is possible to transport information across long distances (~11.4 μm for the chain consisting of 19 square rings; Figure 5.1c) that are not typically observed in traditional nanomagnetic logic [5].

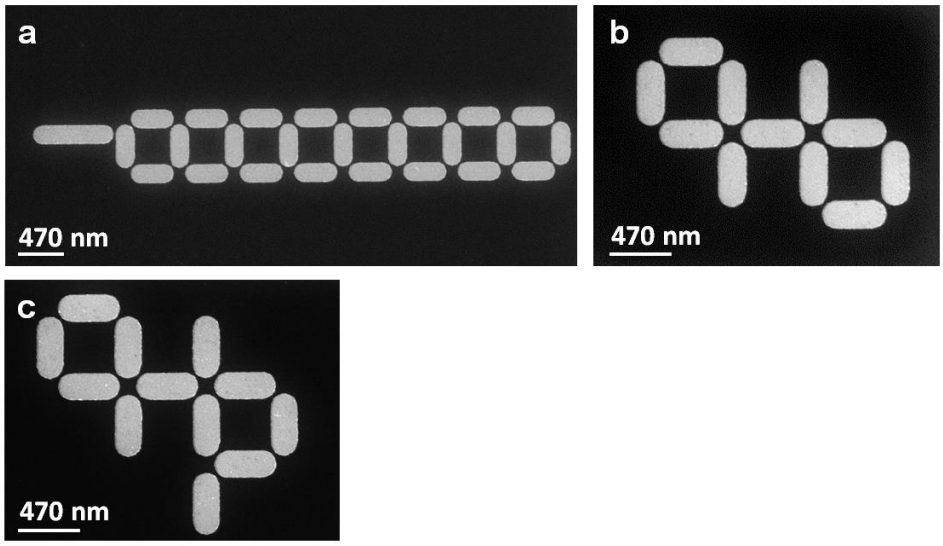

Figure 5.2: (a) SEM image of a chain of square rings with an input nanomagnet. (b-c) SEM images of a pseudo-NAND and NAND logic gate.

Following the demonstration of transport of information using a 1D artificial square ice structure, the next logical step was to build a computational unit in the form of a logic gate using square rings.

5.2 Logic Gates

A key idea when designing a logic gate to perform Boolean algebra is to satisfy the NAND logic (or a NOR logic). This is because a NAND gate is considered functionally complete, which means that all Boolean operations can be performed using a combination of NAND gates [64]. We initially built the pseudo-NAND gates shown in Figure 5.2b. Each gate comprises of two inputs (ii) and an output (o) defining the logic operation (iio), in which each "i" and "o" can be either zero or unity reflecting the moment orientation (up or down) of the input and output nanomagnets. In a functionally complete NAND logic gate with two inputs, the logic operations are (001), (110), (101) and (011). However, the gate is a pseudo-NAND gate because the operations involving inputs of (10) and (01) are unstable. The unstable nature of (10) and (01) operations arise due to a lack of a clear ground state for each set of inputs. This becomes clear when looking at the difference in dipolar energies associated with the magnetic state for each logic operation and the "closest in energy" defect state, which corresponds to a state with one nanomagnet with a different moment orientation to that in the preferred arrangement of moments for each logic operation. It should be noted that all dipolar

energies were calculated by assuming a simple magnetic Hamiltonian as described in the Methods chapter of this thesis. We find that gate operations of (001) and (110) have an energy gap to the closest defect state of -1.16 × 10^{-18} J, whereas gate operations of (100) and (011) have an energy gap of -9.29 × 10^{-19} J. Since the transition rate between two moment configurations is proportional to the Boltzmann factor $e^{-\frac{E_T}{kT}}$, a larger energy gap would mean a lower transition rate and vice-versa (see Equation 2.13); it is implied that the there is an additional E_b, single particle switching barrier, that the nanomagnets must overcome between different transitions. A detailed discussion on the role of E_b and the transition probabilities is provided in Chapter 6.1. Thus, operations involving (10) and (01) inputs are less stable than those involving (00) and (11), since (100) and (011) operations have a higher transition rate to a metastable state. Intuitively, this discrepancy in the energy gap can be understood as arising from magnetic charge creation in the logic gates during a Boolean operation (see Figure 5.3). Whereas in gate operations of (001) and (110), the magnetic charge at the vertex involving the second input and the output is 0q, a Type I variety, the magnetic charge at the same vertex for (10x) and (01x) operations is a ±2q, an energetically higher Type III variety. Additionally, we show this instability in (10x) and (01x) gate operations using thermally averaged calculations (Figure 5.4 a-d), for nanomagnets with magnetization M_s = 200 and 800 kA/m for temperatures in the range 0 – 800 K.

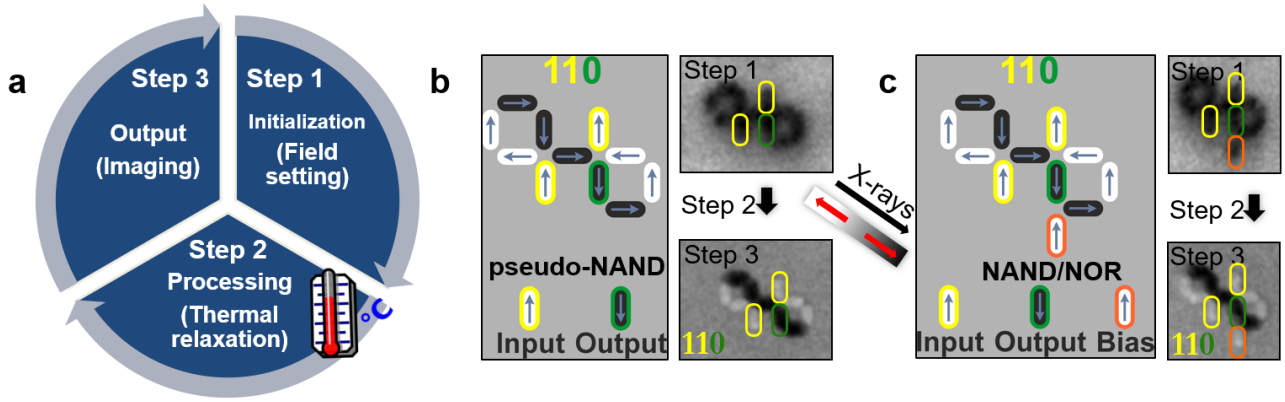

Figure 5.2: (a) Schematic of the procedure for computation within the X-PEEM experimental chamber. (b) Schematic and X-PEEM images of a pseudo-NAND gate performing the (110) logic operation. (c) Schematic and X-PEEM images of a NAND/NOR gate performing a (110) logic operation.

The thermal average occupancy of a particular logic operation, for example (110), for a given set of input constraints is correlated with the probability of a successful gate operation. The calculations were performed by assuming that each nanomagnet has dimensions of 470 nm (L) x 200 nm (W) and a thickness of ~3 nm. The magnetization was varied from 200 kA/m to 800 kA/m, with the latter corresponding to the bulk saturation magnetization of Permalloy. Typically, the average occupancy asymptotically reaches 0.5 with an increase in temperature. Therefore, the thermally averaged outputs

provide us with a barometer to test against, in order to build a device with parameters that could reliably operate at ambient conditions, such as room temperature.

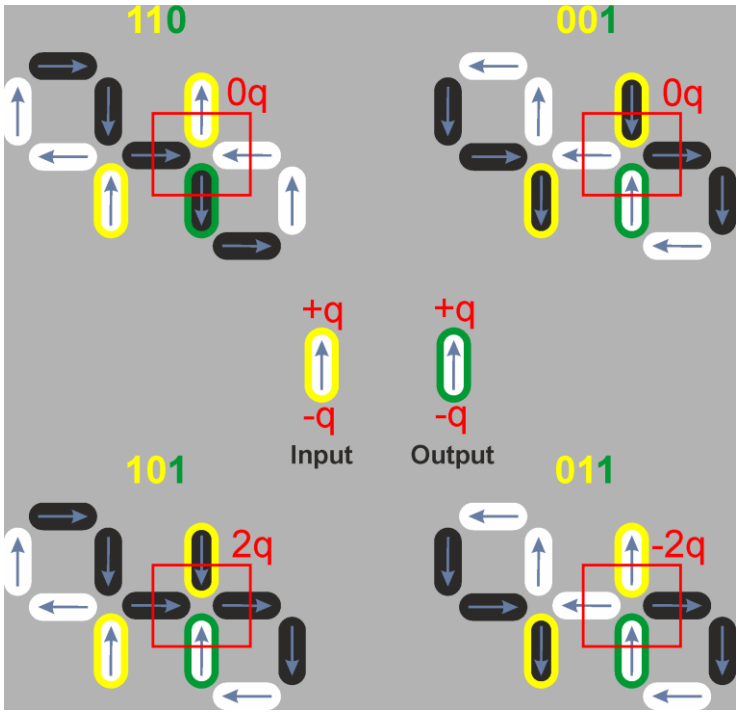

Figure 5.3: A schematic of pseudo-NAND gate moment configurations for logic operations of (110), (001), (101) and (011). For each gate operation, the net magnetic charge at the 4-vertex containing the output and enclosed in a red box is shown.

Even though gate operations involving inputs of (01) and (10) are unstable, we could still use the pseudo-NAND to demonstrate gate functionality by checking the success of accessing (110) and (001) logic operations. We have experimentally tested the efficacy of the pseudo-NAND gate in two experiments. The first involved a small sample set with a total of 48 logic gates and the experiments were performed in a similar way to the thermal relaxation described in the Transport of Information section (5.1) earlier, with the initial state of the nanomagnets set with the moments pointing along the direction of x-rays as shown in Figure 5.2b.

Two versions of the logic gates (Figure 5.5a) were built in order to test the two low energy logic operations involving (110) and (001). One version of the logic gate, with 24 gates in total, has inputs made of nanomagnets with a larger magnetic volume (L = 1000 nm and W = 200 nm), which ensures that the magnetization in the input nanomagnets retains its orientation throughout the thermal protocol (Figure 5.5). A second version of the gates was also made, with 24 gates in total, in which inputs had the same dimensions as the rest of the nanomagnets, which would then perform either a (110) or a (001) gate operation.

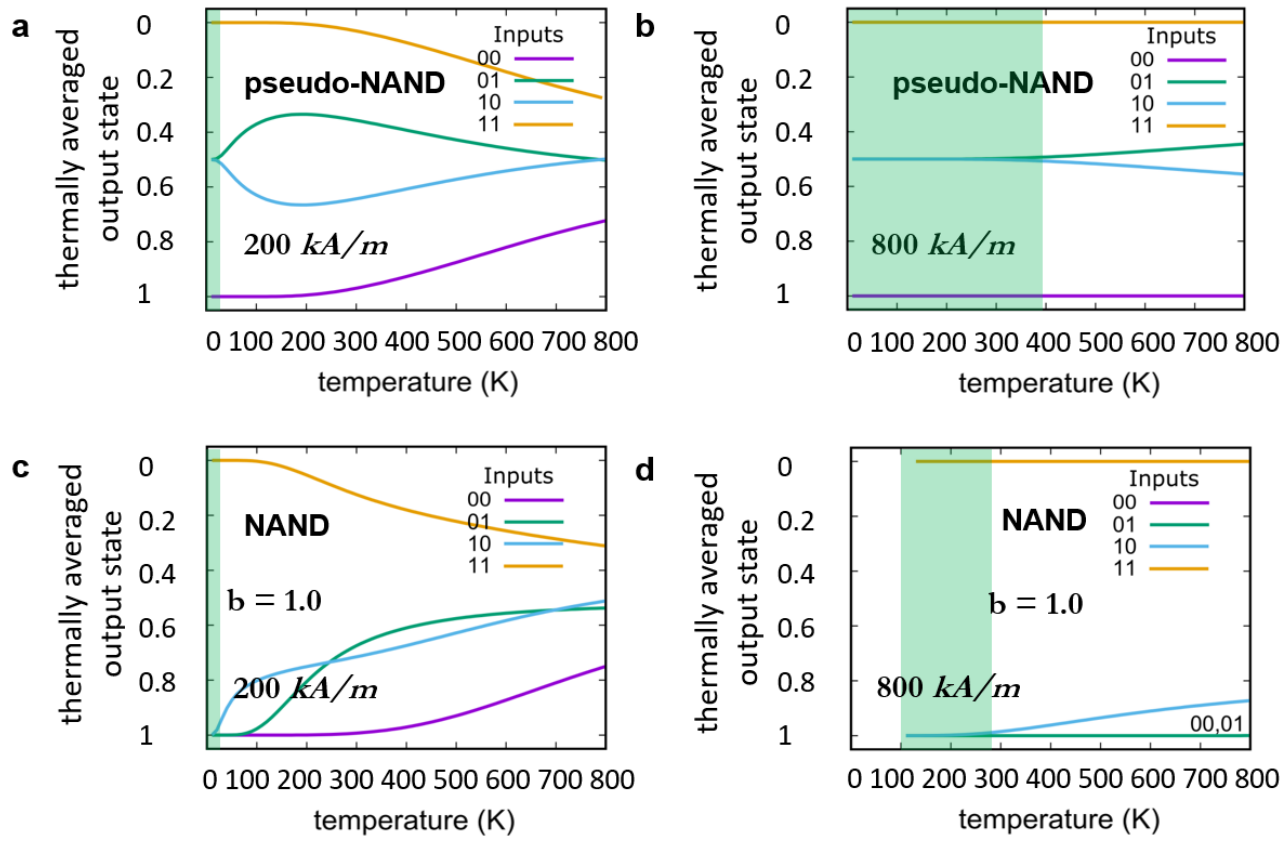

Figure 5.4: (a-b) Thermal average calculations performed on the pseudo-NAND gate for gate operations involving inputs of (00), (01), (10) and (11) and temperatures in the range 0 to 800 K. (c-d) Thermal average calculations for the NAND gate, where the bias nanomagnet has an M_s equal to all other nanomagnets in the logic gate, for inputs of (00), (01), (10) and (11) and temperatures in the range 0 to 800 K.

We observed that 46 out of the 48 logic gates performed the right logic operation, with one failure for each version. To statistically validate, we tested an additional 2310 individual logic gates (Figure 5.6) with shorter inputs, in an optimal thickness window of the nanomagnets (from ~2.0 to ~4.5 nm), resulting in either the state (110) or (001) with a success of ~94%. In addition, we have seen large regions on the sample where we observed 100% reliability for accessible operations of (110) and (001).

The experimental success of the pseudo-NAND demonstrated to us that the energetics of the logic operations played a key role in stabilizing the logic gates and that this design would an excellent candidate to build NAND gate with a few modifications. In order to morph the pseudo-NAND gate into a functionally complete NAND gate, a mechanism needed to be added that would turn the vertex containing the second input and the output (highlighted with red frames in Figure 5.3, more energetically stable. This problem was solved through the introduction of a “bias” nanomagnet, which

would form a 3-vertex, with 3 nanomagnets arranged at a common vertex, with the output nanomagnet as shown in Figure 30. The bias nanomagnet would then always have its moment orientation in one direction. For a NAND gate, the moment would be fixed in the “down” direction (Figure 5.7. If the moment were to be fixed in the “up” direction, then the logic gate would function as a NOR gate. The influence of the bias is shown in the dipolar-energy calculations, which indicate correct gate operations (NAND gate) with clearly defined ground state energies (Figure 5.4b).

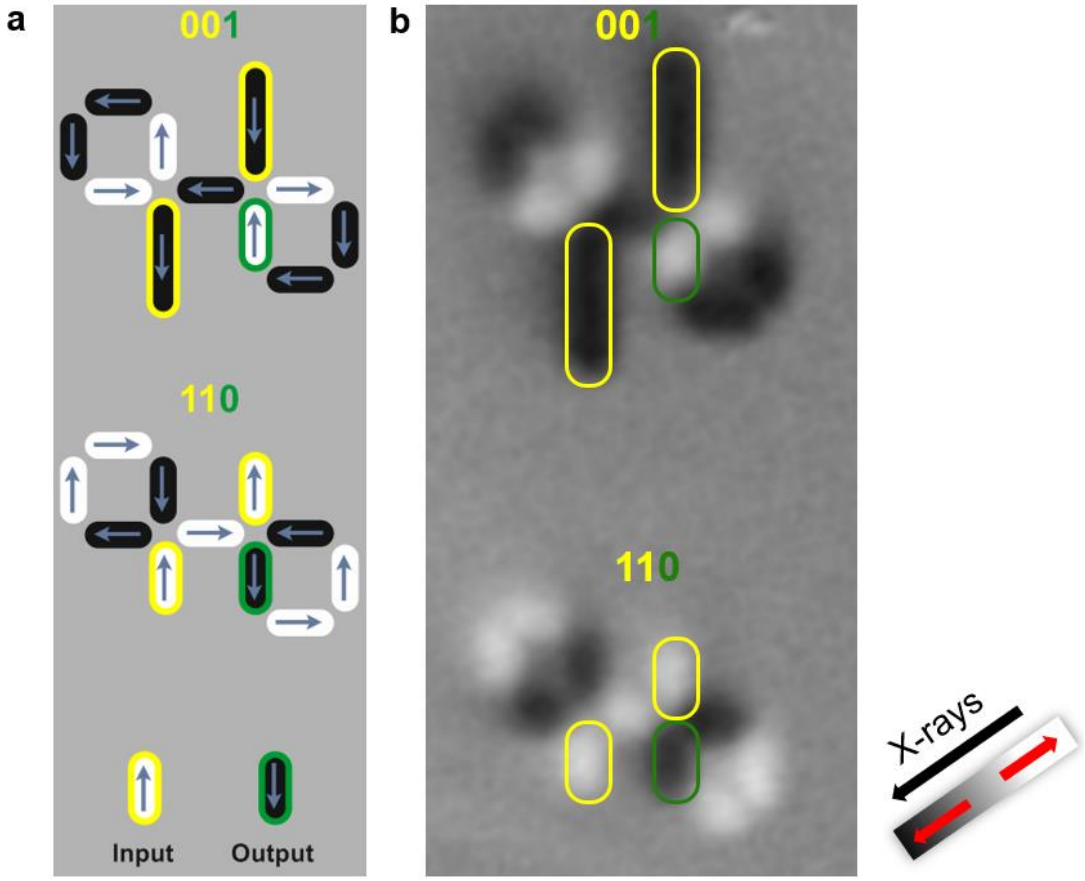

Figure 5.5: Schematic and X-PEEM images of a pseudo-NAND gate, which is thermally relaxed to give a gate operation of (001) and (110), corresponding to pinned inputs (00) and compared to a probabilistic input (11).

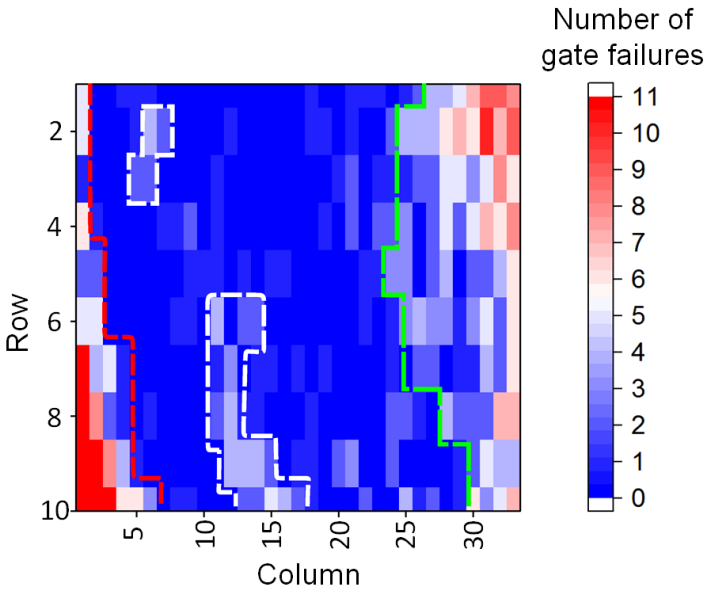

Figure 5.6: Map of logic gate failures. Logic gates are in a grid pattern where column values correspond to (approximately) varying thickness. Each "pixel" in the plot corresponds to 11 logic gates and is color coded based on the total number of logic gate failures. Higher (lower) values of the columns are associated with thinner (thicker) regions. The variation in logic gate failures is linked to the variation in thickness of logic gates across the sample. The optimal operation of the gates is found in a thickness window between ~2.2 nm and ~4.5 nm. Thicker regions with frozen moments are to the left of the red dashed line and thinner regions with fluctuating moments are to the right of the green dashed line. There are regions shown with a white dashed frame within the operational window where we observed increased errors, which are likely to be related to defects arising during sample fabrication.

Thermal average calculations support the NAND design and its efficacy. However, it was observed in the thermal average calculations that the logic operation of (101) was not fully stable at the room temperature. The gate operation of (101) was calculated to have a failure probability of (1×10^{-2}) for an M_S = 800 kA/m (Figure 5.8a and b), which is much higher when compared to a traditional CMOS. The solution to improving the failure probability of the (101) operation and in turn all the NAND operations was to optimize the value of the bias magnetization. Specifically, it was calculated that magnetization of the bias should be 0.75 times lower than the rest of the nanomagnets in the NAND gate, to obtain a failure probability of ~1×10^{-5}, which is more acceptable for device applications.

Implementation of the NAND design into devices is possible after overcoming several fabrication related challenges that were not addressed in this thesis. Even though the individual control of each input in a logic gate is possible and has been demonstrated previously[65, 66], the precise control of the bias to have a certain M_s and moment orientation while the logic gate undergoes energy

relaxation to perform computation is unclear. One possible solution would be to utilize exchange bias to pin the magnet's moment while thermal or field relaxation [4] is performed.

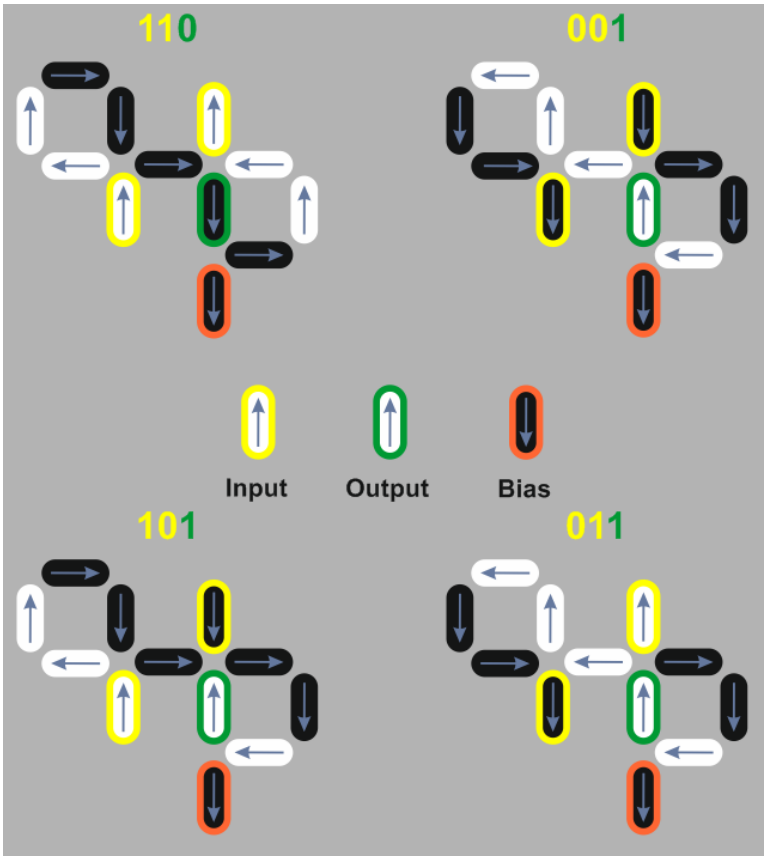

Figure 5.7: A schematic of NAND gate moment configurations for logic operations of (110), (001), (101) and (001).

With the introduction of this proof-of-concept NAND design, we have for the first time used ideas from artificial spin ice to construct a logic gate that reliably performs Boolean operations. While it was shown that the prototype NAND gate is operational, a key question concerning the transport of information from one logic gate to other remains. In particular, a design mechanism to connect the logic gates is required to construct any kind of complex circuitry.

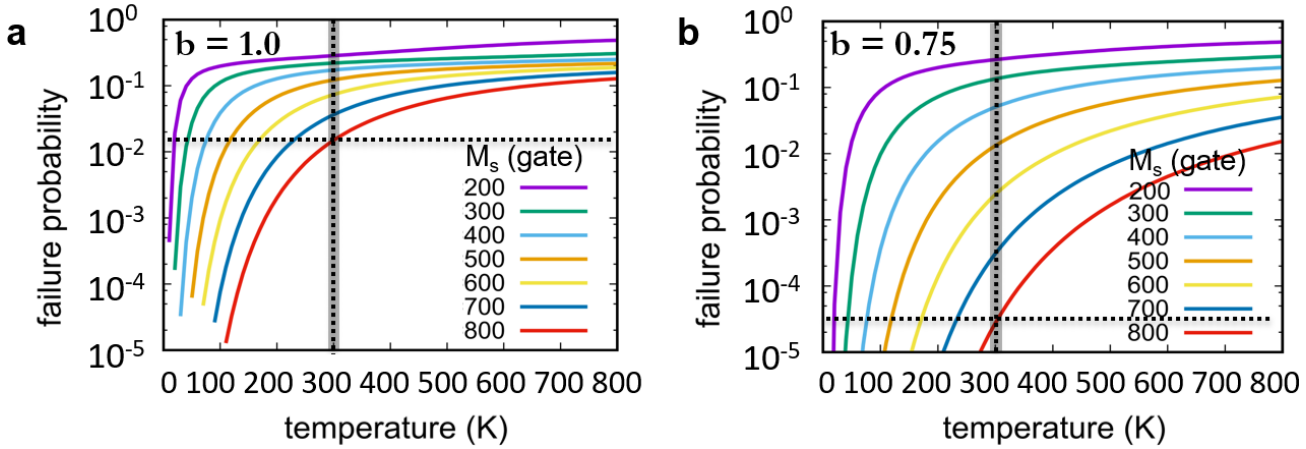

Figure 5.8: Calculated failure probability for the NAND gate for temperatures in the range 0 to 800 K, where the M_s values are varied from 200 kA/m to 800 kA/m in steps of 100 kA/m. Failure probabilities were calculated for gates containing a bias nanomagnet with (a) an M_s same as the nanomagnets comprising rest of the gates and (b) an M_s 0.75 times lower than the M_s of the nanomagnets in the rest of the logic gate.

5.3 Complex Circuits

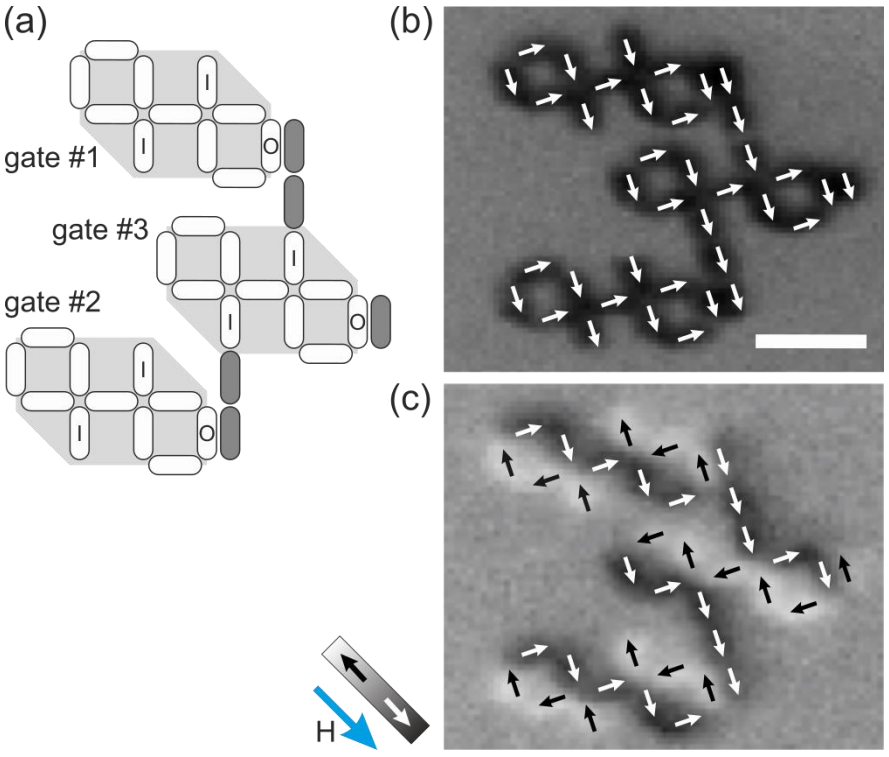

Figure 5.9: (a) A complex circuit comprising of two pseudo-NAND gates with their outputs connected to the input of a third pseudo-NAND gate. (b) The circuit starts with an initial state set

by an applied external field and (c) upon thermal relaxation leads to an output in the third logic gate that is directly correlated with the output of the two logic gates to which it is connected.

Here, I will present one possibility to connect logic gates together so that a complex circuit may be constructed. Such a realization of connected logic gates is critical to perform complex operations such as that of an adder circuit, without which modern CPUs cannot function. The pseudo-NAND gate is used to demonstrate a proof-of-concept circuit in which the outputs from two pseudo-NAND gates are utilized as inputs of the third pseudo-NAND gate, and a schematic of the connected gate is shown in Figure 5.9a. Shown in Figures 5.9b and 5.9c are the X-PEEM images of the experimentally tested circuit, where an initial state (Figure 5.9b) was set using an externally applied field and then thermally allowed to relax to a final low energy state (Figure 5.9c).

Similar connection schemes could be developed to build advanced circuits such as a half adder for use in complex computation. It should be noted that, the relaxation of logic gates are not necessarily sequential and therefore there is no flow of information in the circuit. This problem can be tackled in the future by addressing each logic gate at a particular time by implementing local clocking mechanisms such as the application of Oersted field in a current carrying wire.

Acknowledgements: I performed the sample fabrication and SEM measurements. X-PEEM measurements were performed by me with assistance from Jizhai Cui of Mesoscopic Systems, and Jaianth Vijayakumar of the Swiss Light Source. Thermal average calculations were performed by Peter Derlet from Condensed Matter Theory (CMT) at PSI.

CHAPTER 6: PROBABILISTIC COMPUTATION WITH ARTIFICIAL SPIN ICE

Earlier, in the introduction part of this thesis, I have defined a series of questions for each of the three sub-topics that my thesis would deal with. The following are the questions posed for the topic of probabilistic computation using artificial spin ice:

Can we create computational building blocks using ideas from artificial spin ice to generate a weighted/probabilistic output, which could then be used in applications such as artificial neural networks?

In this chapter, I will generalize the concepts developed in the earlier chapter to show that the probability of obtaining a particular output state can be altered by implementing high energy barriers in the relaxation pathway of logic gates. Such a relaxation pathway is described as a series of moment re-orientations, required in an array of nanomagnets, to relax from an initial field-set state to that of a final low energy state. The control of the output has the potential for use in probabilistic form of computation, such as artificial neural networks. Engineering these relaxation pathways to produce a broad spectrum of low energy outcomes, with varying degree of probability, is essential towards the creation of probabilistic computation. Such a control of the output is achieved by taking two different routes in the design of logic gates: (1) by designing a logic gate with a relaxation pathway that favors a probabilistic output and (2) by gradually modifying a relaxation pathway to yield outputs of varying probability. I will show experimental realizations of each concept, and furthermore demonstrate strategies to modulate the final outcome during computation. Such flexibility in modulating magnetic information, or *magneto-informatics*, may provide additional avenues to explore computation using nanomagnets.

6.1 Monotonic and Intermittent Relaxation Pathways

Similar to the previous chapter, here I consider elongated nanomagnets, with high shape anisotropy, where the magnetic moment points in one of two directions parallel to the magnet long axis. In order for a single nanomagnet to change its magnetic moment orientation, it requires energy of E_b, which corresponds to its intrinsic anisotropic energy. The energy required to facilitate moment reorientation is usually achieved by applying an external magnetic field or by heating the nanomagnet. The size of the applied energy (field or thermal) is correlated to the magnetic volume in each nanomagnet and thus the dimensions of the nanomagnet need to be fine-tuned to achieve relaxation. The dynamics of moment reorientations are assumed to follow Neel-type relaxation and thus their probabilities are approximated by the Boltzmann factor $e^{-\frac{E_T}{kT}}$ where E_T is the barrier energy associated with the transition between an initial state and a transition state (see Equation 2.13) and kT is the

energy at a given temperature T. It should be noted that E_T is E_b in the case of a single nanomagnet but, could include other energy terms such as dipolar strength when considering arrays of dipolar coupled nanomagnets.

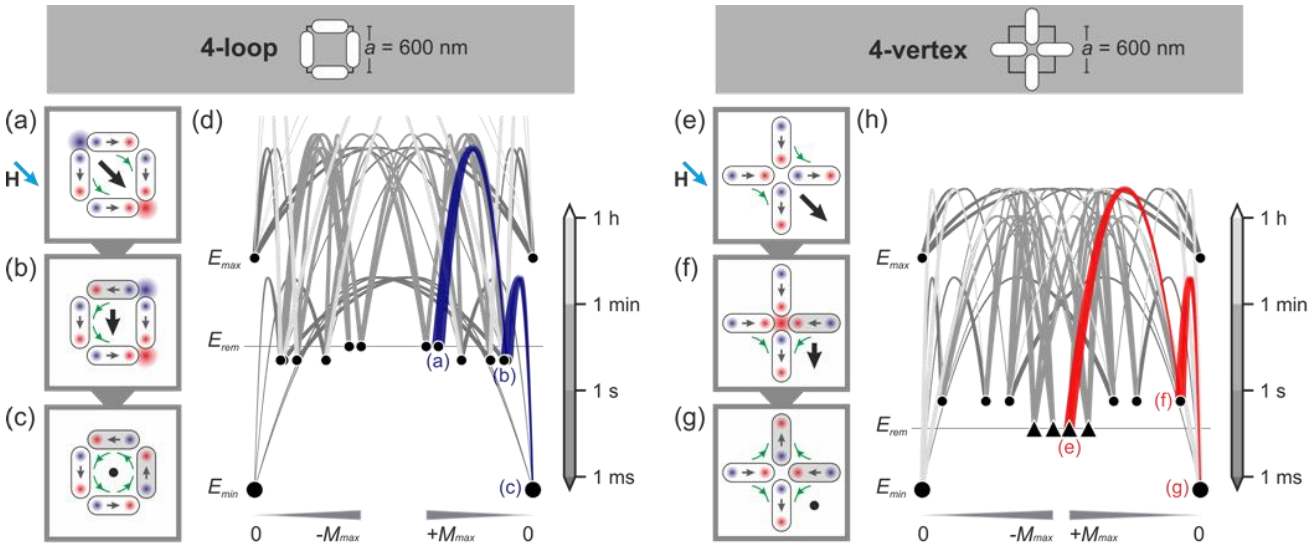

Figure 6.1: The single-spin-flip relaxation from a field-set state to the low-energy/ground state of a nanomagnetic configuration is determined by the corresponding state network diagram. (a-c) a schematic of a relaxation pathway in a 4-loop structure initialized by a global field, where (a) is the initial state, (b) is one of the many possible intermediate states and (c) is a low energy ground state. (d) The corresponding state network diagram of a 4-loop structure where all possible paths to low-energy states are illustrated. In blue is the pathway for the 4-loop structure as shown in (a-c). (e-f) a schematic of a relaxation pathway in a 4-vertex arrangement where (e) corresponds to an initial field-set state, (f) is a higher energy intermediate state and (g) is the final low energy ground state. (h) the state network diagram of a 4-vertex structure with the relaxation pathway in (e-f) highlighted in red. Ground states are shown using large black dots, while low energy metastable states are shown using black solid triangles.

We start with all the nanomagnets in a particular configuration (Figure 6.1a and Figure 6.1e) that have an initial state set by an external magnetic field, where all the magnetic moments are aligned in the direction of the applied field. Such an initial state corresponds to an intermediate energy, as opposed to a ground state that possesses the lowest energy, or the highest energy state where the total number of magnetic charges are maximized. Upon removal of external field and the application of heat, the individual nanomagnets will undergo thermally induced moment reorientations and the structure will thermally relax to a ground state [Figure 6.1c and Figure 6.1g][22, 67]. In arrays of nanomagnets, moment reorientations are not only dictated by the intrinsic energy barrier (E_b) but also the energy associated with the dipolar coupling between different nanomagnets (E_d). Thus the energy

barrier to switching (E_T) is approximated by $E_T=E_b+ E_d$[67, 68]. It is assumed that all the nanomagnets in the array are identical and therefore E_b is the same for all of them. The transition rate between different states is described by:

$$\nu(E_T, T) = \nu_0 e^{-\frac{E_T}{kT}} \quad (6.1)$$

Here, ν_0 is the attempt frequency and is set at $10^9 s^{-1}$, k is the Boltzmann constant, and E_T is the transition energy. The temperature is set to 400 K for the rates obtained in Figure 6.1. The barrier energy is approximated by equation 2.13. Here, E_b is the single particle switching barrier and is set at 0.626 eV for Permalloy, *m* and *l* are the initial and the transition state with dipolar energies of E_m and E_l.

The collective reversal of moments, corresponding to different energies, from an initial set state to that of a final low energy state is thus a relaxation path, and the probability of traversing the different energy levels in a relaxation path is governed by the Boltzmann factor.

Different spatial arrangements of nanomagnets possess different relaxation paths, corresponding to different transition states. These transitions could be from an initial low energy state (E_i) to that of a lower energy state (E_{i+1}), which is termed as Monotonic relaxation path (M-type) or from an initial low energy state (E_i) to that of a lower energy state via a higher energy state (E_{i+1}), which is an intermittent relaxation path (I-type). Thus, all relaxation paths are either M-type or I-type. From a computational standpoint, an M-type relaxation path would lead to a deterministic output. On the other hand, an I-type relaxation path incorporates a weight in it, where the output relaxed state is determined by the height of the energy barrier, and thus leads to a weighted output.

This is illustrated in Figure 6.1 by the relaxation behavior from a field-set configuration to the ground state in two basic motifs derived from artificial square ice[67]. Here, I will introduce the idea of state network diagrams, which visually describes the energy states associated with different orientations of magnetic moments in an array of nanomagnets. Examples of state network diagrams are shown in Figures 6.1d and 6.1h. The 4-sided polygon (or a 4-loop structure) (Fig. 6.1a) and the 4-vertex (Fig. 6.1e) structures contain four nanomagnets each, arranged on the edges of a square lattice. In both cases, the initial state is set by an external magnetic field. Upon the removal of the external field, the individual nanomagnets will undergo thermally-induced moment reorientations, letting the system relax to a state of lower magnetostatic energy[50].

It should be noted that, throughout the thesis, relaxation pathways have been described in the context of dipolar energies for particular magnetic configurations. However, transition rates are also influenced by any change in the single particle switching barrier in the nanomagnets. Often a change in single particle switching barrier E_b would be higher in energy that the difference in dipolar energies

between transitions. Therefore, systems in which the shape or the composition of the nanomagnet are altered may not exactly follow the relaxation pathways described here. Additionally, such a change in E_b is often implemented in arrays of nanomagnets to alter the relaxation probabilities to attain particular states[69]. However, there are fabrication challenges to tuning E_b, since the single particle switching barrier is an intrinsic property and therefore individual nanomagnets need to be altered such that their shape or composition is different to rest of the nanomagnets in an array. In an earlier work, attempt frequency, in turn the transition rate, in iron nanomagnets were found to be strongly dependent on the shape and size of each nanomagnet[70]. Therefore, there is a concern that fabrication related defects, such as a small change in the shape of each nanomagnet may lead to a changed E_b. However, experimentally we have not observed lithographic defects to have had a significant role in changing a relaxation pathway. Therefore, it is reasonable to assume that lithographically fabricated arrays of nanomagnets, such as those described in this thesis, with a small disorder in shape or spin would still have a similar E_b. Thus, the model used to describe relaxation pathways in this thesis, in which only the dipolar energies are considered, should be sufficient. Finally, within the assumption of a constant E_b, the transition probabilities between different states are expected to be solely driven by the energy differences between magnetic states.

Two kinds of relaxation pathways, as introduced earlier, in the nanomagnetic state networks can be formally distinguished:

Monotonic relaxation (M-type) paths in *n*-loops: The two lowest-energy configurations of a closed 4-loop (and, in general, any *n*-loop with $n>1$) are characterized by a left- or right-handed flux closure state (Fig. 32c), respectively. In contrast, the remnant state S_0, shown in Fig. 6.1a, as well as any state of higher energy, features one pair (or several pairs) of magnetic charges $\pm 2q$. Therefore, the relaxation towards the ground state G_i progresses via the annihilation of magnetic charges (as well as the reduction of net magnetization) and the successive reduction of the magnetostatic energy, which can be written as:

Monotonic relaxation path via the states: $0 \rightarrow 1 \rightarrow \ldots \rightarrow k$, where $E_i > E_{i+1}$ for all I, and k corresponds to a final low energy state.

The presence of Monotonic relaxation pathways in a state network, leads to a deterministic relaxation as desired in the design of Boolean logic gates.

Intermittent relaxation (I-type) paths in *2n*-vertices: The two ground states of a 4-vertex structure (any 2*n*-vertex structure with $n>1$), one of which is shown in Fig. 32g, is determined by maximizing the number of pairwise head-to-tail configurations. Likewise, the remnant state (Fig. 6.1e) is characterized by a vanishing magnetostatic charge at the vertex. However, a single-spin flip leads to the creation of vertex charge ±2q, leading to an intermediate state with higher magnetostatic energy

(Fig. 6.1f). Therefore, the successive transitions involve an increase in dipolar energy (Fig. 6.1h), which can be written as:

Intermittent relaxation pathway via states: $0 \rightarrow 1 \rightarrow \ldots \rightarrow k$, where $E_i < E_{i+1}$ for at least one i.

Furthermore, the presence of metastable states in the state network, where any relaxation pathway includes a transition to a higher-energy state (marked by triangles in Figure 6.1h), can potentially trap the system in a non-ground state configuration (if thermal energy is too low to overcome the barrier), or can lead to relaxation into other pathways (if the barrier can be overcome by thermal fluctuations).

Either way, the presence of intermittent pathways in a state network leads to a probabilistic relaxation. With respect to Boolean logic operations, such behavior is undesirable. However, the probability of output states, and the possibility to modulate the output by varying the intrinsic barriers of the network by the design of the spatial nanomagnet configuration, makes such systems interesting for probabilistic computational applications.

It should be noted that traditional nanomagnetic logic does not consider the presence of I-type paths (or any relaxation path) in their designs.

6.2 Conditions for I-type Relaxation Pathway in Composite Structures

As shown earlier, the creation of magnetic charges at vertices is intimately tied to the presence of intermittent relaxation paths. However, this behavior might change for vertices combined with other motifs, i.e. loops or vertices, as the magnetostatic energy associated with a charged vertex might be compensated by a gain in interaction energy due to flux closure configurations in other parts of the nanomagnetic structure.

In the following, I propose conditions for an arbitrary spatial arrangement of *n* nanomagnets that will feature intermitted relaxation paths, i.e. involving transitions via a higher-energy state. The fundamental idea behind the generalization of rules is shown in Fig. 6.2, where moment configurations in a 4-vertex structure are described as part of a combinatorial approach using a binomial expansion. It is important to point out that in order to observe relaxation via an intermittent path, all 2*n*-vertex structures are in an initial configuration with a 0q charge. This can be achieved, for example, by applying a global magnetic field.

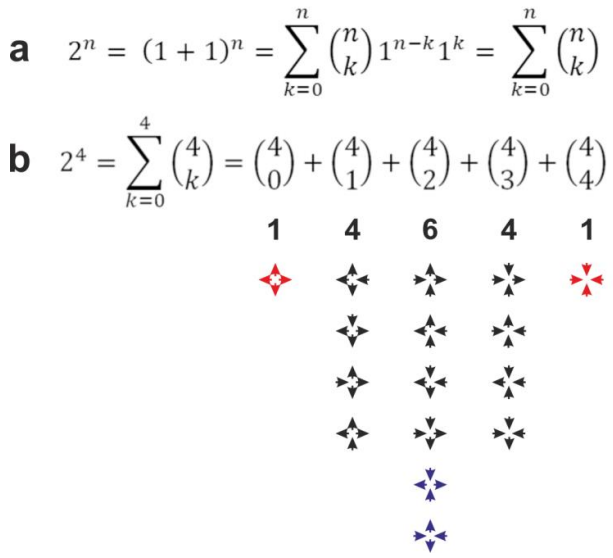

Figure 6.2: (a) For 2n-vertices the number of states with zero magnetic charge can be deduced by simple combinatorics using Binominal coefficients. (b) All states for a 4-vertex structure, classified by the number of k moments pointing into the center of the vertex. Uncharged configurations are those with an equal number of moments pointing inwards and outwards, i.e. C(2n, n) = C(4, 2) = 6. Of these six states, two are the ground states (in blue), whereas the others correspond to the field-saturated states, one of which is considered as initial state in Fig. 6.1e.

Condition 1

n-loop structure*: An n-sided polygon has a high-energy state containing ±2q magnetic charge, which transitions to a 0q low-energy state (i.e. the flux-closure ground states). There is no intermediate state which is higher in energy than the initial (saturated) state. Therefore, an n-sided polygon always features Monotonic relaxation paths.*

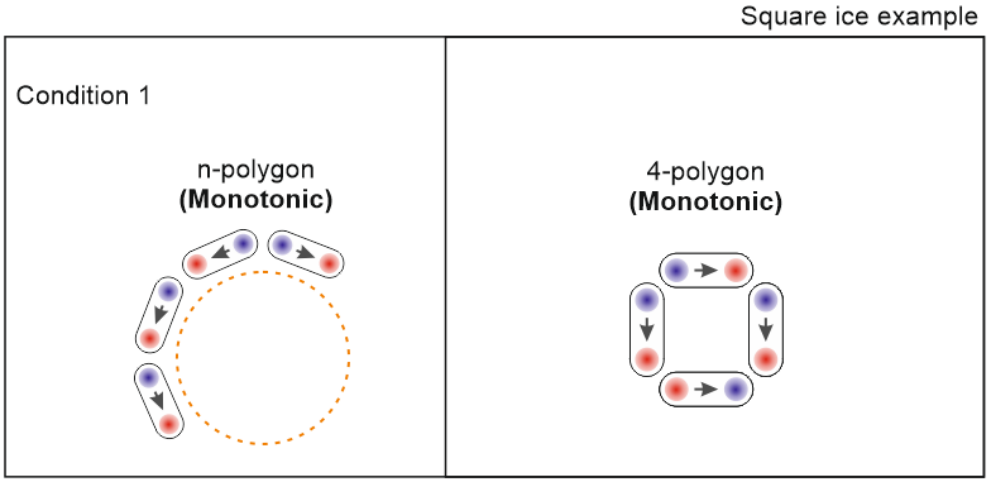

Figure 6.3: A schematic illustrating Condition 1 with a square ice example.

Condition 2

***2n-vertex structure**: There are $C(2n,n)$ states for a 2n-vertex structure where the total magnetic charge at a vertex is 0q (Fig. 33b). Here we assume that the only way the net charge at a vertex is zero is if there are n magnetic moments with a +q magnetic charge and n magnetic moments with a –q magnetic charge, totaling 0q. There are two possible ground states in any 2n-vertex structure. Therefore, there are a total of $C(2n,n)-2$ possible states with intermediate energy and a 0q charge. Relaxation from any of these zero-charge states to the zero-charge ground state would require the creation of an intermediate state of excess magnetic charge. Thus a 2n-vertex features intermittent relaxation paths if the initial state corresponds to one of the 0q states.*

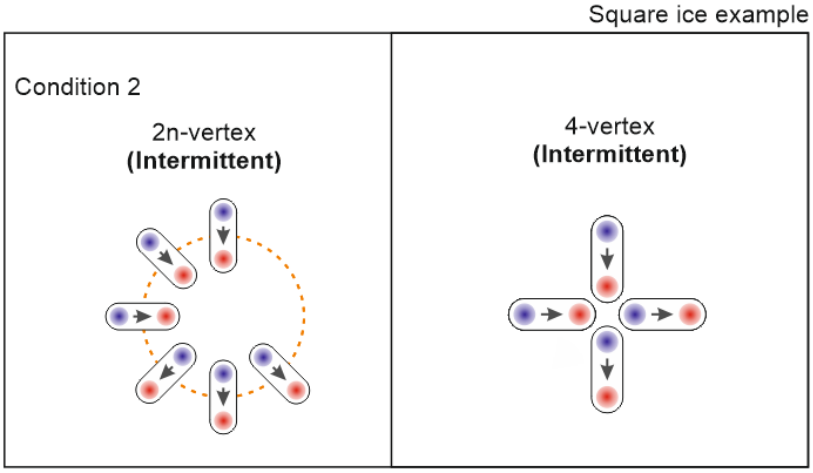

Figure 6.4: A schematic illustrating Condition 2 with a square ice example.

Condition 3a

***n-loop structure+2n-vertex structure (Figure 6.5)**: This is an extension of the considerations of a 2n-vertex structure (condition 2). The existence of one shared nanomagnet between an n-sided polygon and a 2n-vertex structure does not alter the energetics for the relaxation of the 2n-vertex structure; there still are $C\left(n,\frac{n}{2}\right)-2$ possible initial states with a 0q charge.*

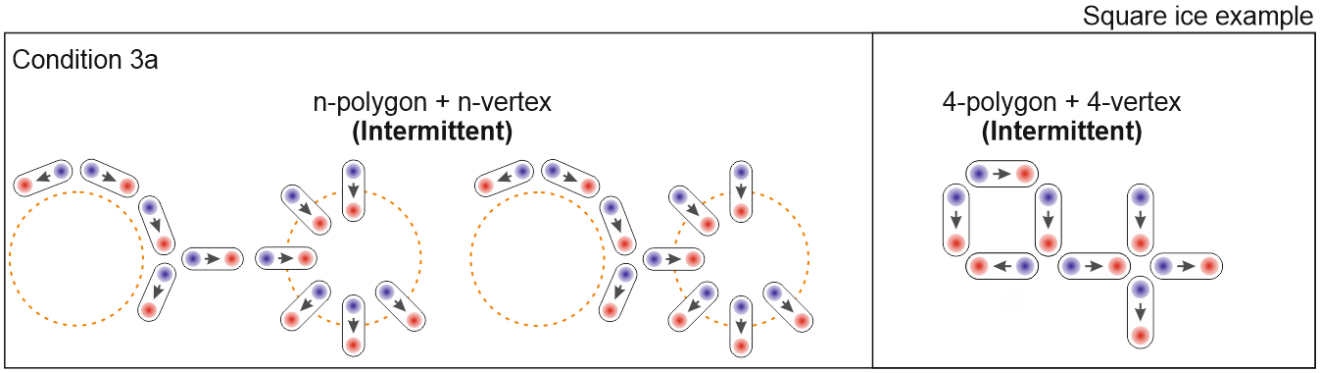

Figure 6.5: A schematic illustrating Condition 3a with a square ice example.

Condition 3b

n-vertex structure + 2n-vertex structure (Figure 6.6)*: This is an extension of the considerations of a 2n-vertex structure (condition 2). Here, the existence of one shared nanomagnet between two or more n-vertices – if at least one of them is even – is not enough to alter the fact that relaxation from a zero-charge state occurs via the creation of charged states of higher energy– there still are* $C\left(n,\frac{n}{2}\right)-2$ *possible initial states with a 0q charge.*

n-polygon structure + n-polygon structure (Figure 6.6): *This is an extension of the considerations of an n-polygon structure (condition 2). The combination of two polygons does not lead to the creation of excess charge above the background (assuming a field-set initial state) that may contribute to the creation of an I-type path. Therefore n-polygon structure + n-polygon structure is always M-type.*

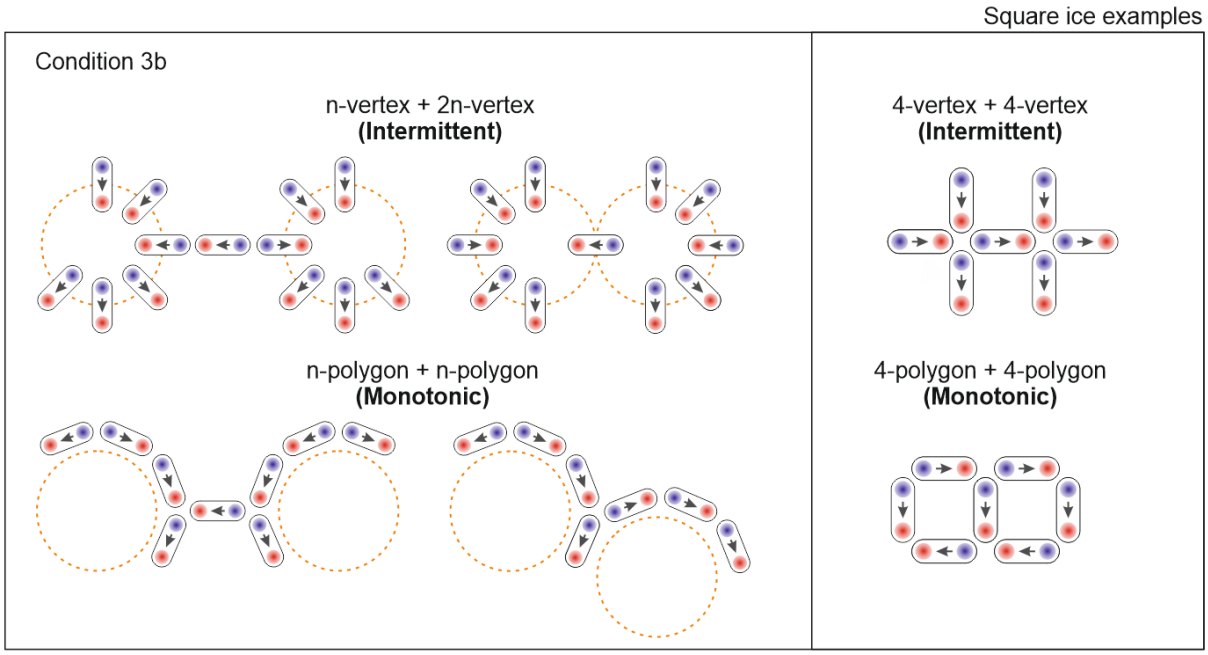

Figure 6.6: A schematic illustrating Condition 3b with a square ice example.

Condition 3c

n-loop structure incorporated in n-vertex structure (Figure 6.7)*: Unlike the previous two conditions (condition 3a and condition 3b), the incorporation of an n-vertex into a loop alters the properties of the 2n-vertex, and therefore Condition 2, under specific considerations. As I have noted before, there are* $C\left(n,\frac{n}{2}\right)-2$ *possible initial states with a 0q charge in a 2n-vertex. We know that for every two nanomagnets in a 2n-vertex, there is a possibility of incorporating one n-loop. Additionally, for every n-loop incorporated into a 2n-vertex, there is a path where the creation of excess charge in the 2n-vertex is offset by the lowering of energy in the n-loop. Thus, for this composite to feature intermittent relaxation paths via the creation of intermediate states with excessive charge, the number of*

nanomagnets not part of any polygon must be $> \frac{n}{2}$, *so that the condition of* $C\left(n, \frac{n}{2}\right) - 2$ *possible initial states with a 0q charge is still valid.*

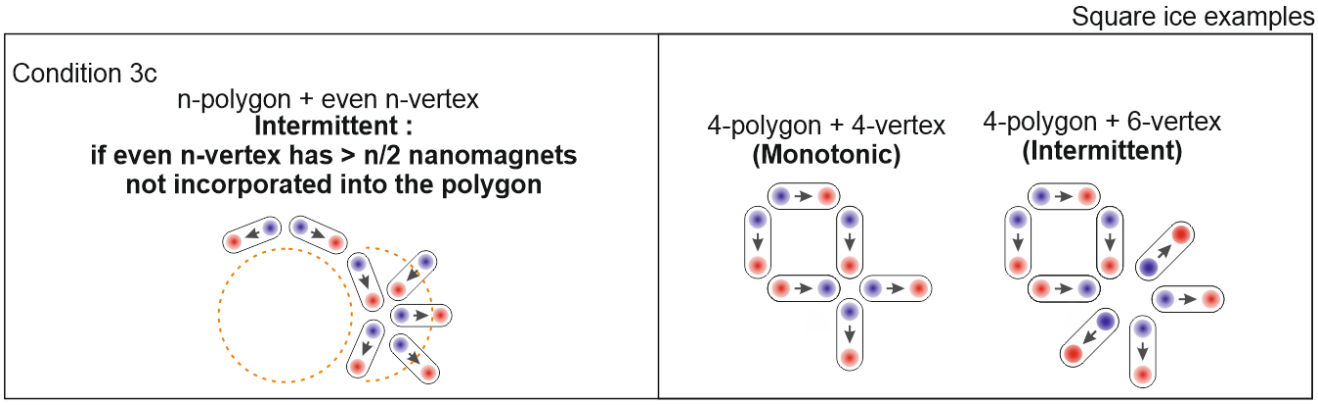

Figure 6.7: A schematic illustrating Condition 3c with a square ice example.

These three conditions thus dictate if a particular arrangement of nanomagnets is of the I-type or the M-type.

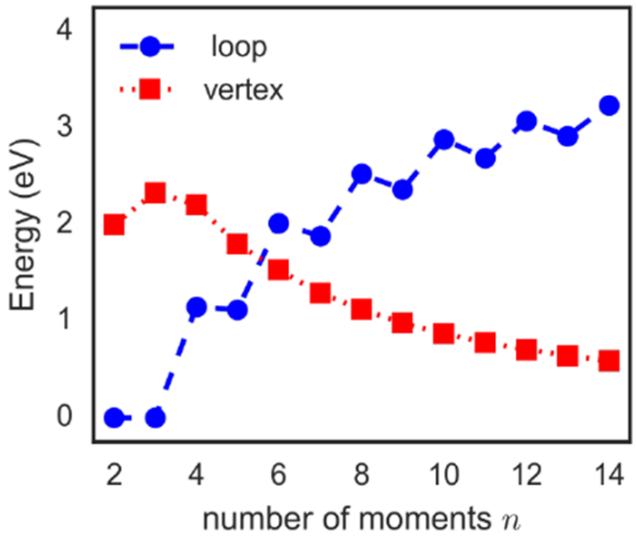

Figure 6.8: Calculated energies of n-loop and n-vertex structures, where the y-axis is the normalized energy ($[E_{max}$-$E_{sat}]/n$) and the x-axis corresponds to number of moments in the structures.

It should, however, be noted that the conditions may not hold if the total number of nanomagnets reaches a critical value of *n*. The magnetostatic energy of an n-loop would continue to rise with an increase in n, while that of an n-loop would continue to drop (Figure 6.8). Therefore at a critical *n*, the conditions described in this section would not hold anymore. The crossover observed in

Figure 6.8 does not necessarily tell us if the conditions described in this section would break down at a value of ~5 for *n*, but they give a hint as to when such a breakdown may occur. At the time of writing, the role of a critical *n* is under consideration and additional analysis involving Monte-Carlo and micromagnetic simulations are still being carried out and therefore not included in the thesis.

6.3 Probabilistic Relaxation in P-gate

First, I will discuss the behavior of the probabilistic gate or the P-gate, for which we expect an I-type relaxation pathway. A scanning electron microscopy (SEM) image of the P-gate design is shown in Fig. 6.9. From the 390 P-gates tested, we found that 48.5 % of the gates relaxed to the ground state G2 shown in Fig. 6.9c, whereas only 26.6 % of the gates ended up in the (degenerate) ground state G1 shown in Fig. 6.9d. In addition, several other states were observed, most notably the (metastable) state M shown in Fig. 6.9e, which accounted for 16 % of the final configurations.

The imbalance of the ground state population indicates that the transition barriers involved in reaching G2 must be higher than those on the paths towards G1. This is illustrated in Fig. 6.9f, which shows the state connectivity network diagram. Here, the highly probable relaxation paths towards G1 (in blue) and G2 (in red) are highlighted. From the saturated state S_0, either ground state can be reached by three successive spin flips. On the path towards G1 (in blue) the first transition is towards a state with higher dipolar energy, requiring overcoming a large activation barrier, already reducing the probability for the system to effectively relax towards G1.In contrast, the first spin flip towards G2 (red path) leads to a state of lower energy, which biases the system towards relaxation to G2. However, with this transition the system ends up in a “metastable” state (triangles), for which single-spin flips only allow for transitions to states with again higher dipolar energy due to the creation of charges or reduction of the local flux

The presence of a metastable state in the relaxation path has severe consequences for the final outcome probability in the logic gates: First, transitions towards other relaxation paths and even a relaxation back to the initial state are possible. This behavior was also observed in our experiment as the time evolution in Fig. 6.9g illustrates. The corresponding relaxation path is highlighted green in Fig. 6.9f. Second, metastable states can act as an energy trap for an undesirable/incorrect state, as the relatively high population of state M (in Fig. 6.9e) demonstrates.

A small bias field is present in the X-PEEM chamber and is taken into account in our analytical calculations, such as the Kinetic Monte Carlo .The size of the bias field is comparable to the earth’s magnetic field of ~40 - 80 μT and its presence has been confirmed in recent experiments[71].

The probability to reach each ground state can thus be finely tuned by sample design, temperature at which the thermal relaxation takes place, and biasing with a small magnetic field.

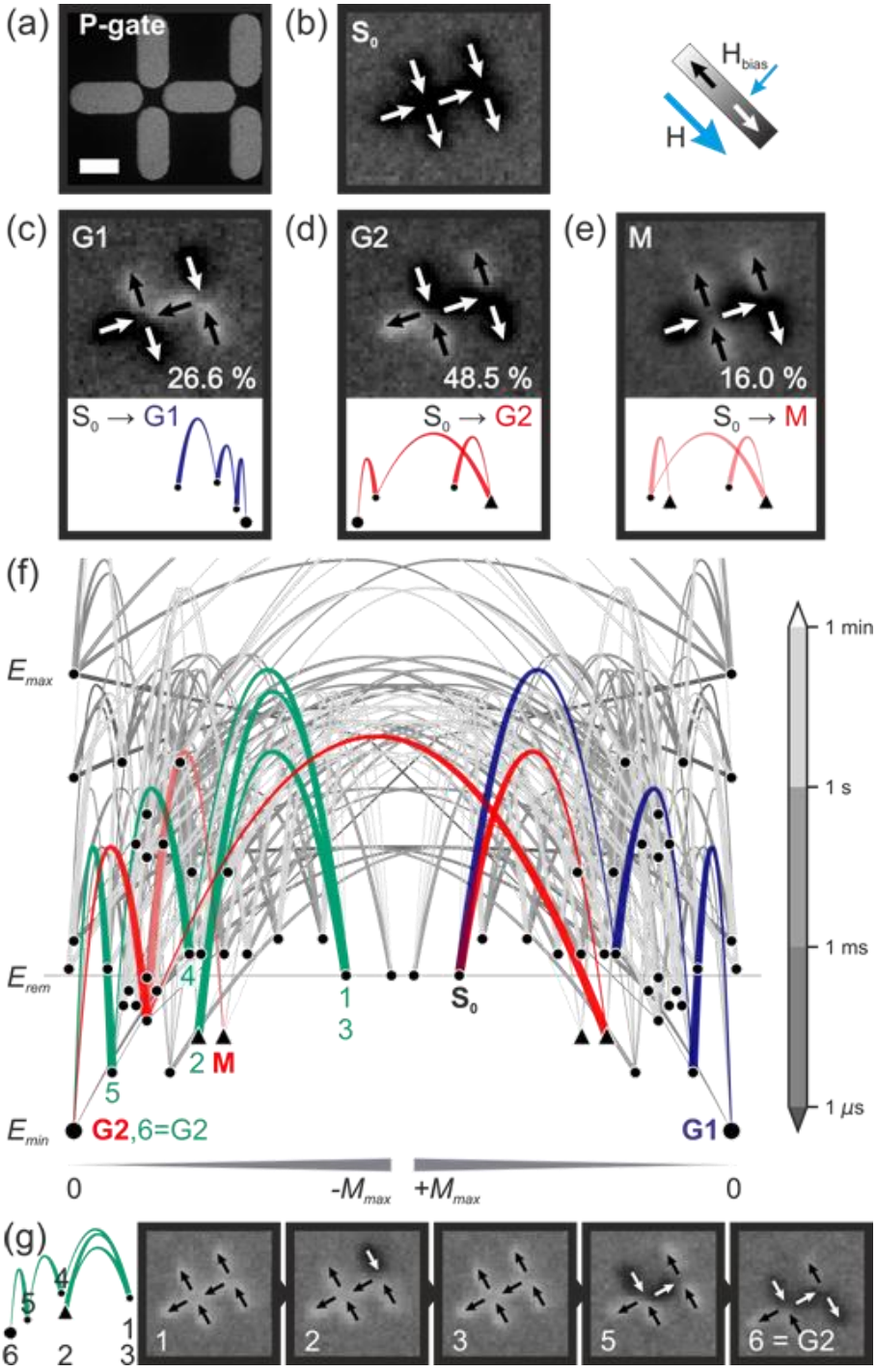

Figure 6.9: (a) Scanning-electron microscopy image of the P-gate. Scale bar measures 250 nm. (b) Saturated initial state and (c and d) the two degenerate ground states imaged by X-PEEM. For 390 gates we observe that the ground state (G1) shown in (d) is reached in 48.5 % of the gates, whereas the degenerate ground state (G1) in (c) is reached in only 26.6 % of the cases. In addition, the metastable state M shown in (e) has a final occupation of 16.0 %. (f) State network diagram of P-

gate at T = 400 K. The paths of S_0 to G1 and S_0 to G2 are highlighted in blue and red, respectively. In addition, the path in (g) is highlighted in green. (g) X-PEEM imaging of a P-gate where the relaxation path is reversed, from step 2 to step 3, during the course of a thermal relaxation. Step 4 is not shown due to an abrupt increase in the rate of relaxation and the X-PEEM not having the time resolution to cope with the sudden change.

6.4 Deterministic Relaxation in D-gate (pseudo-NAND)

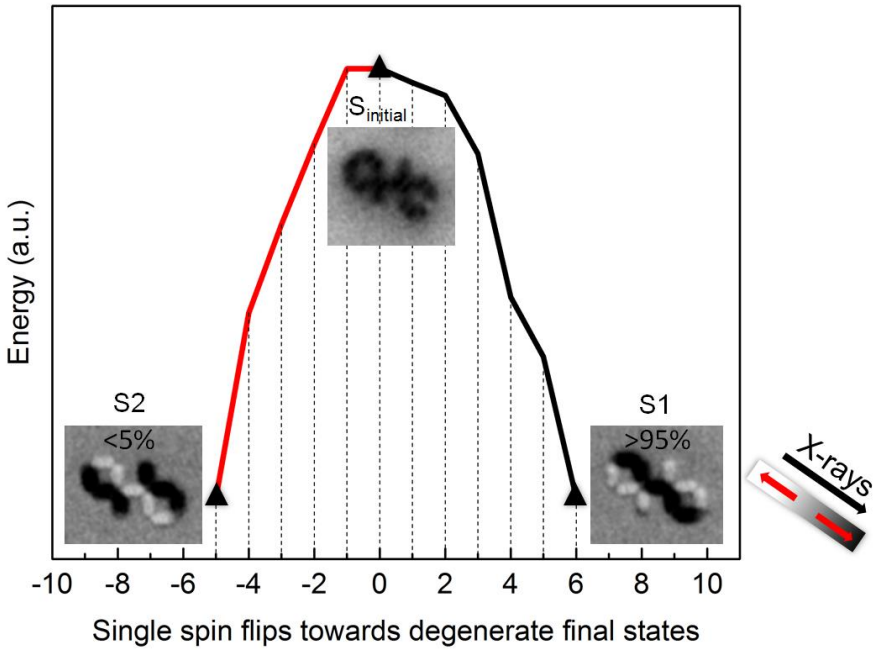

Figure 6.10: A one dimensional relaxation pathway for the D-gate is shown, where the operations of (110) and (001) are performed. The x-axis denotes the number of single spin flips required to reach one of the two degenerate states. The y-axis is the dipolar energy corresponding to each relaxation step. It should be noted that in a D-gate, the relaxation pathway does not incorporate any transitions to higher energy states and therefore makes for a highly reliable logic gate.

Now I will discuss the experimental realization of the deterministic gate or the D-gate, for which we expect, based on the design rules presented earlier, an M-type relaxation pathway. In the previous chapter[22], I demonstrated that the design shown in Fig. 6.10d acts as a pseudo-NAND gate with a failure probability of ~10^{-5} at room temperature. Here, I will discuss the peculiarities of the relaxation behavior that leads to this operational stability and will demonstrate a strategy to modulate the final outcome probability.

Testing 2310 D-gates, It was found that, starting from the saturated state S_0 shown in Fig. 6.10, thermal relaxation at elevated temperatures leads to a final probability of 91 % for the ground state S1, and only 3 % for the degenerate ground state S2 (Fig. 6.10). The fact that almost all gates end up in

the configuration's ground state indicates that thermally-assisted relaxation takes place via continuous pathways through the state network successively lowering the dipolar energy. This is in contrast to the previously-discussed P-gate, where a sizable fraction (51.5%) of P-gates ended up in intermediate and G1 states, as well as G2 states.

This deterministic relaxation in the D-gate stems from an energetic bias that results in the D-gate initially choosing a path from S_0 towards ground state S1. This bias is associated with the kinetics of the very first spin flip taking place during the relaxation process. The first barrier of the 5-flip fastest path towards S1 is slightly higher than the first transition on the 6-flip fastest path towards S2 (Figure 6.10). Even though this difference might appear small, the transition probability is determined by the Boltzmann factor $\sim e^{-\left(\frac{E_T}{k_B T}\right)}$, which leads to a pronounced preference to overcome the smallest possible barrier. Once the path towards either S1 or S2 is chosen, thermal relaxation proceeds without further hurdles.

The experimental results show that the D-gate exhibits deterministic relaxation with a high output probability for one of the two final states, as is desirable for Boolean-logic applications. However, for the use in non-Boolean computation, the output probability needs to be modified in a controlled manner.

6.5 Modulation of Output in D-gate (pseudo-NAND)

It is now clear that the strong bias of the D-gate to relax to ground state S1 stems from an initially small preference towards this path upon the systems very first spin flip. This indicates that even small changes of the transition barriers can affect the relaxation kinetics profoundly. As I will show in the following, such modifications to the state energies can be introduced locally in order to continuously modulate the final relaxation outcome. Here, we physically change the initial design of the D-gate by shifting one of the two 4-loops by a distance *d* away from the initial vertex center (Figure 6.11d), thus weakening the dipolar coupling at the vertex. In turn the activation barrier associated with the creation of a vertex charge decreases.

For each separation *d* between 0 nm and 80 nm, we tested the thermal relaxation behavior of 51 modified D-gates. The relaxation percentages to reach ground states G1 and G2 is dependent on the separation *d* and plotted as points in Figure 6.11e. G1 and G2 in Figure 6.11b and Figure 6.11c, is the same as S2 and S1 in Figure 6.10, the change in naming was done so that it is consistent with data from Section 6.3. We observe a clear decrease in percentage of states found in G1 with increasing *d*, and less of a variation for G2. This behavior agrees very well with theoretical predictions based on kinetic Monte-Carlo simulations, shown as solid lines in Figure 6.11e. For the kinetic Monte-Carlo simulations, the nanomagnet dimensions and the lattice parameter were exactly those used for the fabricated lithographic structures. In addition, the saturation magnetization was set to 350 kA/m and

the single particle switching barrier was assumed to be 0.626 eV. An external bias of 50 μT was applied to the simulated structure, as this magnetic field was found to be present in the experimental XPEEM chamber. This demonstrates the possibility to create and control the output in nanomagnetic logic gates, as required for non-Boolean operation.

Even though we modulated the output probabilities by physically varying the gate design, similar local variations can be achieved in-situ, for example by Oersted fields in a current-carrying nanowire[72], exploiting strain-mediated effects[73] and interaction modifiers[74]. Such designs would even allow adjustment of the transition barriers during the course of a computation cycle.

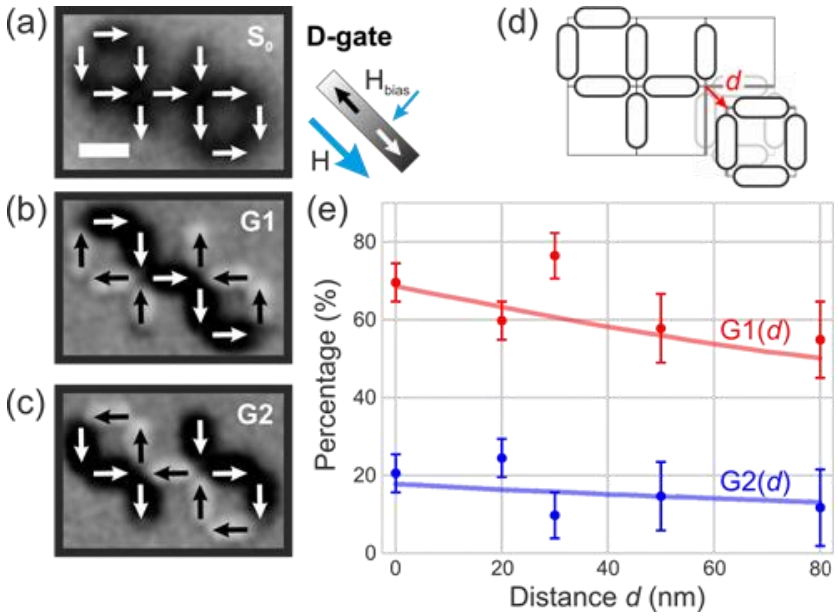

Figure 6.11: Modulation of output in a D-gate with an initial state (a) set by an external field with (b) and (c) showing the degenerate states G1 and G2. (d) Output modulation is achieved by physically moving one of the 4-loop structures away from the structure, thus weakening the dipolar coupling between the 4-loop and rest of the logic gate. (a) A plot of the experimentally observed percentages of G1 and G2 in the D-gate for distances of 0, 20, 30, 50 and 80 nm are shown using solid dots. Also plotted are the KMC simulations shown using solid lines.

Acknowledgements: Sample fabrication and SEM were performed by me. X-PEEM measurements were performed by me with assistance from Jizhai Cui of Mesoscopic Systems, and Jaianth Vijayakumar of the Swiss Light Source. KMC calculations were performed by Dominik Schildknecht from the Condensed Matter Theory (CMT) group at PSI. State network diagrams were plotted by Naemi Leo of CIC NanoGUNE.

CHAPTER 7: DETERMINISTIC INJECTION OF MONOPOLE CURRENTS IN ARTIFICIAL SPIN ICE

As has been the case with the previous chapters, this chapter will begin with one of the key questions posed at the beginning of the thesis. The question being:

… is it possible to control the generation and evolution of monopole currents in artificial spin ice? If yes, can we implement them as part of a device?

In this chapter, I will lay down some of the ideas behind nucleating (or injecting) monopoles at a location of my choosing and controlling the direction of the generated monopole currents. Emergent magnetic monopoles were described in the earlier chapters as moment configurations at a vertex where there is an excess magnetic charge. In extended arrays of artificial spin ice, monopoles always occur in pairs of opposite charges, with the monopole-antimonopole pair connected by a series of nanomagnets with a head-to-tail (or tail-to-head) moment orientations. These nanomagnets connecting two oppositely charged monopoles are referred to as Dirac strings[15] and their dynamics are considered as monopole currents[75, 76]. Here, I will use different vertex configurations, exploiting their energies, to produce deterministic injection of monopole currents in artificial spin ice.

Here I refer to an arrangement of nanomagnets at a vertex as a vertex configuration. For the artificial square ice designs used in this thesis, the number of nanomagnets at a vertex is at most four, meeting at a common vertex at right angles to each other. Examples of such vertex configurations are shown in Figure 7.1, in particular 4 vertex-, 3 vertex-, and 2 vertex- configurations.

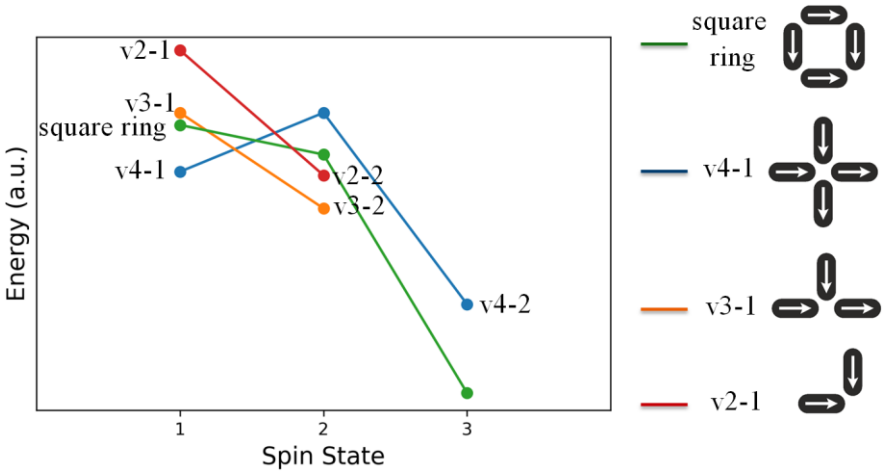

Figure 7.1: Calculated energies of different vertex configurations, shown as schematics adjacent to the plot, where the y-axis is the dipolar energy and the x-axis corresponds to the magnetic state number.

Before venturing further, it is helpful to introduce a general notation that will be used for describing different vertex configurations. This notation is v*n*-X, where v stands for vertex, *n* represents the number of nanomagnets in a particular vertex and X corresponds to either a globally field set state (1) or a relaxed ground state (2). An example of the notation would be v2-1, which refers to lowest vertex configuration in Figure 7.1.

The discrepancy in the energies of different vertex configurations is illustrated in Figure 7.1. Assuming an initial state set by a globally applied magnetic field, the relaxation pathways associated with different vertex configurations are schematically shown in Figure 7.1. The y-axis in the plot is increasing energy in arbitrary units and the x-axis corresponds to different spin states in each vertex configuration. For example, a v4-1 configuration (relaxation pathway in blue) would require traversing a spin state 2 (on the x-axis) before relaxing to a ground state at 3. Unlike a v4-1 configuration, a v2-1 configuration (shown in red) would only require one step to find its ground state at 2. Since the probability of transition from one spin state to another is dictated by the Boltzmann factor $e^{-\frac{E_T}{kT}}$, it can be seen that, under the same conditions, the probability of a v2-1 configuration to transition to a v2-2 configuration is more likely than the transition of a v4-1 configuration to a v4-2 configuration, which occurs via a metastable state.

Now that the idea of switching probabilities for different vertex configurations has been introduced, the next step is to define vertex terminations. Here the term vertex termination refers to taking an artificial spin ice, such as the artificial square ice, and populating two of its edges with a specific vertex configuration, with examples shown in Figure 7.2. I will now introduce a notation to identify artificial square ice structures with different terminating edges. The notation takes the form of v*n*-v*m*, where v stands for vertex, and n and m are the number of nanomagnets at a terminating edge in a design. The terminating edges are identified as edges with vertex configurations in a v*n*-1 (or *vm*-1) state. An example of the notation is shown in Figure 7.2b, in which an artificial square ice structure has two edges comprising two v2-1 vertex terminations and therefore it is called a v2-v2 termination design. Assuming the initial field-set state, shown in Figure 7.2 and for individual vertex structures in Figure 7.1, the energy associated with each vertex configuration and their relaxation pathway will be different. For example, an artificial square ice that is populated by v4-1 configuration in the bulk of the array could be terminated at the edges by either a v3-1 configuration or a v2-1 configuration (Figure 7.2a and b). From an energetic standpoint, an artificial square ice with the v2-1 termination, shown in Figure 7.2b, would have a higher probability of monopole injection at the termination sites, shown in blue, than in the bulk of the array. This is because the bulk of the array consists of v4-1 configurations that are energetically more stable than the v2-1 configurations. In contrast, for an artificial square ice with a v4-1 termination (Figure 7.2c), the probability of switching of a magnet away from this configuration is independent of the location of a nanomagnet, since v4-1 configurations occur both in the bulk and at the edges of the array. In a v3-1 terminated artificial square ice (Figure 7.2a) nucleation of monopoles would occur at both v2-1 sites (at the corners) and v3-1 sites (at the edges), with a

slightly higher probability to switch a nanomagnet at the v2-1 site. Among the three designs illustrated in Figure 7.2, the v2-1 termination in Figure 7.2b is the likely candidate to give injection of monopoles at the edges and generate a monopole current with monopoles propagating towards the center of the structure. It should be noted that injection of monopoles is unlikely to occur at the v2-2 terminations in Figure 7.2b i.e. those highlighted in purple. This is because the moment configurations are already in their lowest energy configuration and therefore, they are "protected".

This realization of a v2-1 structure producing location specific injection of monopoles has been known to the artificial spin ice community, although experimental attempts made to produce monopole currents were not successful[46, 48, 77, 78]. This was attributed to disorder (in the placement of individual nanomagnets or associated with a distribution of switching fields) in the artificial spin ice.

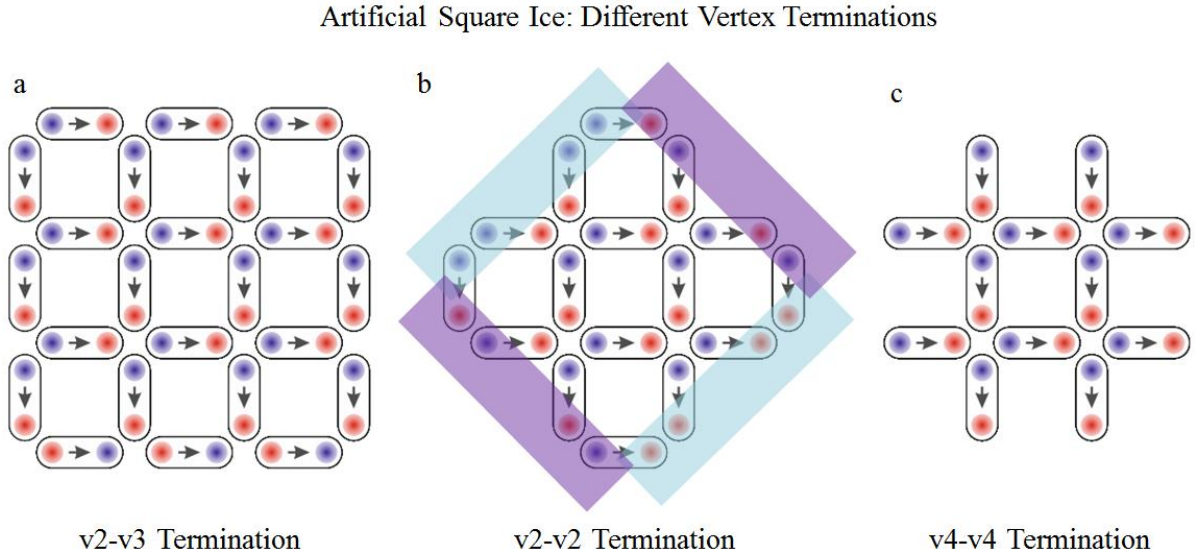

Figure 7.2: Artificial square ice structures with different vertex terminations. The v2-1 terminations highlighted in blue give a high probability of injection of monopole currents and those highlighted in purple are the v2-2 termination sites which give a low probability of injection of monopole currents.

7.1 Asymmetric Artificial Square Ice: v2-v4 Structure

As part of my project goal, not only to deterministically inject monopoles but also to create directional monopole currents, a symmetric structure such as a v2-1 termination (Figure 7.2b) would be undesirable because monopole injection would occur from two edges of the artificial square ice and the generated currents would terminate in the bulk of the structure. Therefore, a modified design needed to be created that was inherently asymmetric.

An asymmetric artificial square ice design is shown in Figure 7.3a. From now on, this design will be referred as the v2-v4 structure, consistent with the earlier introduced terminology. The design incorporates v2-1 and v4-1 terminations in order to create an asymmetry in the energies associated with each edge. This is seen in the calculated dipolar energies given in Figure 7.3b. For example, the values shown under the title "Switching of 12" in Figure 7.3b correspond to the energies associated with the switching of a numbered nanomagnet shown in Figure 7.3a. In the Figure 7.3b, the blue highlighted energy for nanomagnet 12 indicates that the number 12 nanomagnet has the highest probability to switch upon the implementation of a relaxation protocol. Therefore, it can be seen that the magnets that are most likely to change their moment orientations upon the implementation of a relaxation protocol are the magnets 12 then 9, followed by 6 then 4. Therefore, a v2-v4 structure would lead to preferential injection of monopoles at the v2-1 edge. The magnets 1, 2, 3, 7, and 8 are in a head-to-tail configuration and therefore constitute the least-probable-to-switch-edge of the design. Therefore, theoretically, the design presented in Figure 7.3 would likely produce location specific injection of monopole currents that would begin injection of monopoles at the v2-1 edge, while terminating at the v4-1 edge.

It should be noted that in the schematic in Figure 7.3a, the v4-1 edge of the design is incomplete with magnets missing on alternate sites, which leads to the edge being a combination of v4-1 and v3-1 terminations. While a true v4-1 termination in the v2-v4 structure would contain nanomagnets on all the terminating sites, such a design is experimentally not viable. I will detail the specific reasons for skipping alternate magnets in the design later in the chapter.

7.2 Preliminary Results: v2-v4 Structure

In order to test, that a v2-v4 structure truly supports directional injection of monopole currents, arrays of Permalloy nanomagnets these terminations were fabricated. The dimensions of each nanomagnet is similar to those described elsewhere in this thesis with a length of 470 nm and width of 200 nm, and the thickness was varied with the thickness increasing from 1 to 15 nm across a distance of 6 mm on the substrate. An SEM image of the v2-v4 structure is shown in Figure 7.4. The long nanomagnets (1 μm in length) on the v4-1 edge have a higher shape anisotropy that ensures that they remain thermally inactive during the course of the thermal protocol. However, it should be noted that, for the experiments described in this section, these nanomagnets were the same size as those in rest of the array. The use of long nanomagnets at the v4-1 termination sites will be relevant in the later sections. Experiments were performed using X-PEEM at the SLS, heating the substrate in order to allow the structure to thermally relax.

a

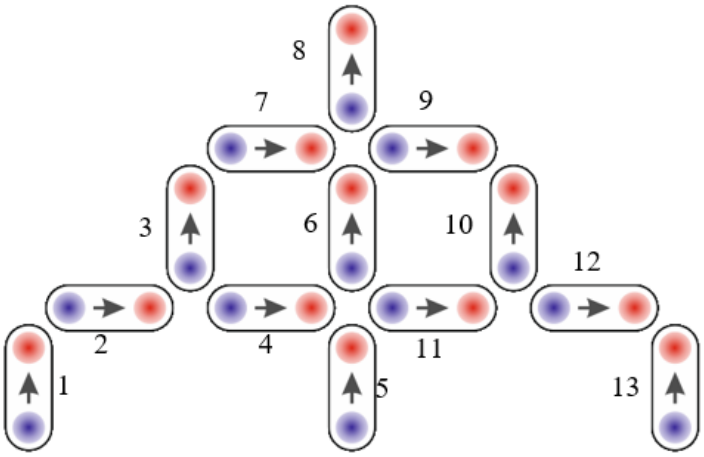

b

Calculated energies during relaxation

Switching of 12		After switching of 12		After switching of 9		After switching of 6	
	Energy/kT		Energy/kT		Energy/kT		Energy/kT
1	1288.16	1	-365.107	1	-1148.18	1	-2791.9
2	3078.647	2	1390.177	2	567.9659	2	-1219.39
3	978.9002	3	-650.207	3	-1528.27	3	-2646.33
4	-45.6934	4	-1830.07	4	-2680.39	4	-6656.69
5	641.5718	5	-1130.66	5	-2008.71	5	-4762.34
6	525.6886	6	-998.265	6	-4065.26	6	-4065.26
7	1463.781	7	-252.574	7	-2096.91	7	-1447.08
8	721.7664	8	-840.65	8	718.4647	8	-2035.16
9	-657.562	9	-2402.02	9	908.9075	9	908.9075
10	-1.32E+03	10	-650.207	10	-1033.26	10	165.4769
11	1.91E+03	11	-824.523	11	-2402.02	11	1979.533
12	-1646.92	12	-1648.08	12		12	
13	-1.29E+03	13		13		13	

Figure 7.3: (a) A modified artificial square ice to facilitate deterministic injection of monopole currents. (b) Energies associated with different moment configurations assuming the application of a relaxation protocol to the moment configuration in (a). The nanomagnets with highest probability to switch is shown in blue.

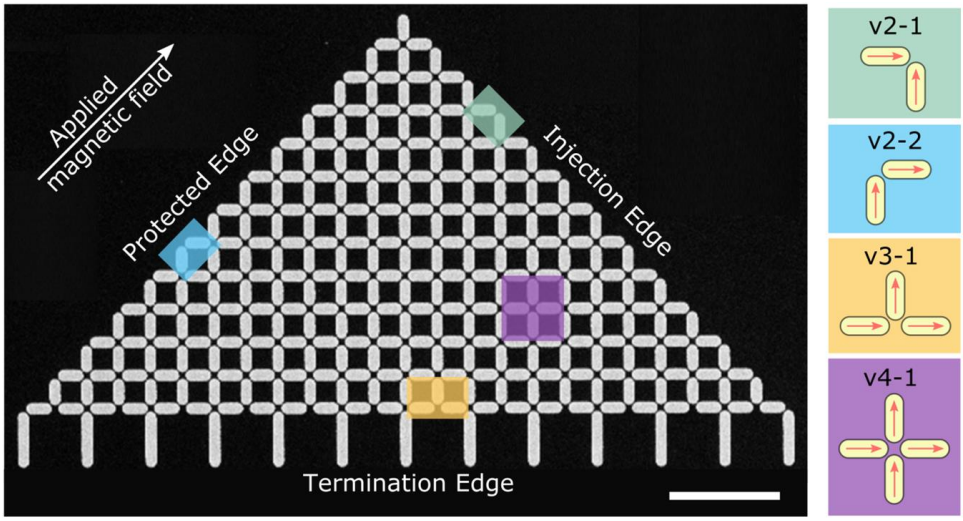

Figure 7.4: An SEM image of the v2-v4 structure. The scale bar is 2 μm. Shown are different regions associated with different vertex terminations, assuming a globally applied field, whose direction is indicated with a white arrow. Injection is expected to occur at the v2-1 termination on the right edge (injection edge) of the structure, while the v4-1 termination edge is where the monopole currents are expected to end. The other v2-2 termination, on the left edge of the structure, is protected since the applied field sets the moment orientations to the lowest energy state. Schematics of the moment orientations in different parts of the v2-v4 structure are shown to the right of the image.

The results of the first experiment with a v2-v4 structure are shown as X-PEEM magnetic contrast images in Figure 7.5. An initial state was set using an external magnetic field, with its direction indicated in Figure 7.5a. As opposed to the expected all-white contrast in the initial state, it was found that the initial field-set state was either incomplete or quickly developed defects corresponding to the nanomagnets with black contrast in Figure 7.5a. Due to a lack of additional experimental time to fix the error with the initial field-set state, I proceeded to allow thermal relaxation of the moment reorientations in the "defective" v2-v4 structure in order to see if the monopoles propagate in a particular direction.

The thermal relaxation of the magnetic moments in the sample was performed by heating it to a temperature of ~100 ^{o}C, during which XMCD imaging was performed to monitor the nanomagnetic moment reorientations in the array, with the initial state in Figure 7.5a and the final state captured in Figure 7.5g.

Upon closer inspection, it was found that, even though initially the images looked like defects were occurring at random, there was a consistent trend in the direction of the generated monopole currents. The entire set of images was split into 14 time chunks and monopole propagation directions were recorded for each (Figure 7.6b). The two possible directions of monopole propagation, which

corresponds to the string expansion indicated with red and blue arrows in Figure 7.6a, are associated with the change of moment orientation in an additional neighboring nanomagnet. The string expansion direction is then given by the location of the neighboring nanomagnet. It was found that there was a preferred direction of string expansion and therefore monopole propagation towards the v4-1 termination.

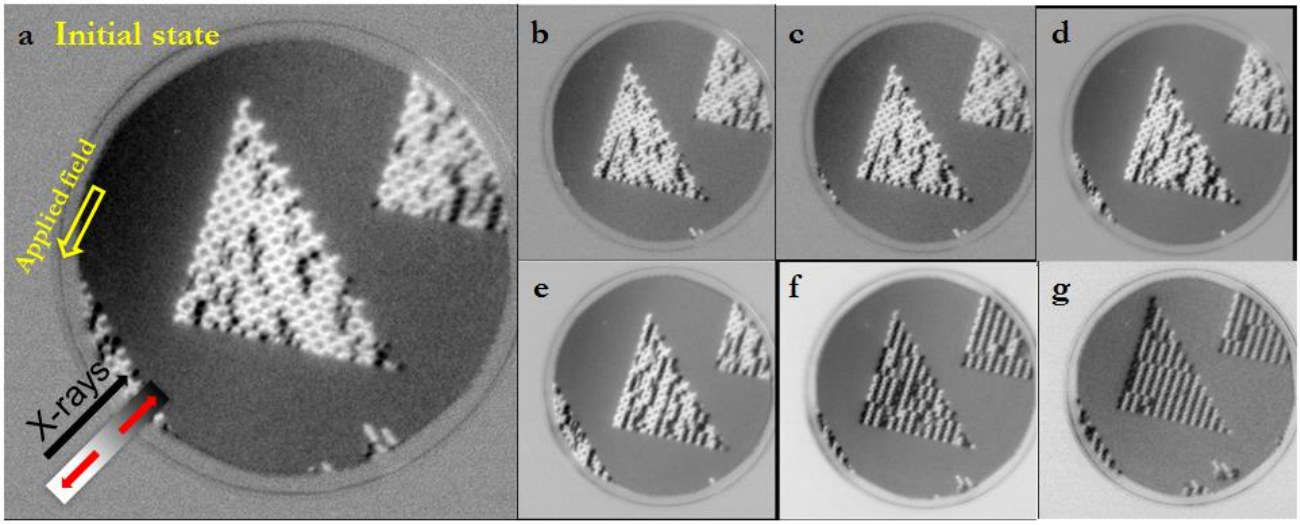

Figure 7.5: X-PEEM images of dynamics in a v2-v4 structure from an initial field set state (a) to a final domain state (g). Monopole propagation was observed to occur predominantly towards the v4 termination.

Even though the experiment did not conclusively demonstrate directional injection of monopole currents, it seemed that injection events were likely to occur at the v2-1 termination and that the v2-v4 structure might sustain directional currents. The experiment also provided insights into how to develop a thermal protocol. A key component in the development of a thermal protocol is to take into account the change in temperature when heating. This is because, a large increase in the temperature might lead to a change in the probability of the occurrence of certain moment reorientations. Therefore, the increase of temperature should be small enough to ensure that injection events are restricted to specific locations.

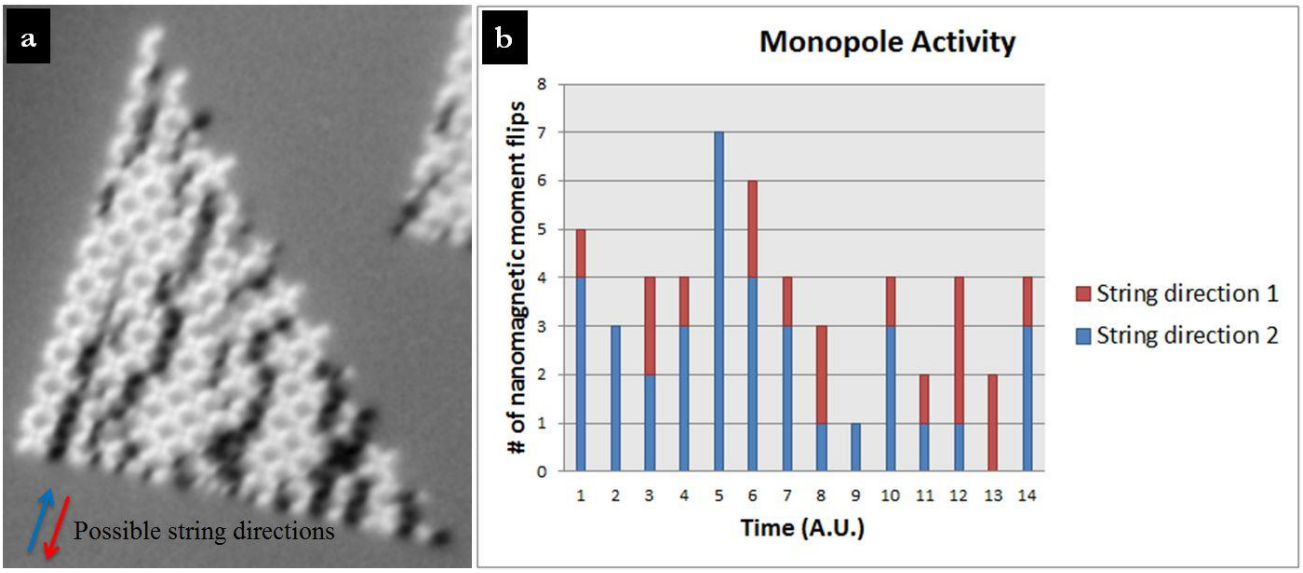

Figure 7.6: Monopole propagation direction associated with string expansion in a v2-v4 structure. (a) The direction of expansion of a string is indicated by the red and blue arrows. (b) Expansion events are shown as a function of time. Here, it is observed that string expansion along direction 2 is larger than the string expansion along direction 1 at the beginning of the thermal protocol.

7.3 v2-v4 Structure Including Longer Nanomagnets

Encouraged by the preliminary results from the v2-v4 structure, additional experiments were performed on a multitude of designs involving an artificial square ice with different vertex terminations. Unlike for the preliminary experiments discussed in the earlier subsection, the v4-1 termination now included longer nanomagnets as shown in the SEM image of the v2-v4 structure in Figure 7.4. The longer nanomagnets have a larger energy barrier to overcome during the thermal protocol and therefore retain their initial field-set state during thermal relaxation. Such a pinned set of nanomagnets would also ensure that monopole injection events are now completely restricted to the v2-1 termination sites. It should be noted here that the design in Figure 7.4 does not comprise a true v4-1 edge, since nanomagnets are missing on alternate sites. Such a modified design was necessary in a v2-v4 structure with longer nanomagnets at the v4-1 termination sites, in order to facilitate access to the ground state. As before, the initial state was set with an external field, but this time along the direction shown in Figure 7.4. Unlike the preliminary experiment on the v2-v4 structure described in the previous section, the applied field is now in the opposite direction and therefore, for the initial field-set state, the nanomagnets appear “all-black”.

Key stages in the observed dynamics of the v2-v4 structure are shown in Figure 7.7. Four distinct dynamic regimes were observed: (1) initial injection of monopoles (Figure 7.7a), (2) fast paced motion of monopoles, often terminating within the structure (Figure 7.7b), (3) formation of domains

(Figure 7.7c), and (4) ground state ordering (Figure 7.7d). The associated thermal protocol is shown in Figure 7.7e, in which the temperature associated with X-PEEM images in 7.7a-d is marked.

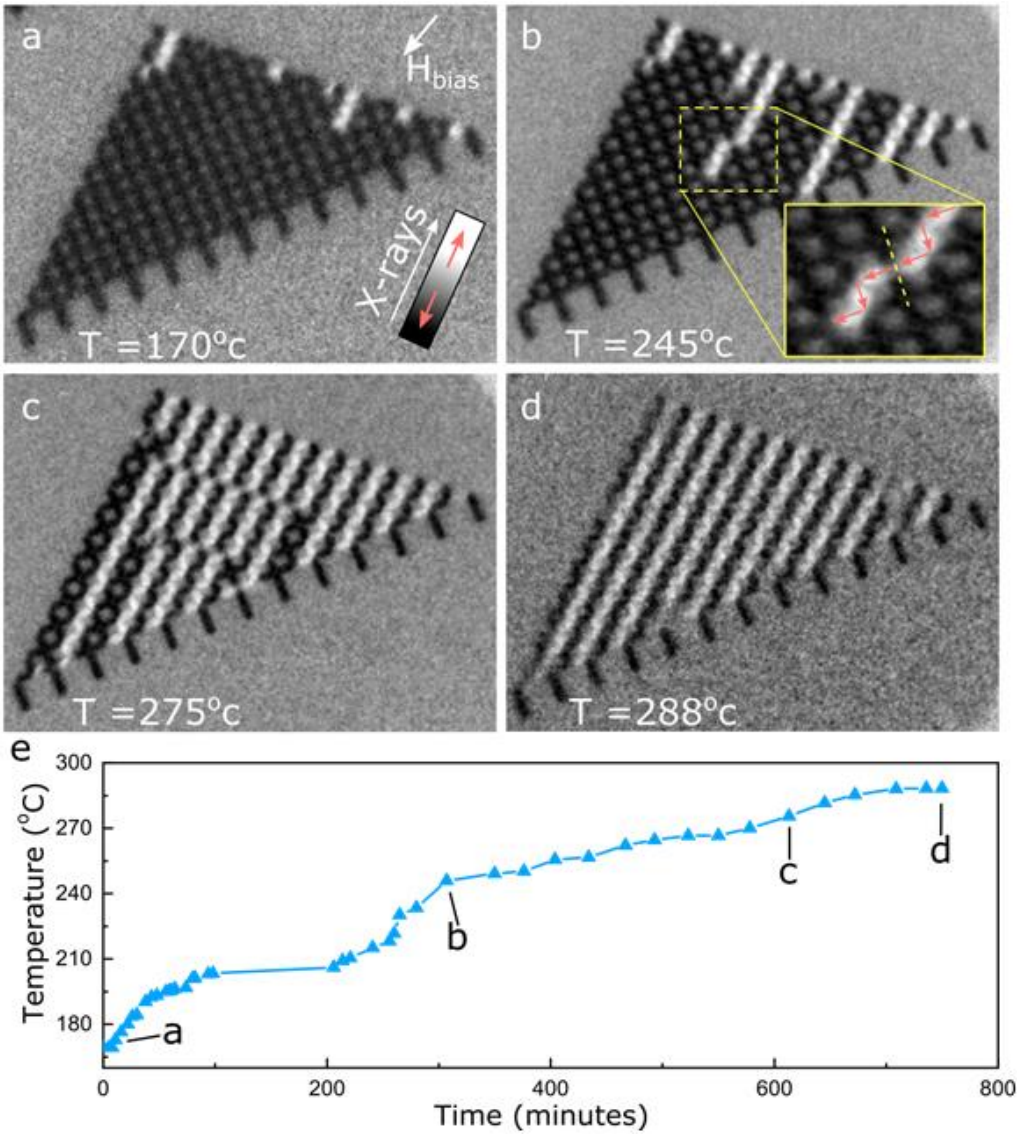

Figure 7.7: Dynamics observed in a v2-v4 structure in which different regimes corresponding to (a) initial injection of monopoles, (b) fast paced motion of monopole currents, often terminating within the structure, (c) formation of domains, and (d) ground state ordering are shown. The temperature of the sample for each X-PEEM image is given in the images. The implemented thermal protocol is shown in (e), in which the y-axis corresponds to the temperature and the x-axis is the change in time.

I will now expand on the observed dynamics in each of the four regimes in detail:

(1) Initial injection of monopoles

The initial injection of the monopoles (7.7a) is completely restricted to the v2-1 sites as predicted. However, it should be noted that this is further restricted to nanomagnets that are approximately parallel to the H_{bias}. The presence of such a spurious external magnetic field, H_{bias}, has been observed by others and was measured to be 30 – 50 μT[71]. If not for the H_{bias}, nucleation would still occur at the v2-1 sites but there would be an equal probability of switching in the nanomagnets with both orientations comprising the v2-1 site. Once the injected, the monopoles propagate, creating currents as the applied heat is increased (Figure 7.7e).

I take this opportunity to detail some of the technical difficulties in X-PEEM imaging that I often encountered while a thermal protocol was being implemented. These were (1) poor image quality and (2) image drift. During the course of a thermal protocol, the metallic holder that houses the sample may mechanically distort as a response to changes in the applied temperature. Since the sample is effectively part of the electron optics of the X-PEEM, this can result in a change in focus. The distortion of the metallic holder also means that the sample itself may slightly change its location, or drift, with respect to the region currently being imaged. It was therefore often required to wait for a sufficient amount of time for the distortions in the sample holder to stabilize at a particular temperature before imaging. Other issues such as the release of water vapor or other contaminants (outgassing) may occur at elevated temperatures and can lead to a reduction in image quality. Thus, during an outgassing event, it was often necessary that sufficient time was allowed to pass before good quality imaging of the nanomagnets could be performed. Imaging magnetic moment reorientation dynamics during the course of a thermal protocol was therefore often challenging.

(2) Fast paced motion of monopole currents, often terminating within the structure

As the temperature is further raised, the monopoles that are injected at v2-1 site proceed into the bulk of the structure as a fast paced current. These currents were observed to often terminate within the structure, followed by shifting to a different lattice. The shifting of the monopole currents can be visualized by considering the structure in Figure 7.3. As I have discussed previously, energetics tell us that the structure in Figure 7.3 would follow a specific relaxation pathway in which, if an injection associated with the nanomagnet numbered 9 were to occur, it is highly likely that the moments in 6 and 4 would follow suit sequentially. Such a relaxation, with moment reorientations starting with nanomagnet 9, followed by 6 and then 4 would constitute a monopole current. A shifting of such a current happens if, instead of 6, nanomagnet 7 would switch. Experimentally, such a shifting of the monopole currents to a neighboring lattice is highlighted in the inset provided in Figure 7.7b. Shifting of the monopole currents has been attributed to disorder in the nanomagnets or the inherent nature of

relaxation pathways, where there is always a certain probability of the shifting to occur. However, the latter explanation, where the shifting is assessed to be a purely statistical event, is not consistent with the large number of monopole currents that were experimentally observed to shift. At this point, I sought help from E.Y. Vedmedenko, a theoretical expert in magnetism from the University of Hamburg.

E.Y. Vedmedenko previously found that a simple dipolar approximation for nanomagnets would often give an underestimation of the experimentally obtained coercivity in arrays of nanomagnets[79]. She therefore proposed that the Hamiltonian for a simple dipolar approximation needed to include additional corrections in the form of higher order contributions that would predict coercivities that are comparable to those obtained experimentally.

The modified Hamiltonian in which higher order magnetostatic contributions are considered in arrays of nanomagnets takes the following form:

$$H = \frac{1}{4\pi\mu_0} \sum_{\substack{A\neq B \\ l_A l_B m_A m_B}} T_{l_A l_B m_A m_B}(\vec{R}_{AB}) Q^A_{l_A m_A} \quad (7.1)$$

Here, the multipolar interaction is described in spherical coordinates, where $Q^A_{l_A m_A}$ and $Q^B_{l_B m_B}$ are the moments of multipoles A and B expressed in spherical harmonics[79, 80] and $T_{l_A l_B m_A m_B}(\vec{R}_{AB})$ is the geometric interaction tensor depending on the interparticle distance vector $\vec{R}_{AB}$ between multipoles on sites A and B

$$T_{l_A l_B m_A m_B}(\vec{R}_{AB}) = (-1)^{l_B} I^*_{l_A+l_B\ m_A+m_B}(\vec{R}_{AB}) \times \sqrt{\frac{(l_A+l_B-m_A-m_B)!}{(l_A-m_A)!(l_B-m_B)!}\frac{(l_A+l_B+m_A+m_B)!}{(l_A+m_A)!(l_B+m_B)!}} \quad (7.2)$$

where the dependency on the distance is given by the complex conjugate of the irregular normalized spherical harmonic function:

$$I_{l\,m}(\vec{r}) = \sqrt{\frac{4\pi}{2l+1}}\frac{Y_{l\,m}(\theta,\varphi)}{r^{l+1}} \quad (7.3)$$

Analytical calculations were performed to compare the energy difference from a simple dipolar approximation to that of a Hamiltonian in which octopolar contributions were taken into account. It should be noted that higher order contributions to the magnetic Hamiltonian is highly symmetry dependent and it was previously reported[79] by E.Y. Vedmedenko and her colleagues that particles such as cylindrical disks and those possessing fourfold symmetry have a vanishing Q_{lm} when *l* is 2, *i.e.* the quadrupole term vanishes. The nanomagnets we use in the thesis are a composite of a rectangle and two circles, in which we expect the magnetization to be centrosymmetric. As found by E.Y. Vedmedenko and her colleagues, in a centrosymmetric magnetic particle, the quadrupole

contribution vanishes while leaving the octupole term intact. It was found that, in a v2-v4 structure, the excess energy from an initial field-set state to that of a ground state was 3 times larger when octopolar contributions are taken into account.

$$\frac{[\mathrm{E_{GS}}(\text{dipole} + \text{octopole}) - \mathrm{E_{field-set}}(\text{dipolar} + \text{octopole})]}{\mathrm{E_{GS}}(\text{dipole}) - \mathrm{E_{field-set}}(\text{dipole})} \sim 3 \quad (7.4)$$

Such an excess energy increases the transition probability from an initial field-set configuration to a shifted vertex configuration in the v2-v4 structure and therefore shifting of monopole currents is more likely to occur. This reasoning, that higher order contributions to the Hamiltonian are responsible for the shifting, was confirmed using Monte-Carlo simulations where the magnetic ordering at different Monte-Carlo time steps (Figure 7.8) mimicked the experimentally observed dynamics (Figure 7.7). Monte-Carlo simulations were performed by considering the v2-v4 structure in an initial field-set state as shown in Figure 7.4. At each Monte-Carlo step, the magnetization of a randomly chosen dipole or multipole is randomly switched and the change in energy is calculated by using equation (7.1). The probability of the new configuration, *p*, was obtained using the Boltzmann factor $e^{-\frac{E_T}{kT}}$. $\mathrm{E_T}$ is the barrier energy given by Equation 2.13. A random number, *r*, was then chosen between 0 to 1 and the step was accepted or rejected if $p>r$. Several runs were performed using different random number seeds to check for statistical validity. The nanomagnets in the simulated array had dimensions of 470 nm × 200 nm, and a thickness of 3 nm was assumed. Figure 7.8 contains the Monte-Carlo data for the four regimes that were experimentally observed: (1) initial injection at the v2-1 sites (Figure 7.8a), (2) fast paced current, in which shifting is observed (Figure 7.8b), (3) domain formation (Figure 7.8c), and (4) perfect ground state ordering (7.8d). It should be noted that the Monte-Carlo simulation was stopped slightly pre-maturely and therefore a single moment in Figure 7.8d (black circle) is not found in its low energy state.

(3) and (4) Formation of domains and ground state

I have grouped the final two regimes together since it is convenient to explain them as part of the same set of dynamics. After the monopoles shift within the v2-v4 structure, they continue to propagate towards the v4-1 termination sites. Throughout these observed dynamics, the temperature is gently raised to facilitate their propagation (Figure 7.7e) and the shifting of the monopole currents leads to the formation of shifted domains in the v2-v4 structure. The shifted domains are seen in Figure 7.7c and Figure 7.8c for the experimentally observed dynamics and for the Monte-Carlo simulations, respectively. Additional heating is required for the domains to re-arrange themselves to reach a fully ordered low energy state. The ground state ordering for the experimentally observed and analytically calculated v2-v4 structure is shown in Figure 7.7d and Figure 7.8d, respectively. A more detailed set of the experimentally observed dynamics is given in Figure 7.9.

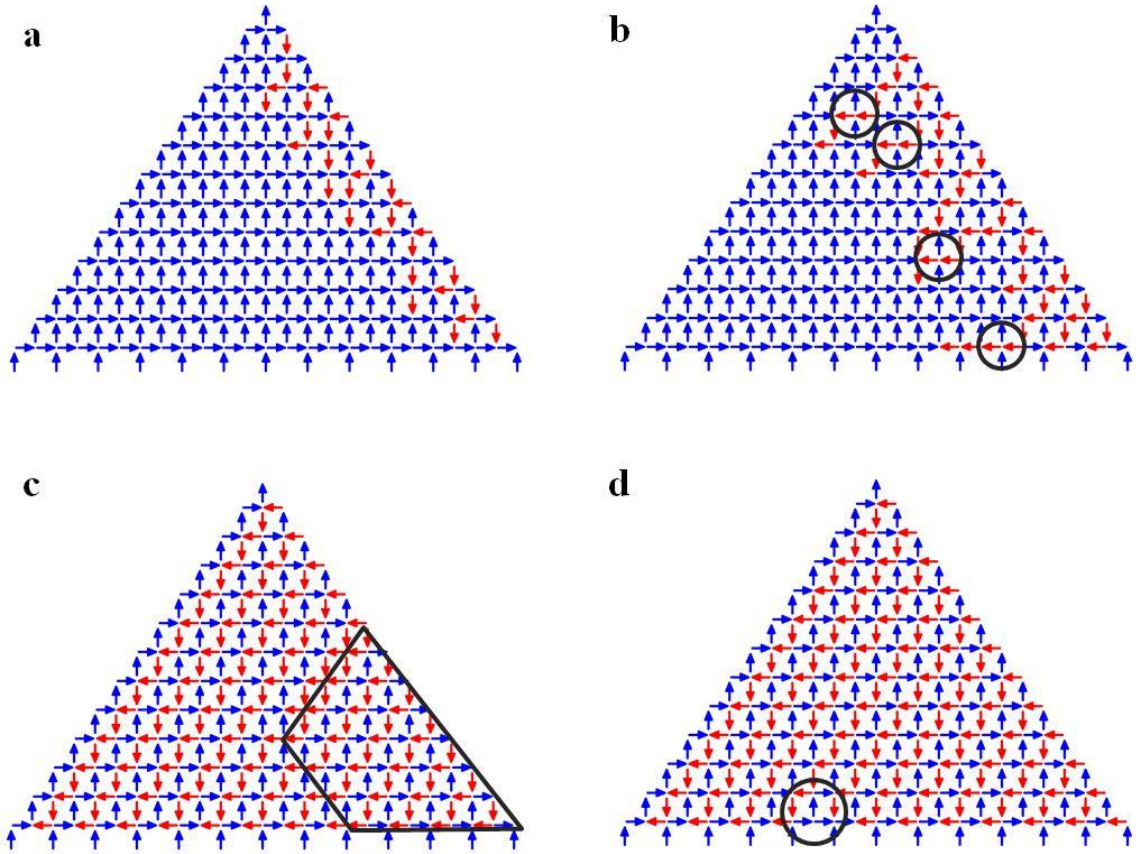

Figure 7.8: Monte-Carlo simulation data for a v2-v4 structure, in which the dynamics is similar to that observed experimentally. The four observed regimes are (a) injection of monopoles, (b) shifting of the monopole currents, (c) domain formation, and (d) ground state ordering. It should be noted that the simulation was prematurely terminated and therefore one of the moments in (d) was not in a low energy state (black circle).

From this experiment, and with the experience gained from the partial failure of the preliminary v2-v4 structure's dynamics, it is possible to draw a few conclusions on why others have not been able to deterministically inject and control monopole currents. Two main factors may be identified that have the largest impact on the deterministic injection of monopole currents. These are: (1) the implemented relaxation protocol by others probably involved large step size in the applied field or heat, as was observed to be the case in our preliminary v2-v4 structure experiments, and (2) the array design was not asymmetric. However, the termination edges need to be different in order to facilitate a location specific injection of monopoles, which defines their subsequent propagation.

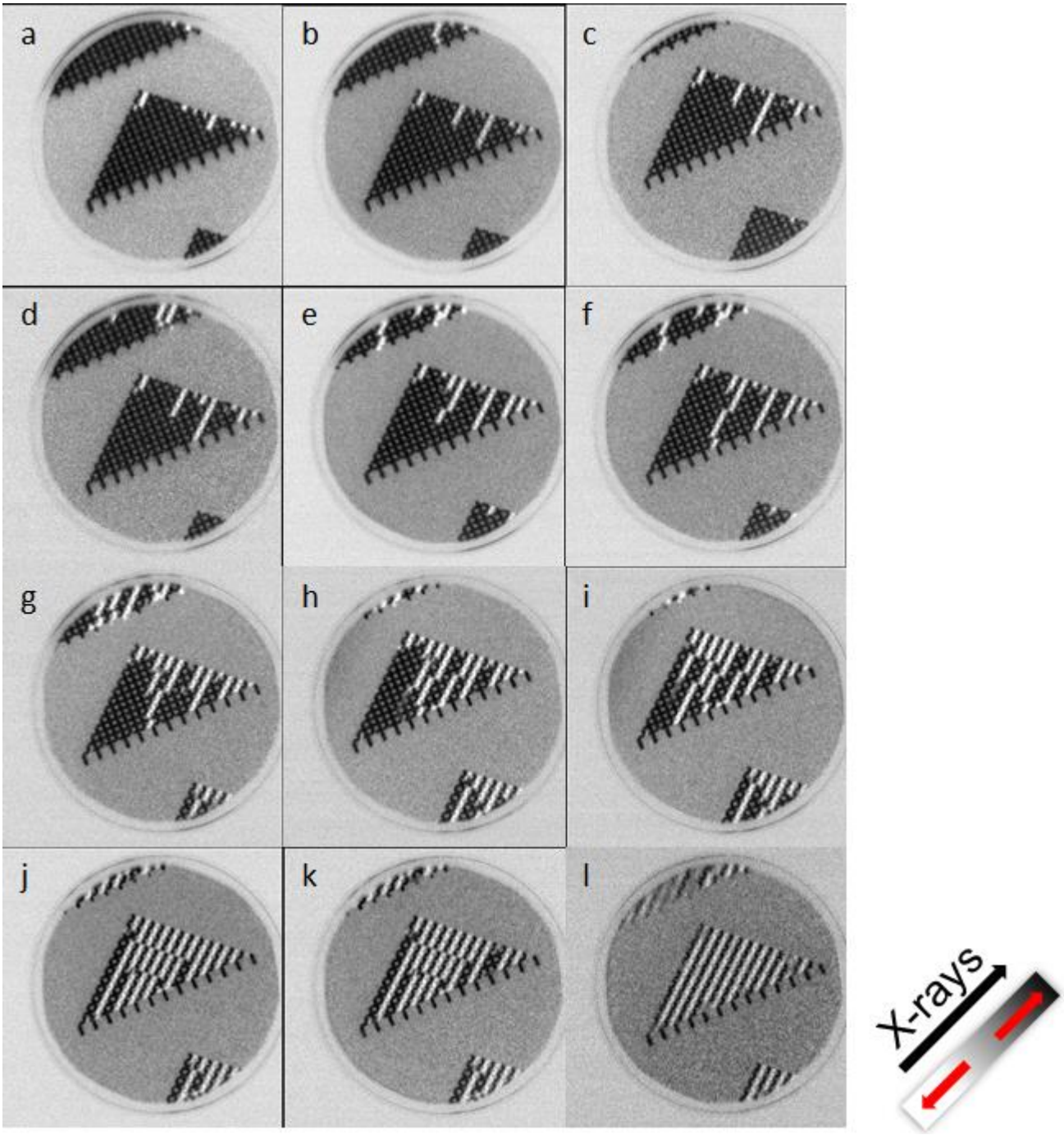

Figure 7.9: Detailed X-PEEM images of the dynamics in a v2-v4 structure, for which snapshot shots were shown in Figure 7.7

With the v2-v4 structure experiment, we therefore demonstrated conclusively that it is possible to inject monopoles at a location of choice and constrain the propagation of the generated monopole currents in a specific direction towards a specific edge.

7.4 Other Artificial Square Ice Structures

In addition to the v2-v4 structure, I have also measured the dynamics in structures with other terminations in order to test whether the different vertex terminations can be used to control the injection of monopole currents. A v2-1 termination has always been the typical test bed for theoreticians in the artificial spin ice community to predict monopole dynamics in artificial square ice. Therefore, I experimentally tested a v2-1 terminated square ice (or v2-v2 structure) that has a symmetric design. Here, the injection of monopole currents occurs at both of the v2-1 termination edges (Figure 7.10 a-d). The generated monopoles from the edges can annihilate each other somewhere in the bulk of the structure. Similarly, in an asymmetric artificial square ice, in which one edge has a v3-1 termination while the other is a v2-1 termination (v2-v3 structure), monopole currents would preferentially inject at the v2-1 sites (Figure 7.10 e-h). However, unlike the v2-v4 structure shown in Figure 7.7 in which the energy difference between the v2-1 configuration and v4-1 configuration is large, the energy difference between a v2-1 configuration and a v3-1 configuration is rather small. Therefore, in a v2-v3 structure (Figure 7.10e), the injection is not purely restricted to the v2-1 termination (Figure 7.10f). It should be noted that the experiments were performed using the same thermal protocol as that described for the v2-v4 structure in the earlier sections of this chapter.

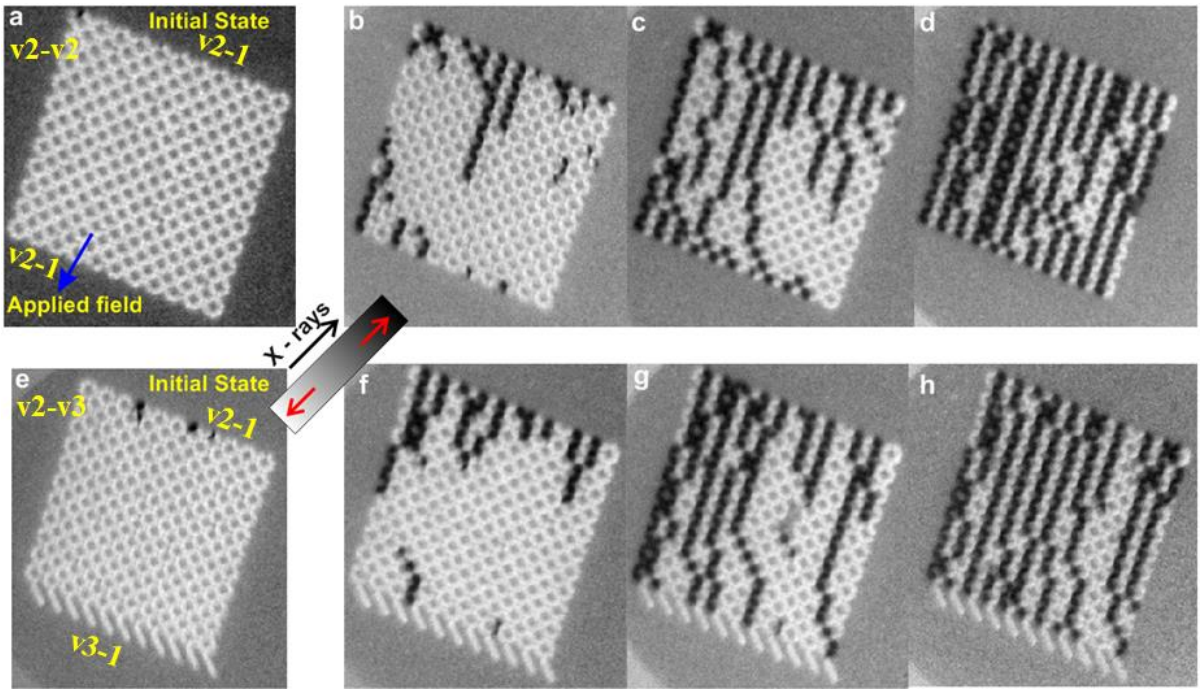

Figure 7.10: X-PEEM images of artificial square ice structures (a) v2-v2 and (e) v2-v3. The observed dynamics for (a) and (e) are shown in (b-d) and (f-h). Final ground state ordering is not shown since it is not relevant to the question of the specific location of injection of monopole currents.

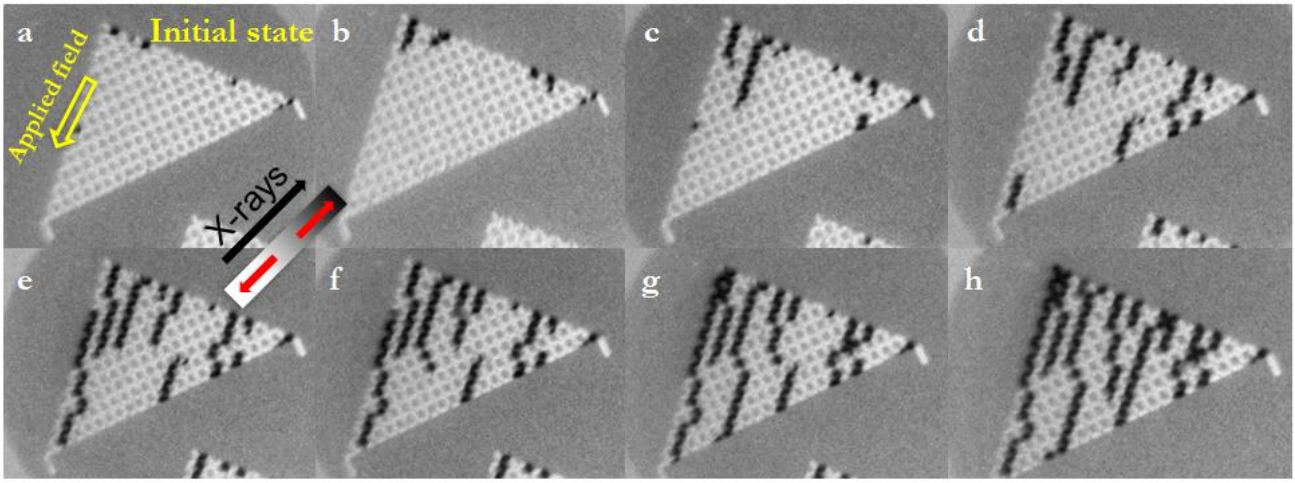

Figure 7.11: X-PEEM images of the dynamics in a modified v2-v4 structure, where the v4-1 termination sites were completely removed so giving a v3-1 termination. The initial state is shown in (a) and injection of monopoles now occurs at both v2-1 and v3-1 sites (b-h).

I also tested a modified version of the v2-v4 structure shown in Figure 7.7. Here the long islands at the v4-1 termination were removed to give the v3-1 termination shown in Figure 7.11a. This modified version of the v2-v4 structure therefore has the same terminations as the square v2-v3 structure shown in Figure 7.10e. It was found that the injection of monopole currents was then not fully restricted to the v2-1 termination sites but were also observed at the v3-1 site (Figure 7.11 a-h), similar to the behavior observed for the v2-v3 square structure shown in Figure 7.10e.

Shifting of the monopole currents to a neighboring lattice, similar to that observed in the v2-v4 structure, was also observed in artificial square ice structures with different terminating edges.

7.5 Monopole Injection Probabilities

During the course of experimentally testing injection of monopole currents in different artificial square ice structures, it was observed that it was necessary to find an optimal nanomagnet thickness to facilitate injection events at specific locations. Therefore, a natural question to pose here is, is there a correlation between the sample thickness and the location of injection in arrays of nanomagnets? An answer to the question would help us identify the factors responsible for the failure or the success of controlled injection and propagation of monopole currents in artificial spin ice and may provide additional insight into previously reported experiments in which deterministic injection of monopoles proved elusive[48, 49, 78].

An experiment to determine the correlation between sample thickness or, more appropriately, the change in energy between an initial field-set state to that of a relaxed state (ΔE) with respect to kT

($\frac{\Delta E}{kT}$), and the location of monopole nucleation could be performed in one of two ways: (1) image different nanomagnet arrays of a constant thickness at different temperatures or (2) image nanomagnet arrays of different thicknesses at a constant temperature. Due to a lack of a Proportional-Integral-Derivative (PID) controller in the current sample set-up that would monitor the temperature and correct for fluctuations, so delivering a constant temperature throughout the experiment, it was virtually impossible to accurately heat the sample to a specific temperature. Therefore, it made sense to image arrays of nanomagnets at different thicknesses while maintaining a constant temperature where the moment reorientations occurred slow enough so that the instantaneous magnetic configurations could be recorded i.e. they were frozen at the imaging timescale.

Typically, for the experiments described in this thesis, the temperature in the sample was raised during the observations to increase the rate of relaxation until a ground state was observed in the nanomagnet arrays (see Section 3.3 in Chapter 3). However, in order to assess the influence of $\frac{\Delta E}{kT}$ on the location of injection of monopole currents, a constant temperature needs to be maintained that is high enough to facilitate moment reorientations in the nanomagnets that can be imaged in the X-PEEM. Therefore, at an arbitrary temperature (>50 ^{o}C), the heating was stopped and different arrays with different nanomagnet thicknesses were imaged. As explained in the methods section, I deposited Permalloy as a wedge film and therefore have access to different nanomagnet thicknesses on a single substrate. The imaging yielded a correlation between nanomagnet thickness and the location of monopole injection. It was observed that, for thin nanomagnet arrays whose thickness was measured to be ~3 nm, the monopole injection occurred anywhere on the structures. However, for thicker nanomagnet arrays with a value of ~4 nm, the monopole injection was restricted to the vertex terminations. An example of monopole injection that occurs at different locations for v2-v4 structure is given in Figure 7.12. It is observed that, in thinner arrays, the injection occurs everywhere in the structure (red circled regions in images 3 and 4 in Figure 7.12), while in the thicker arrays, the injection is restricted to both v2-1 and v4-1 terminations (red circled regions in images 7 and 8 in Figure 7.12). The deterministic injection of monopole currents observed in v2-v4 structure (Figure 7.7), in which injection was restricted to v2-1 termination sites, was at a higher thickness of ~5.5 nm. Such a correlation between nanomagnet thickness and the location of monopole injection was also observed in other artificial square ice structures with different vertex terminations (also shown in Figure 7.12).

Therefore, in order to facilitate location specific injection of monopole currents, the interplay between the intrinsic energy barriers to switching and the type of vertex terminations needs to be carefully considered.

At this stage, I thought that there may be a quantitative approach to plotting switching probabilities as a function of sample thickness, which would reflect the experimentally observed results. Such a plot of the switching probability versus nanomagnet thickness for different vertex

configurations is shown in Figure 7.13a. The plot was generated by E.Y. Vedmedenko; a theoretician introduced earlier in this chapter.

The plot in Figure 7.13a was generated by considering the switching probability $P \sim e^{-\frac{\Delta E}{kT}}$, in which ΔE is the energy change for a particular vertex termination from an initial field-set state to the closest metastable state. The thickness (t) and the magnetic moment (μ) were scaled to the nanomagnets with dimensions of 470 nm (length) × 200 nm (width) × 9 nm (height/thickness). The plot shown in Figure 7.13a is the calculated switching probabilities for different vertex configurations in which, the y-axis indicates an increasing probability of switching, while the x-axis is increasing thickness of the nanomagnet as a function of moment strength with respect to the reference thickness (t_r) of 9 nm, at a constant temperature of 170 K. Even though the plot was generated by considering the switching probability, P, for isolated vertices, these switching probabilities at the termination edges in extended arrays of nanomagnets are expected to be very similar. The switching probabilities are marked by yellow triangles, green triangles, and red circles for vertex configurations of v2-1, v3-1, and v4-1. While the switching probabilities for v2-2, v3-2, and v4-2 are indicated by purple diamonds, blue triangles, and black squares respectively. At a very low thickness, x-axis close to 0, all vertex terminations are injection sites – therefore all symbols indicating different vertex configurations are located on top of each other representing a probability of 1. At the maximum thickness, $t/t_r = 1$, the injection is primarily restricted to the v2-1 termination sites.

Schematics of artificial square ice structures with different vertex terminating edges, corresponding to the calculated switching probabilities in Figure 7.13a, are qualitatively shown in Figure 7.13 b-j, with the solid lines used to distinguish structures with different thicknesses. For example, the v2-v4 structure shown in Figures 7.13b, c and d are for small, medium, and large nanomagnet thicknesses, respectively. Here, the probability of injection at a particular location is highlighted with a red-white color scale. At low thicknesses, the v2-v4 structure is expected to have injection sites at arbitrary locations in the structure (Figure 7.13b). At a higher thickness, the injection is restricted to v2-1 and v4-1 terminations (Figure 7.13c). While at high thicknesses, the injection is confined to v2-1 termination sites (Figure 7.13d). It should be noted that we introduce the v4-1* nomenclature in Figure 7.13d, which refers to the v4-1 termination in a v2-v4 structure where the asterisk indicates that the experimentally tested structure had nanomagnets missing on alternate sites and therefore did not constitute a true v4-1 termination edge. The calculated switching probabilities shown in Figure 7.13 qualitatively correspond to the moment dynamics experimentally observed in the v2-v4 structure described in the earlier sections (Figure 7.7 and Figure 7.12). Similarly, other artificial square ice designs with different vertex terminations are observed to follow the injection probabilities (Figure 7.10 and Figure 7.11), in which v2-1 configuration would often be the location of injection while v3-1 and v4-1 configurations would act as terminating sites schematically shown in Figure 7.13.

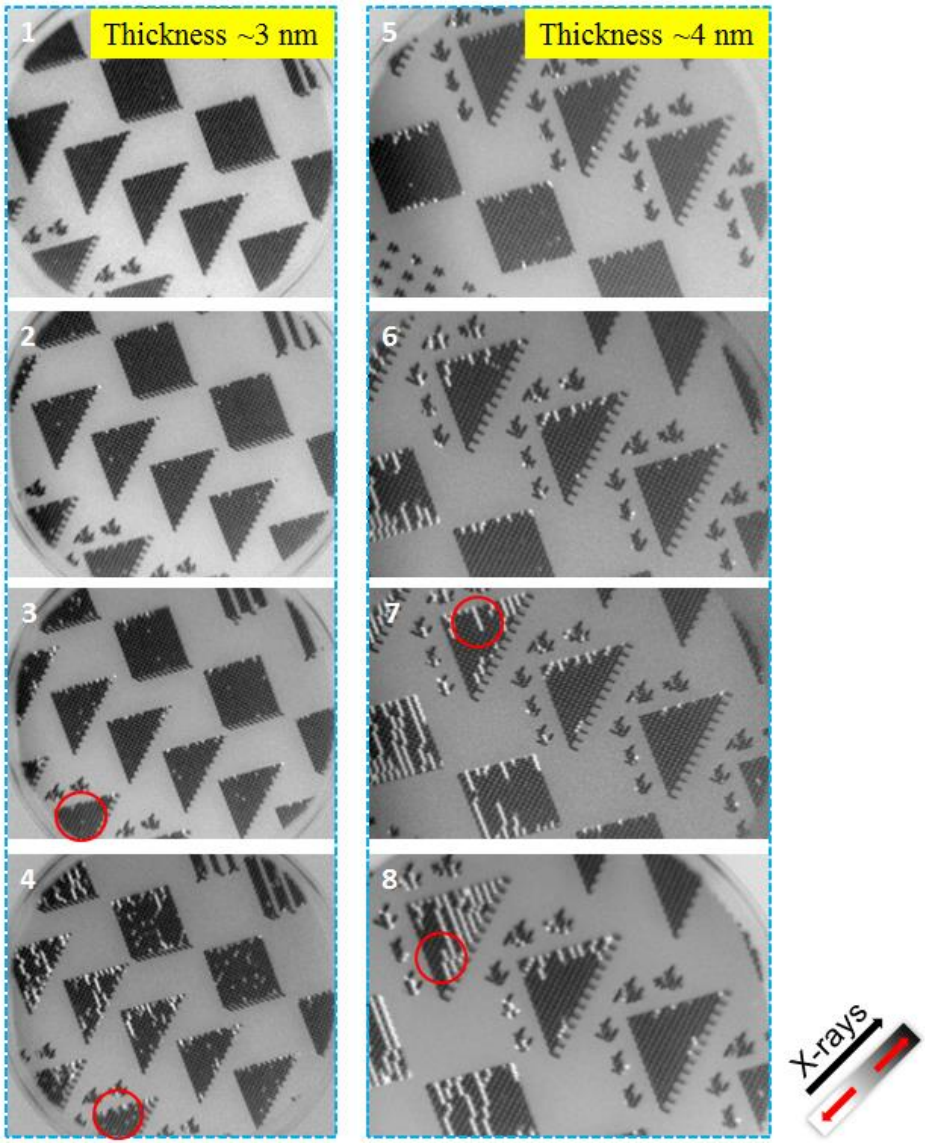

Figure 7.12: X-PEEM images of artificial square ice with different vertex terminations obtained for a thickness of (1-4) ~3 nm and (5-8) ~4 nm. (2-4) are a time sequence of images with the initial state in (1). (3 and 4) Regions highlighted with the red circles are in the v2-v4 structure where injection of monopoles is observed to occur anywhere on the structure. (6-8) are time sequence images from an initial state (5) in which, for example, the region shown by the red circles in (7) and (8), it is observed that the injection of monopoles in a v2-v4 is restricted to the termination sites of v2-1 and v4-1

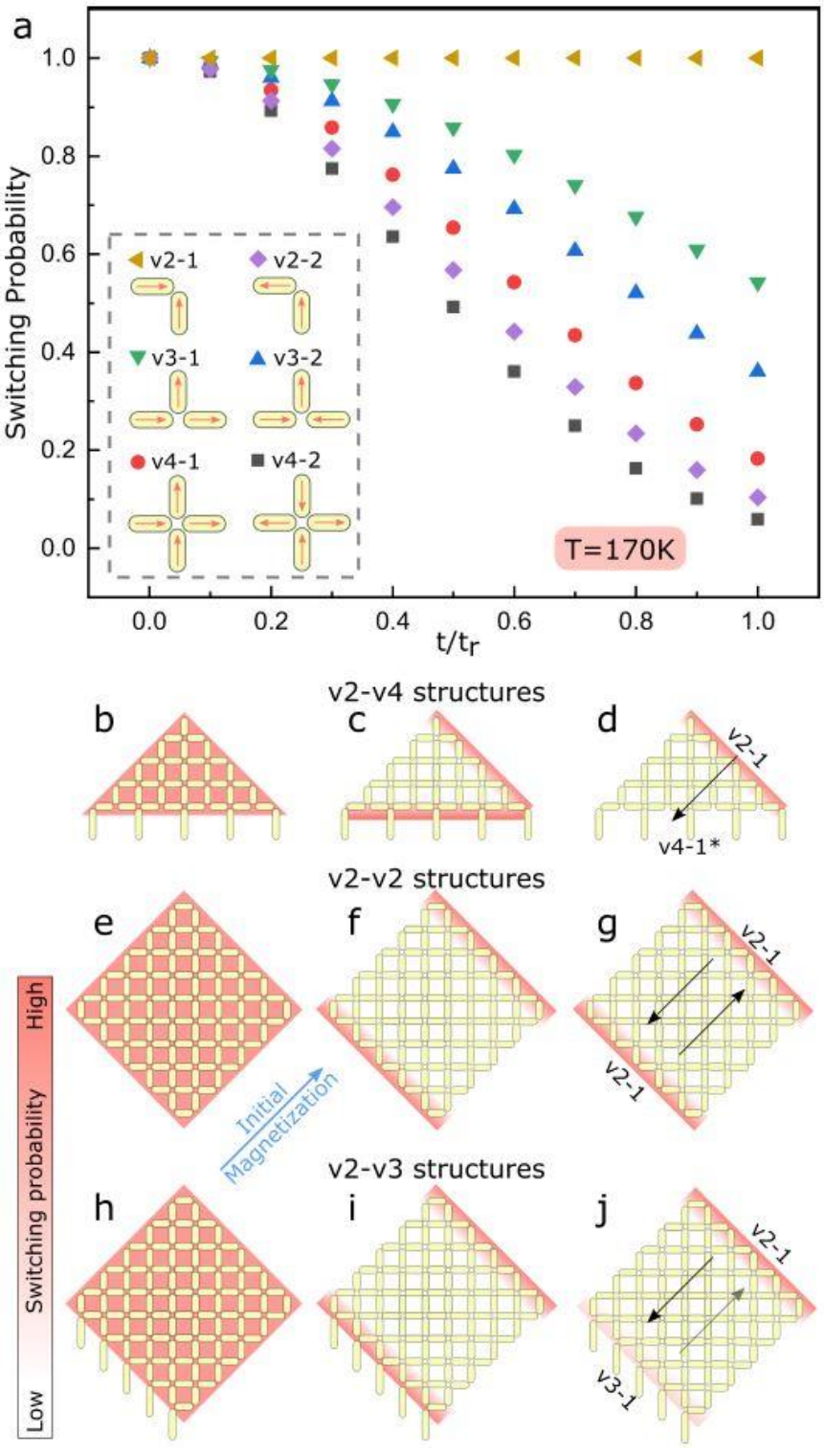

Figure 7.13: (a) Switching probabilities for different vertex configurations as a function of nanomagnet thickness. (b-j) switching probabilities expected to be observed in artificial square ice

structures with different vertex edges. Regions in red have a high probability for the injection of monopoles. Solid lines are used to distinguish nanomagnets of different thicknesses.

Thus, it is demonstrated that there is a correlation with the location of injection of monopoles as a function of nanomagnet thickness. It is also shown that an artificial spin ice could be tuned to observe a specific type of injection dynamics by carefully modifying either the sample thickness or the operating temperature.

7.6 Injection in Small Structures

In this part of the project, the aim was to deterministically control the injection of monopole currents in artificial spin ice. The broader goal has been to lay down the foundations to apply monopole currents for use in monopole based circuits. In this section, I will highlight some of the preliminary ideas concerning the implementation of monopole currents in smaller structures for use in monopole based devices.

A good starting point for me is to replicate the results I have obtained for extended arrays of artificial spin ice in a 1D structure. Examples such structures are shown in the X-PEEM images of 7.14a and 7.14d. Shown in Figure 7.14a are three artificial square ice structures, each with two termination edges where each of the structures is terminated differently. Similarly, in Figure 7.14d, three other artificial square ice structures are shown with each of them terminated differently. The X-PEEM images in Figures 7.14a to c correspond to different time steps during the course of a thermal protocol with the initial state shown in Figure 7.14a. Similarly, Figures 7.14e and f correspond to time steps following the initial state shown in Figure 7.14d. It can be seen that the injection probabilities in finite sized structures are same as those observed in extended arrays.

Such finite sized structures could therefore be used as building blocks in a monopole based computational device. For example, in Figure 7.14d, a structure is shown with a v3-1 (middle) and v4-1 termination (right) that involves a terminating edge with a single vertex, which I will now refer to as a *data line*. Such a design could be used to transport data from the v2-1 termination to either a v3-1 or a v4-1 termination quite reliably. Another way of visualizing the data line is to consider a typical transistor with, for example, a PNP junction in which an applied voltage is used to transport electrons from one junction to another to facilitate switching from a logic state of 0 to 1.

This idea can be taken a step further and a proposal can be made that the probability of transporting data from one end of a structure, such as the structure on the right in Figure 7.14d with a v4-1 termination, could be modified by incorporating a v3-1 termination in the middle of the data line. An example of such a modification to the data line, which is called the *Barracuda* due to its close resemblance to the fish species, is shown in Figure 7.15, for different vertex terminations this would result in different probabilities of obtaining a particular output. The v3-1/v3-2 configuration in Figure

7.15a would act like an on/off valve that would allow/restrict the flow of information depending on the type and location of the vertex configuration. For example, the schematic in Figure 7.15a shows a barracuda design in which the flow of a monopole current starts at the v2-1 edge (indicated with red circle) and terminates at the v4-1 edge (indicated with yellow circle). It should be pointed out that the propagation of the monopole in Figure 7.15 can take paths starting at either of the v3-1 valves (in purple), since both the v3-1 vertices are of the same energy. In contrast, in the schematic in Figure 7.15b, a barracuda design is shown in which the path of propagation for the monopole current is restricted. One of the valves now contains a v3-2 configuration and this configuration is more stable than that of a v3-1 valve. This gives a difference in the probability of switching for different valves and would mean that the monopole current is now more likely to pass through the v3-1 valve. If both the valves were to have a v3-2 configuration, as shown in schematic in Figure 7.15c, the flow of monopole current is only possible upon the application of a relaxation protocol with sufficient temperature to overcome the energy required to switch the v3-2 configuration to a v3-1 configuration.

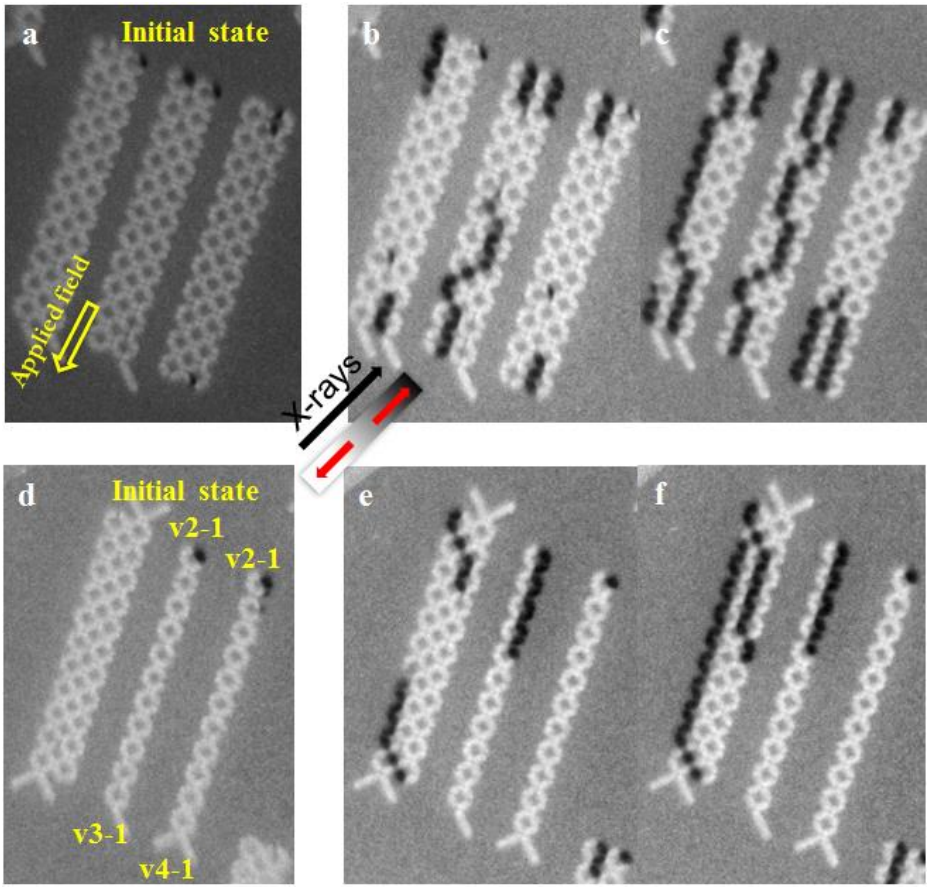

Figure 7.14: (a and d) X-PEEM images of an initial field-set state in small artificial square ice structures with different vertex terminations. (b-c) Observed dynamics following the initial field-set state (a) in which the injection is confined to particular terminations and is found to be similar to

that observed in extended arrays. (e-f) Observed dynamics following the initial field-set state in the structures shown (d) in which injection is restricted to the v2-1 terminations. The 1D structures (middle and right) in (d) could be used as building blocks to construct monopole based computation circuits.

It should also be noted that a valve does not necessarily have to be a single nanomagnet; it could also be a set of magnets corresponding to a logic gate where an entire logical operation is required to be completed before the data is transmitted along the data line. Other variations could include conditional data lines in which the switching of a nanomagnet in the data line leads to a cascade of other logical operations. Such a variety of building blocks could be implemented in both deterministic and probabilistic computation schemes in order to produce monopole based circuits.

Finally, I am currently considering how to concretely implement the above ideas in monopole based circuits and for this, future experiments are being planned. Some of this work may be performed by a new doctoral student that will be employed on the same Swiss National Science Foundation grant to pursue monopole circuits.

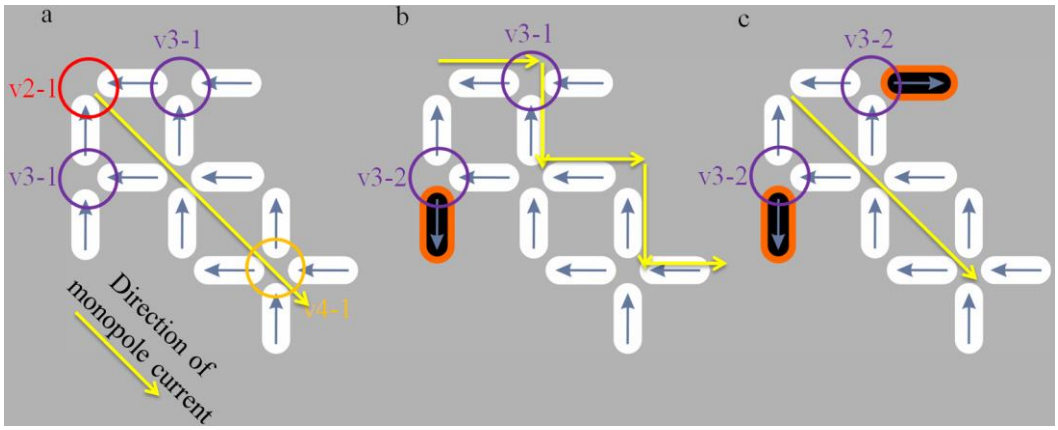

Figure 7.15: Different barracuda designs are shown in which the probability of injecting a monopole and therefore of generating a monopole current can be tuned by the strategic placement of nanomagnets with set moment orientations. (a) A barracuda design in which the propagation of monopole current begins by injection at the v2-1 edge and terminates at the v4-1 edge. (b) The monopole current is biased to take the path shown in yellow, due to the presence of a v3-2 configuration acting as a valve. (c) Two v3-2 configurations are now introduced and generating a monopole current would require high enough thermal energy to overcome the energy barrier for switching.

Acknowledgements: I performed the sample fabrication and SEM. I also performed the X-PEEM measurements with assistance from Jizhai Cui of Laboratory of Mesoscopic Systems and Jaianth Vijayakumar of the Swiss Light Source. Monte-Carlo simulations of the dynamics in the v2-

v4 structure, and probability calculations used to create the switching probabilities plot were performed by E.Y. Vedmedenko of University of Hamburg.

CHAPTER 8: CONCLUSION and OUTLOOK

In this thesis, I began by posing three critical questions that are relevant to creating computation using nanomagnets with ideas inspired from artificial spin ice. I will now conclude the thesis on the same note by summarizing my scientific contributions as responses/solutions to the three critical questions. I will also make an effort to highlight open questions or ideas I would like to have pursued if more time were presented.

Addressing Question 1:

…***is there a viable design alternative to perform nanomagnet based Boolean computation using ideas from artificial spin ice? And following from this, is it possible to demonstrate Boolean logic gates, such as NAND, using this design alternative?***

Linear vs. square chains

The first problem that I set out to solve was that of persistent errors in linear chains of nanomagnets. Upon plotting the energies associated with different states in a linear chain of nanomagnets, one finds that there are moment configurations that could become highly stable magnetic states, since they would require a single spin flip transition to a higher energy state before a relaxation to the ground state. This is a major problem, since information is transmitted across a linear chain in the form of a low energy configuration obtained on relaxation of magnetic moments. The presence of such metastable states would mean that errors in a linear chain are possible and therefore transmission of inaccurate information in the form of incorrect magnetic moment orientations is possible as well. Once this issue was realized, an alternative arrangement of nanomagnets needed to be found to stably support the transmission of data across a certain distance. Such a design was the square chain, in which an input nanomagnet set the initial state and the output was taken from the nanomagnet at the end of a chain. Energetically, a square design proved to be highly robust since all magnetic states, that are higher in energy than the ground state, require single spin flip transitions to a state with lower energy during the course of a relaxation.

I experimentally showed that data can be transmitted at far greater lengths in a square chain than in linear chains, up to an order of magnitude larger in length (~10 μm) but potentially longer. More critically, the transmitted information had a high operational reliability. Therefore, a square chain is a superior alternative to that of a linear chain in transmitting data across a certain distance using nanomagnets. It should be noted that I have also determined that linear chains could support long distance transfer of data, albeit still shorter than square chains, if an appropriate thermal protocol were to be applied. Experimentally, I showed that information can be transmitted across a linear chain

containing up to 50 nanomagnets in contrast to the 10 nanomagnet limit often reported in field-based relaxation experiments.

Identifying the problem*:* The presence of metastable states makes linear chains less reliable for the transfer of data across a distance.

My Solution*:* Square chains do not contain metastable states and therefore are largely error free when transporting data.

Key experimental results*:* (1) Square chains can support transfer of data across a distance that is an order magnitude longer than linear chains (~1 μm Vs. ~10 μm) (2) The use of a thermal protocol may significantly improve data transfer length in linear chains.

Further avenues of exploration: The drastic increase in the total number of nanomagnets in a linear chain that were found to be in ground state when implementing a thermal protocol needs to be rigorously explored. In particular, an upper limit to an error-free chain length, both for linear and square chains, would be an interesting question.

Logic gates: traditional nanomagnetic logic vs. artificial spin ice inspired logic

Similar to the presence of low energy, error prone metastable states in a linear chain, traditional logic gates are also populated with such metastable states. I took a traditional nanomagnetic logic gate design and plotted all the magnetic states as a function of energies to search for error prone metastable states. I found that many logic operations in a traditional nanomagnetic logic gate are energetically unstable with several metastable states that were close in energy. Such a presence of metastable states would explain why these logic gates are error prone and reported to experimentally show a 50% operational reliability. Therefore, similar to the square chain alternative to the transport of information across a distance, a new design needed to be created to perform Boolean operations.

Having already shown that square chains are highly reliable, it was reasonable to construct logic gates using square structures as building blocks. The design proved to be effective and yielded an operational reliability of >90%. More critically, I was able to demonstrate a functionally complete NAND logic gate.

Identifying the problem*:* Magnetic states associated with logic operations in traditional nanomagnetic logic gates are often associated with incorrect metastable states, which are likely to be responsible for the low operational reliability of 50%.

***My Contribution**:* Logic gates, including the functionally complete NAND gates, can be constructed out of square structures in which logic operations are highly reliable due to carefully designed relaxation pathways.

***Key experimental result**:* Logic gates constructed using square structures display an operational reliability of >90%.

Further avenues of exploration: (1) the operational speed of the logic gates has not been addressed. An experiment demonstrating ultrafast response in a pseudo-NAND gate and a comparison with traditional CMOS would be useful for determining additional computational viability of the newly designed logic gates. (2) It would be interesting to implement other artificial spin ice structures, such as the artificial kagome spin ice, fir computational logic and determine if other loop structures, such as hexagons and pentagons, would be viable candidates for nanomagnet based computation. It should be noted here that I tested chains of hexagonal rings to support data transfer but their thermal relaxation proved to be challenging, which is likely to be due to an increased degeneracy of the low energy states. I have therefore not included these inconclusive results in this thesis. (3) Complex circuits such as a half-adder could be designed and tested to see if they would compare to CMOS in computational viability and reliability.

Overarching finding: Boolean computation using building blocks from artificial square ice is a superior alternative to traditional nanomagnetic logic.

Addressing Question 2:

…***can we create computational building blocks using ideas from artificial spin ice to generate a weighted/probabilistic output, which could then be used in applications such as artificial neural networks?***

While it was found that the Boolean operation of artificial spin ice inspired logic gates was highly reliable, another key finding made during the course of designing the gates was that it was possible control their associated relaxation paths. These relaxation paths are characterized as the change in moment configurations required in an array of nanomagnets when relaxing from an initial state to that of a final state. They can be engineered to not incorporate higher energy metastable states so increasing the probability of reaching a particular low energy relaxed state. The natural question that followed was whether there is a possibility to deliberately engineer metastable states in a relaxation pathway such that the probability of reaching a final low energy relaxed state is now controlled by the energy associated with a metastable state.

Two approaches were taken to achieve probabilistic outcomes in logic gates: (1) To design a logic gate to incorporate a metastable stable in the form of an excess magnetic charge at a 4-vertex, so that the probability of obtaining a particular output state was dependent on the energy associated with the magnetic charge creation in the 4-vertex structure. (2) To modify the output in a Boolean logic gate by deliberately weakening the dipolar coupling in the output nanomagnet. Such a weakening of the dipolar coupling was achieved by physically moving the loop structure comprising the output nanomagnet away from rest of the logic gate.

I found both approaches successfully resulted in a probabilistic output. The disadvantage with (1) however, was the fixed nature of the energy barrier. The design approach in (2) meant that I was able to show an active modulation of the output to give multiple probabilities.

Finally, I demonstrated a way to connect different logic gates together to perform Boolean operations. Such a scheme to connect logic gates, where the connecting nanomagnets do not lead to excess magnetic charge creation, is required to ensure operational reliability in complex structures.

Identifying the problem: Relaxation pathways are instrumental for predicting deterministic or probabilistic outputs in arrangements of nanomagnets.

My Contribution: Systematically investigated different relaxation pathways and developed a series of rules/conditions governing the appearance of different types of relaxation pathways in arrangements of nanomagnets.

Key experimental results*:* (1) Logic gates were constructed to deliberately incorporate an energy barrier in the relaxation pathway leading to a probabilistic output. (2) Active modulation of the output probability was achieved by weakening the dipolar coupling between the output structure and rest of the logic gate. (3) Data can be transported between multiple logic gates.

Other avenues of exploration: (1) Designing a magnetic Hamiltonian to solve computationally difficult problems such as image detection using the relaxation pathways approach. (2) Designing of experiments to pursue NP-type problems such as the traveling salesman problem. (3) A spintronic approach to modulating the probability of an output by incorporating a current carrying nanowire in the D- or P-gates. (4) The role of critical *n*, i.e. the highest number of nanomagnets in an n-loop structure or an n-vertex structure, at which the rules described in Chapter 4 would break down. (5) Implementing a simple artificial neural network such as a perceptron to test for learning.

Overarching finding: Probabilistic computation using building blocks from artificial square ice can be achieved by either incorporating excess magnetic charge states in the relaxation pathway or by modifying the strength of dipolar coupling in an output nanomagnet.

Addressing Question 3:

…is it possible to control the generation and evolution of monopole currents in artificial spin ice? If yes, can we implement them as part of a device?

In the creation of structures for probabilistic computing, I have implemented excess magnetic charge at a 4-vertex in an artificial square ice to modify the probability of obtaining a specific state. These excess charges are often termed emergent magnetic monopoles or monopoles. In an extended array of an artificial spin ice, such as the artificial square ice, these monopoles often occur in pairs and are connected by a chain of reversed nanomagnets with a head-to-tail moment orientation. The reversed nanomagnets connecting two oppositely charged monopoles are referred to as Dirac strings and, in this PhD, the dynamics of charged monopoles is considered to be monopole currents, which could be implemented for computation in a similar manner to domain walls in magnetic nanowires[81].

There have been attempts to deliberately nucleate monopoles at a location of choice, which would lead to the production of monopole currents. However, such experiments have not been successful due to the use of incorrect design or have been attributed to the presence of disorder in the artificial spin ice. Having worked with the design of relaxation pathways to produce computational logic, it naturally made sense to control the injection of monopoles and the subsequent generation of monopole currents by engineering the edge terminations. Thus, I modified an existing artificial square ice design, by terminating the edges with different vertex configurations. Such an asymmetry in the artificial square ice design results in regions where injection is highly probable and others where injection is unlikely. I found that, by ensuring that one of edges has terminating vertex configurations with a high energy compared to those at the other terminating edge, preferential injection of monopoles at specific locations and directional generation of monopole currents could be achieved. It was also demonstrated, by plotting the switching probabilities, in which the location of injecting monopoles depends on the nanomagnet thickness, and therefore the moment strength and the temperature. Therefore, tuning of parameters such as the temperature could be used to control the location of injection of monopoles for different applications.

In addition, I proposed the idea of a valve in the form of a tunable vertex configuration, to control the flow of an already generated monopole current with a particular probability. Such a structure would act as a data transfer line where the probability of the output is dependent on the type and the location of the valve used. Depending on how the valve is set up, it is possible to control the direction of data flow that is used to trigger operations in additional logic devices or to only let a monopole current flow after a specific computing operation is performed.

Identifying the problem: A method to control the location of monopole injection is required. Instead of adding nanomagnets with different coercivities to the edges of an artificial spin ice, we can exploit different vertex configurations with different switching probabilities.

My Contribution: Terminating an artificial square ice with different vertex configurations leads to location specific injection of monopoles and the generation of directional monopole currents. This would help in creating monopole current based computational circuits.

Key experimental results*:* (1) Demonstrated local control of injection and propagation of monopole currents in modified artificial square ice. (2) The probability of injecting a monopole is dependent on the type of vertex termination and therefore can be used to tailor the probability of injection for use in applications such as probabilistic computation. (3) Obtained a switching probabilities plot in which the thickness of the nanomagnets, and therefore the magnetic moment and temperature, determines the location of injection of monopoles in different artificial square ice structures.

Other avenues of exploration: (1) Create a NAND logic gate using monopole based currents. (2) Probabilistic computation using monopole currents. (3) The design of a magnetic Hamiltonian to solve computationally difficult problems such as image detection and the design of experiments to solve NP-type problems such as the traveling salesman problem. (4) The directional flow of monopole currents may be implemented into a monopole transistor type device.

Overarching finding: Asymmetric vertex terminations can be leveraged to inject monopoles at specific locations and, subsequently, to control the direction of the injected monopole currents.

REFERENCES

1. Brinkman WF, Haggan DE, Troutman WW. A history of the invention of the transistor and where it will lead us. *IEEE Journal of Solid-State Circuits* **32**, 1858-1865 (1997).

2. Lloyd S. Ultimate physical limits to computation. *Nature* **406**, 1047 (2000).

3. Wirth N. A Brief History of Software Engineering. *IEEE Annals of the History of Computing* **30**, 32-39 (2008).

4. Cowburn RP, Welland ME. Room Temperature Magnetic Quantum Cellular Automata. *Science* **287**, 1466 (2000).

5. Imre A, Csaba G, Ji L, Orlov A, Bernstein GH, Porod W. Majority Logic Gate for Magnetic Quantum-Dot Cellular Automata. *Science* **311**, 205 (2006).

6. Niemier MT, *et al.* Nanomagnet logic: progress toward system-level integration. *Journal of Physics: Condensed Matter* **23**, 493202 (2011).

7. Shah FA, Csaba G, Niemier MT, Hu XS, Porod W, Bernstein GH. Error analysis for ultra dense nanomagnet logic circuits. *Journal of Applied Physics* **117**, 17A906 (2015).

8. Wang RF, *et al.* Artificial 'spin ice' in a geometrically frustrated lattice of nanoscale ferromagnetic islands. *Nature* **439**, 303 (2006).

9. Markram H. The human brain project. *Scientific American* **306**, 50-55 (2012).

10. Pauling L. The Structure and Entropy of Ice and of Other Crystals with Some Randomness of Atomic Arrangement. *Journal of the American Chemical Society* **57**, 2680-2684 (1935).

11. Bramwell ST, Gingras MJP. Spin Ice State in Frustrated Magnetic Pyrochlore Materials. *Science* **294**, 1495 (2001).

12. Heyderman LJ, Stamps RL. Artificial ferroic systems: novel functionality from structure, interactions and dynamics. *Journal of Physics: Condensed Matter* **25**, 363201 (2013).

13. Castelnovo C, Moessner R, Sondhi SL. Magnetic monopoles in spin ice. *Nature* **451**, 42 (2008).

14. Mól LA, Silva RL, Silva RC, Pereira AR, Moura-Melo WA, Costa BV. Magnetic monopole and string excitations in two-dimensional spin ice. *Journal of Applied Physics* **106**, 063913 (2009).

15. Mengotti E, Heyderman LJ, Rodríguez AF, Nolting F, Hügli RV, Braun H-B. Real-space observation of emergent magnetic monopoles and associated Dirac strings in artificial kagome spin ice. *Nature Physics* **7**, 68 (2010).

16. Ladak S, Read DE, Perkins GK, Cohen LF, Branford WR. Direct observation of magnetic monopole defects in an artificial spin-ice system. *Nature Physics* **6**, 359 (2010).

17. Nisoli C, Moessner R, Schiffer P. Colloquium: Artificial spin ice: Designing and imaging magnetic frustration. *Reviews of Modern Physics* **85**, 1473-1490 (2013).

18. Li Y, *et al.* Brillouin light scattering study of magnetic-element normal modes in a square artificial spin ice geometry. *Journal of Physics D: Applied Physics* **50**, 015003 (2017).

19. Panagiotopoulos I. Confined spin wave spectra of Kagome artificial spin ice arrays. *Journal of Magnetism and Magnetic Materials* **422**, 227-231 (2017).

20. Zhou X, Chua GL, Singh N, Adeyeye Adekunle O. Large Area Artificial Spin Ice and Anti-Spin Ice Ni80Fe20 Structures: Static and Dynamic Behavior. *Advanced Functional Materials* **26**, 1437-1444 (2016).

21. Gypens P, Leliaert J, Van Waeyenberge B. Balanced Magnetic Logic Gates in a Kagome Spin Ice. *Physical Review Applied* **9**, 034004 (2018).

22. Hanu A, *et al.* Computational logic with square rings of nanomagnets. *Nanotechnology* **29**, 265205 (2018).

23. Kim NS, *et al.* Leakage current: Moore's law meets static power. *Computer* **36**, 68-75 (2003).

24. Roy K, Mukhopadhyay S, Mahmoodi-Meimand H. Leakage current mechanisms and leakage reduction techniques in deep-submicrometer CMOS circuits. *Proceedings of the IEEE* **91**, 305-327 (2003).

25. Salahuddin S, Datta S. Use of Negative Capacitance to Provide Voltage Amplification for Low Power Nanoscale Devices. *Nano Letters* **8**, 405-410 (2008).

26. Hong J, Lambson B, Dhuey S, Bokor J. Experimental test of Landauer's principle in single-bit operations on nanomagnetic memory bits. *Science Advances* **2**, (2016).

27. Imre A, Csaba G, Bernstein GH, Porod W, Metlushko V. Investigation of shape-dependent switching of coupled nanomagnets. *Superlattices and Microstructures* **34**, 513-518 (2003).

28. Carlton D, *et al.* Investigation of Defects and Errors in Nanomagnetic Logic Circuits. *IEEE Transactions on Nanotechnology* **11**, 760-762 (2012).

29. Lambson B, Gu Z, Monroe M, Dhuey S, Scholl A, Bokor J. Concave nanomagnets: investigation of anisotropy properties and applications to nanomagnetic logic. *Applied Physics A* **111**, 413-421 (2013).

30. Gu Z, *et al.* Sub-nanosecond signal propagation in anisotropy-engineered nanomagnetic logic chains. *Nature Communications* **6**, 6466 (2015).

31. Gubbi J, Buyya R, Marusic S, Palaniswami M. Internet of Things (IoT): A vision, architectural elements, and future directions. *Future Generation Computer Systems* **29**, 1645-1660 (2013).

32. Lucas A. Ising formulations of many NP problems. *Frontiers in Physics* **2**, (2014).

33. Cook SA. The complexity of theorem-proving procedures. In: *Proceedings of the third annual ACM symposium on Theory of computing* (ed^(eds). ACM (1971).

34. Fortnow L. The status of the P versus NP problem. *Commun ACM* **52**, 78-86 (2009).

35. Hoffman KL, Padberg M, Rinaldi G. Traveling Salesman Problem. In: *Encyclopedia of Operations Research and Management Science* (ed^(eds Gass SI, Fu MC). Springer US (2013).

36. Reinelt G. TSPLIB—A Traveling Salesman Problem Library. *ORSA Journal on Computing* **3**, 376-384 (1991).

37. Bhanja S, Karunaratne DK, Panchumarthy R, Rajaram S, Sarkar S. Non-Boolean computing with nanomagnets for computer vision applications. *Nature Nanotechnology* **11**, 177 (2015).

38. McMahon PL, *et al.* A fully-programmable 100-spin coherent Ising machine with all-to-all connections. *Science*, (2016).

39. Sutton B, Camsari KY, Behin-Aein B, Datta S. Intrinsic optimization using stochastic nanomagnets. *Scientific Reports* **7**, 44370 (2017).

40. Sharmin S, Shim Y, Roy K. Magnetoelectric oxide based stochastic spin device towards solving combinatorial optimization problems. *Scientific Reports* **7**, 11276 (2017).

41. Grollier J, Querlioz D, Stiles MD. Spintronic Nanodevices for Bioinspired Computing. *Proceedings of the IEEE* **104**, 2024-2039 (2016).

42. Torrejon J, *et al.* Neuromorphic computing with nanoscale spintronic oscillators. *Nature* **547**, 428 (2017).

43. Sharad M, Augustine C, Panagopoulos G, Roy K. Spin-Based Neuron Model With Domain-Wall Magnets as Synapse. *IEEE Transactions on Nanotechnology* **11**, 843-853 (2012).

44. Yamamoto Y, *et al.* Coherent Ising machines—optical neural networks operating at the quantum limit. *npj Quantum Information* **3**, 49 (2017).

45. Torlai G, Melko RG. Learning thermodynamics with Boltzmann machines. *Physical Review B* **94**, 165134 (2016).

46. Vedmedenko EY. Dynamics of Bound Monopoles in Artificial Spin Ice: How to Store Energy in Dirac Strings. *Physical Review Letters* **116**, 077202 (2016).

47. Thonig D, Henk J. Pinning of thermal excitations at defects in artificial dipolar arrays: A theoretical investigation. *Journal of Magnetism and Magnetic Materials* **386**, 117-124 (2015).

48. Budrikis Z, *et al.* Disorder Strength and Field-Driven Ground State Domain Formation in Artificial Spin Ice: Experiment, Simulation, and Theory. *Physical Review Letters* **109**, 037203 (2012).

49. Hügli RV, *et al.* Artificial kagome spin ice: dimensional reduction, avalanche control and emergent magnetic monopoles. *Philosophical Transactions of the Royal Society A: Mathematical, Physical and Engineering Sciences* **370**, 5767 (2012).

50. Farhan A, *et al.* Direct Observation of Thermal Relaxation in Artificial Spin Ice. *Physical Review Letters* **111**, 057204 (2013).

51. Kodama RH. Magnetic nanoparticles. *Journal of Magnetism and Magnetic Materials* **200**, 359-372 (1999).

52. Kittel C. *Introduction to solid state physics*.

53. Tannous C, Gieraltowski J. The Stoner–Wohlfarth model of ferromagnetism. *European Journal of Physics* **29**, 475 (2008).

54. Brown WF. Thermal Fluctuations of a Single-Domain Particle. *Physical Review* **130**, 1677-1686 (1963).

55. Stöhr J. X-ray magnetic circular dichroism spectroscopy of transition metal thin films. *Journal of Electron Spectroscopy and Related Phenomena* **75**, 253-272 (1995).

56. Trieste E-S. Elettra-Sincrotrone Trieste (2011).

57. van der Laan G, Figueroa AI. X-ray magnetic circular dichroism—A versatile tool to study magnetism. *Coordination Chemistry Reviews* **277-278**, 95-129 (2014).

58. Le Guyader L, *et al.* Studying nanomagnets and magnetic heterostructures with X-ray PEEM at the Swiss Light Source. *Journal of Electron Spectroscopy and Related Phenomena* **185**, 371-380 (2012).

59. Hartmann U. MAGNETIC FORCE MICROSCOPY. *Annual Review of Materials Science* **29**, 53-87 (1999).

60. Binnig G, Quate CF, Gerber C. Atomic Force Microscope. *Physical Review Letters* **56**, 930-933 (1986).

61. Jalili N, Laxminarayana K. A review of atomic force microscopy imaging systems: application to molecular metrology and biological sciences. *Mechatronics* **14**, 907-945 (2004).

62. Farhan A, *et al.* Direct Observation of Thermal Relaxation in Artificial Spin Ice. *PRL* **111**, 057204 (2013).

63. Shah FA, Csaba G, Niemier MT, Hu XS, Porod W, Bernstein GH. Error Analysis for Ultra Dense Nanomagnetic Logic Circuits. *J Appl Phys* **117**, 17A906 (2015).

64. Harrison MA. *Introduction to switching and automata theory*. Mac Graw-Hill (1965).

65. Bhowmik D, You L, Salahuddin S. Spin Hall effect clocking of nanomagnetic logic without a magnetic field. *Nature Nanotechnology* **9**, 59 (2013).

66. Alam MT, *et al.* On-Chip Clocking of Nanomagnet Logic Lines and Gates. *IEEE Transactions on Nanotechnology* **11**, 273-286 (2012).

67. Arava H, *et al.* Engineering Relaxation Pathways in Building Blocks of Artificial Spin Ice for Computation. *arXiv preprint arXiv:181206936*, (2018).

68. Farhan A, *et al.* Exploring hyper-cubic energy landscapes in thermally active finite artificial spin-ice systems. *Nat Phys* **9**, 375-382.

69. Chopdekar RV, *et al.* Controlling vortex chirality in hexagonal building blocks of artificial spin ice. *New Journal of Physics* **15**, 125033 (2013).

70. Krause S, *et al.* Magnetization Reversal of Nanoscale Islands: How Size and Shape Affect the Arrhenius Prefactor. *Physical Review Letters* **103**, 127202 (2009).

71. Gliga S, *et al.* Emergent dynamic chirality in a thermally driven artificial spin ratchet. *Nature Materials* **16**, 1106.

72. Kiermaier J, Breitkreutz S, Csaba G, Schmitt-Landsiedel D, Becherer M. Electrical input structures for nanomagnetic logic devices. *Journal of Applied Physics* **111**, 07E341 (2012).

73. D'Souza N, Salehi Fashami M, Bandyopadhyay S, Atulasimha J. Experimental Clocking of Nanomagnets with Strain for Ultralow Power Boolean Logic. *Nano Letters* **16**, 1069-1075 (2016).

74. Östman E, *et al.* Interaction modifiers in artificial spin ices. *Nature Physics* **14**, 375-379 (2018).

75. Bramwell ST, Giblin SR, Calder S, Aldus R, Prabhakaran D, Fennell T. Measurement of the charge and current of magnetic monopoles in spin ice. *Nature* **461**, 956 (2009).

76. Jaubert LDC, Holdsworth PCW. Signature of magnetic monopole and Dirac string dynamics in spin ice. *Nature Physics* **5**, 258 (2009).

77. Morley SA, *et al.* Thermally and field-driven mobility of emergent magnetic charges in square artificial spin ice. Preprint at https://ui.adsabs.harvard.edu/\#abs/2018arXiv180907472M (2018).

78. Morley SA. The Dynamics of Artificial Spin Ice in Real and Reciprocal Space. (ed^(eds). University of Leeds (2015).

79. Vedmedenko EY, Mikuszeit N, Oepen HP, Wiesendanger R. Multipolar Ordering and Magnetization Reversal in Two-Dimensional Nanomagnet Arrays. *Physical Review Letters* **95**, 207202 (2005).

80. Vedmedenko EY, Mikuszeit N. Multipolar Ordering in Electro- and Magnetostatic Coupled Nanosystems. *ChemPhysChem* **9**, 1222-1240 (2008).

81. Allwood DA, Xiong G, Faulkner CC, Atkinson D, Petit D, Cowburn RP. Magnetic Domain-Wall Logic. *Science* **309**, 1688 (2005).